

TALLINN UNIVERSITY OF TECHNOLOGY
DOCTORAL THESIS
55/2019

Investigation of the Eddy Viscosity for a Breaking Wave in the Surf Zone

NELLY OLDEKOP



TALLINN UNIVERSITY OF TECHNOLOGY

School of Engineering

Department of Civil Engineering and Architecture

This dissertation was accepted for the defence of the degree of Doctor of Philosophy on 05/11/2019

Supervisor: Associate Professor Janek Laanearu
School of Engineering
Tallinn University of Technology
Tallinn, Estonia

Co-supervisor: PhD Toomas Liiv
Corson LLC
Tallinn, Estonia

Opponents: Professor Ping Dong
School of Engineering
Department of Civil Engineering and Industrial Design
University of Liverpool
Liverpool, United Kingdom

Professor Boriss Gjunsburgs
Civil Engineering Faculty
Department of Water Engineering and Technology
Riga Technical University
Riga, Latvia

Defence of the thesis: 10/12/2019, Tallinn

Declaration:

Hereby I declare that this doctoral thesis, my original investigation and achievement, submitted for the doctoral degree at Tallinn University of Technology, has not been previously submitted for doctoral or equivalent academic degree.

Nelly Oldekop

signature



European Union
European Regional
Development Fund



Investing
in your future

Copyright: Nelly Oldekop, 2019

ISSN 2585-6898 (publication)

ISBN 978-9949-83-498-3 (publication)

ISSN 2585-6901 (PDF)

ISBN 978-9949-83-499-0 (PDF)

TALLINNA TEHNIKAÜLIKOOL
DOKTORITÖÖ
55/2019

Turbulentse viskoossusteguri määramine murdlaine piirkonnas ranna-alal

NELLY OLDEKOP



Contents

List of Publications	7
Author's Contribution to the Publications	8
Introduction	9
Objectives of the research	9
Methodology and structure of the thesis	9
Publications overview	10
Abbreviations	11
Symbols	12
1 Experimental measurements and data analysis	14
1.1 Field measurements.....	15
1.2 Laboratory measurements.....	16
1.3 Wave data analysis.....	16
1.3.1 Existing physical model	16
1.3.2 Measurement data analysis.....	19
2 Turbulence models in coastal engineering	24
2.1 Classification of turbulence models	25
2.2 Theoretical model	27
2.2.1 The turbulent-viscosity hypothesis	27
2.2.2 Channel flow case	27
2.3 Empirical models	29
2.4 Development of the calculation method	30
2.4.1 Processing of experimental results	30
2.4.2 Modified wave characteristics	32
2.4.3 Shear velocity	36
2.4.4 Turbulent kinetic energy	37
2.4.5 Eddy viscosity	39
3 Modelling and simulation	45
3.1 Theoretical background	45
3.1.1 The equations of fluid motion.....	45
3.2 Large Eddy Simulations	47
3.3 Smoothed Particle Hydrodynamics	48
3.4 Development of numerical model and comparison with experimental findings.....	51
3.4.1 Processing of numerical results	51
3.4.2 Comparison of experimental and numerical findings	52
4 Conclusions	55
Findings of this thesis.....	55
Future work.....	56
List of Figures	57
List of Tables	60
References	61
Acknowledgements.....	69

Abstract.....	70
Lühikokkuvõte.....	71
Appendix.....	73
Publication I.....	73
Publication II.....	85
Publication III.....	93
Publication IV.....	109
Curriculum vitae.....	122
Elulookirjeldus.....	124

List of Publications

The list of author's publications, on the basis of which the thesis has been prepared:

- I Oldekop, N., & Liiv, T. (2013). Measurement of the variation of shear velocity on bed during a wave cycle. *Journal of Earth Science and Engineering*, 3(5), 322–330.
- II Oldekop, N., & Liiv, T. (2015). The variation of turbulent eddy viscosity during wave cycle. *E-Proceedings of the 36th IAHR World Congress*, The Hague, Netherlands, 28 June – 3 July 2015, 1–5.
- III Oldekop, N., Liiv, T. & Laanearu, J. (2019). Experimental study of eddy viscosity for breaking waves on sloping bottom and comparisons with empirical and numerical predictions. *Proceedings of the Estonian Academy of Sciences*, 68(3), 299–312.
- IV Oldekop, N., Laanearu, J. & Liiv, T. (2019). The streamline curvature dependent eddy viscosity for a plunging breaker. *Submitted to Journal of Hydraulic Research*

The list of author's conference presentations:

Oldekop, N.; Liiv, T. (2012). Measurement of the Variation Bed Shear Stress during a Wave Cycle. *Proceedings: 6th International Conference on Scour and Erosion*, Paris, France, 27 – 31 August 2012. Societe Hydrotechnique de France, 152–157.

Oldekop, N., & Liiv, T. (2015). The variation of turbulent eddy viscosity during wave cycle. *E-Proceedings of the 36th IAHR World Congress*, The Hague, Netherlands, 28 June – 3 July 2015, 1–5.

Author's Contribution to the Publications

Contribution to the papers in this thesis:

- I The author was part of the two-person team that created the original idea and the method design. All data processing and analysis were done by the author. The author had a major role in contributing to results interpretation and manuscript preparation.
- II The author was part of the two-person team that created the original idea. The full method design, the major part of the data processing and analysis was done by the author. The author had a major role in contributing to results interpretation and manuscript preparation.
- III The author was part of the four-person team that created the original idea. An equal part of the method design, a major part of the data processing and analysis was done by the author. The author had a major role in contributing to results interpretation and manuscript preparation. The SPH model used in the article was developed by the master-level student Gleb Bogomol during the special course of fluid dynamics at Tallinn University of Technology.
- IV The author was part of the three-person team that created the original idea. An equal part of the method design, a major part of the data processing and analysis was done by the author. The author had a major role in contributing to results interpretation and manuscript preparation.

Introduction

Turbulence generated by breaking waves is important for most processes within the surf zone. Processes like wave transformation, generation of nearshore currents, sediment transport, and diffusion of materials are directly connected to turbulence. Resulting from the distribution of wave field and viscous flow velocity and concentration of moving particles over the flow field, determination of turbulence is one of the basic tasks of engineers working in the field of fluid mechanics. However, because the turbulent transport processes cannot be calculated with an exact method, they must be approximated by a turbulent model, with the aid of empirical information. This approach still fails to solve many real-life flow problems.

During the last decades, research of the processes where turbulence dominates the flow has shifted from simple phenomenological descriptions to sophisticated numerical models in which the flow is described in detail. Even though, engineers still resort to physical modelling; advances in computer technology have made it possible to test thoroughly increasingly complex turbulence theories and to apply them in practical calculations. As a result, the theoretical treatment of field problems is gaining ground.

Most of the turbulent model development and application work is based on the hypothesis that turbulent processes require empirical input, which simulates the effect of turbulence on the mean-flow behaviour but does not access the details of the turbulent motion. Today it is recognized that a simple model that does not include such essential parameters as eddy viscosity or turbulent shear stresses is not acceptable for the complex problem of wave motion in the surf zone.

Objectives of the research

The purpose of the present thesis is to work out the turbulent model applicable to the flow in the surf zone on the sloping bottom that would give adequate results for eddy viscosity under breaking waves.

To meet the goal, firstly, an intensive work along with in-depth analysis of the raw data measured on the surf zone model was carried out. According to previous authors, considerable difficulties are encountered in determining turbulent eddy viscosity; thus, based on previous analysis, a calculation method for eddy viscosity was developed. Thirdly, a sophisticated numerical model for eddy viscosity was proposed.

Methodology and structure of the thesis

In this thesis, three methodologies are used – analysis of the physical model, development of a theoretical method and comparison of the results with empirical models and numerical modelling.

Chapter 1 outlines the fundamentals of experimental measurements in the field and laboratory environment with the necessary literature overview. In this research, Laser Doppler Anemometer measurement in an open wave flume was used. The chapter concludes with the interpretation of wave characteristics from the raw data.

Chapter 2 introduces the basic theory behind coastal hydrodynamics and provides a literature overview of the fields of application. Then, the turbulence models are classified with a detailed literature overview. Next, a theoretical method for weakly compressible fluid is proposed and processed with modifications. Also, in this chapter, empirical models are outlined with a literature review covering their compatibility with

the free shear flow and near-wall shear flow. The final section of this chapter addresses the modified wave characteristics, and shear stress, turbulent kinetic energy and eddy viscosity are calculated and discussed.

Chapter 3 presents a theoretical background for modelling and simulations by outlining the equations of fluid motion. Also, in this chapter, the literature review gives thorough insight for empirical and numerical modelling. Smoothed Particle Hydrodynamics modified model was tested for eddy viscosity in the open channel environment. The chapter concludes with a comparison of experimental and numerical findings.

Chapter 4 summarizes the results and discusses the findings.

Publications overview

For this thesis, in **Publication I** (and **Conference presentation**), the values of shear velocity on the boundary layers under breaking waves were investigated. The results confirmed that shear velocity values vary both in time and space, and the maximum value is always under the wave crest and the value decreases rapidly after the crest has passed. It was found that the shear velocity profiles gathered from an open channel flow are different from the shear velocity profiles measured in the experiments with a U-pipe.

Turbulence progresses because of the instability of a vortical flow, so turbulence injection description can only be simplified once the mechanisms for vorticity production in a wave are known. This can be done through handling turbulent stresses utilizing the Boussinesq eddy viscosity assumption. However, following the commonly used incompressible fluid concept from U-pipes, the results in **Publication II** (and **Conference presentation**) were obtained with eddy viscosity that contains singularities. It was also confirmed that eddy viscosity varies both in time and space as the wave propagates and is at least two orders of magnitude larger than the corresponding dynamic viscosity.

Later studies revealed that the spurious peaks and negative values in eddy viscosity are related to the velocity corresponding to a potential part of the flow where its gradient components do not represent the shear straining and manifest themselves when the shear stress and the velocity gradient change signs, i.e., flow reversal. However, removing the premise of an irrotational flow and regarding the production of vorticity due to the roller as the fundamental ingredient for a physical description of the energy dissipation will lead to the use of a nonlinear Boussinesq-type model. As such, the breaking terms are derived directly through the decomposition of the velocity into a potential and a rotational part. For that purpose, in **Publication III** (and **Seminar presentations**), turbulent stresses are described by the Boussinesq eddy viscosity assumption for a weakly compressible fluid. The irrotational flow that masked the turbulence velocity field under a breaking wave was removed through oscillating velocity at the bottom and four coefficients were used to modify the particular mean velocity gradient components. The resulting eddy viscosity is positively valued during the wave period, which gives evidence of the modified velocity field corresponding well to the shear and compression strain that results from the bottom and surface boundary layers.

In addition to the theoretical formulae, empirical formulae were used to estimate the eddy viscosity values during the wave period. Furthermore, a meshless numerical model is proposed to determine artificial viscosity and demonstrate its dependence on eddy viscosity in the case of a weakly compressible fluid. **Publication IV** confirms further the results from **Publication III** that the eddy viscosity does not vary just during the wave period, but it also varies over the water depth.

Abbreviations

ADCP	Acoustic Doppler Current Profilers
ADP	Acoustic Doppler Profilers
ADV	Acoustic Doppler Velocimeters
CFD	Computational Fluid Dynamics
CFL	Courant-Freidrichs-Lewy (constraint)
DES	Detached Eddy Simulation
DNS	Direct Numerical Simulation
EMCM	Electromagnetic Current Meters
EVM	linear Eddy Viscosity Model
LES	Large Eddy Simulations
LDA	Laser Doppler Anemometer
NLEVM	Non-linear Eddy Viscosity Model
RANS	Reynolds-Averaged Navier-Stokes model
RNG	Re-Normalization Group model
RP	Reference point
SPH	Smoothed Particle Hydrodynamics
SST	Shear Stress Transport model

Symbols

Upper-case Roman	
A, B, C, D	function
C	wave celerity (m s^{-2})
C_0	deep water wave celerity (m s^{-2})
C_μ, C_S	empirical constant (-)
D/Dt	substantial derivative
$\bar{D}/\bar{D}t$	mean substantial derivative
H_0	deep water wave height (m)
H_b	wave height at the breaking point (m)
L	turbulence length scale (m)
L_0	deep water wave length (m)
L_ϵ	Kolmogorov length scale (m)
\mathcal{P}	Turbulent production ($\text{m}^2 \text{s}^{-3}$)
T	wave period (s)
U	instantaneous local velocity (m s^{-1})
$\langle U \rangle$	ensemble-averaged velocity (m s^{-1})
$\langle U_1 \rangle$	ensemble-averaged horizontal velocity (m s^{-1})
$\langle U_2 \rangle$	ensemble-averaged vertical velocity (m s^{-1})
$\langle U \rangle_b$	ensemble-averaged velocity on bottom boundary (m s^{-1})
$\langle U \rangle_p$	ensemble-averaged potential velocity (m s^{-1})
$\langle U \rangle_t$	modified ensemble-averaged velocity (m s^{-1})
U_*	shear velocity (m s^{-1})
W_{ij}	interpolating kernel
Lower-case Roman	
a_{ij}	Reynolds stress anisotropic component ($\text{m}^2 \text{s}^{-2}$)
c	sound speed (m s^{-1})
d	still water depth (m)
d_b	still water depth at the breaking point (m)
g	gravity (m s^{-2})
h	water depth including water set-up (m)
h	smoothing length in SPH (m)
h_b	water depth at the breaking point including water set-up (m)
k_T	turbulent kinetic energy ($\text{m}^2 \text{s}^{-2}$)
m	particle mass (kg)
p	pressure ($\text{kg m}^{-1} \text{s}^{-2}$)
Δr	interparticle spacing (m)
$\langle u \rangle$	velocity fluctuation (m s^{-1})
$\langle u_1 \rangle$	horizontal velocity fluctuation (m s^{-1})
$\langle u_2 \rangle$	vertical velocity fluctuation (m s^{-1})

x_1	along the flow horizontal coordinate
x_2	vertical coordinate
x_b	horizontal distance from the reference point (m)
Upper-case Greek	
Π_{ij}	viscosity term
Lower-case Greek	
α	artificial viscosity coefficient
δ_{ij}	Kronecker delta (-)
ε	turbulence energy dissipation rate ($\text{m}^2 \text{s}^{-3}$)
μ	dynamic viscosity (N s m^{-2})
ν	kinematic viscosity ($\text{m}^2 \text{s}$)
$\nu_{A,ij}$	artificial viscosity
ν_T	eddy viscosity ($\text{m}^2 \text{s}^{-1}$)
ρ	fluid density (kg m^3)
τ_b	bottom shear stress (N m^{-2})
τ_{ij}	stress tensor
ω	turbulence energy dissipation rate ($\text{m}^2 \text{s}^{-3}$)
Symbols	
$\partial/\partial x$	partial differential
∇	vector differential operator

1 Experimental measurements and data analysis

The development of shoaling leads to a change in wave height, when waves propagate into shallower water. At a certain location, where the wave height is about 0.8 times the local water depth, the wave breaks. The wave crest topples over because instability from the forward wave orbital velocity becomes too large. While the shoaling process is considered as a process with a very small loss of wave energy, the wave-breaking is characterised as a process with a large portion of wave energy dissipation.

The breaking waves can be divided into three most commonly used types: spilling, plunging and surging breakers (Fig. 1). The relation between wave geometry and the breaker type was given by Galvin (1968).

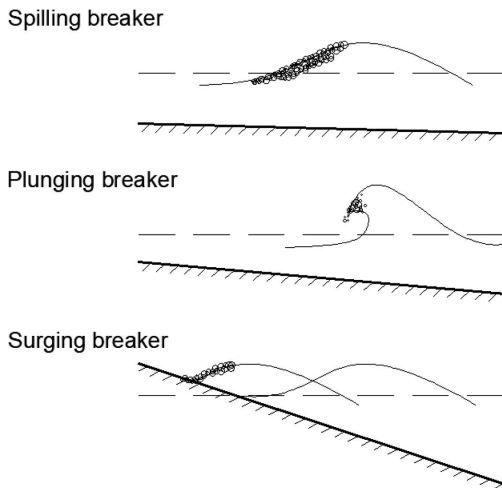


Figure 1. Breaker types.

Spilling breakers are categorized by the unstable wave front, where a spiral of water and air bubbles slides down the slope from the crest while travelling with the wave as a surface roller. Spilling breakers occur at very moderate beach slopes, where incoming waves are relatively steep. Besides beaches, spilling breakers can be found in deep water, where energy dissipation is an important part of the wind-generated waves.

In case of a plunging breaker, the crest of the wave moves forward and then overtops to the trough in front of it as a single controlled mass of water. The impact of the mass of water acts as the jet and generates a splash-up of water, which ensures the breaking process and further creates large vortices. This jet can reach the bottom and stir up a significant amount of sediment. Possible manners of producing the splash-up have been described by Peregrine (1983). Plunging breakers are found on steeper beach slopes, where incoming waves are less steep than on spilling breakers.

However, in surging breakers, it is the foot of the very steep beach slope that causes the wave crest to decrease and disappear rapidly, without giving wave time to become unstable.

Grouping into breaker types is done by the surf similarity parameter developed by Battjes (1974), which gives the ratio between the beach slope and the square root of the wave steepness.

After a wave-breaking in both spilling or plunging breaker, a wave transition occurs. In the case of the spilling breaker, the surface roller grows, and the wave height decreases rapidly. At the same time, the jet of water in front of the plunging breaker pushes up a relatively turbulent mass of water that continues the wave-breaking process. This area of the surf zone where in both cases the wave is changed from wave-breaking into a bore-like broken wave is called an outer part of the surf zone. In the inner part of the surf zone, waves can be described as a series of periodic bores (Svendsen, Madsen, & Hansen, 1978). An additional difference between the inner and the outer part is the ratio between the local wave height and the mean water depth, whereas in the outer part, it decreases from the value of near 0.8 at the point of wave-breaking to convert practically constant at about 0.5 in the inner zone.

It is required to gain further information about the experimental measurements of the breaking waves, which can be divided into two large categories. The first group is field measurements that give basic knowledge about the wave processes and their physical parameters. The second group is laboratory measurements that provide a more controlled environment for determining specific parameters for furthering empirical models.

Field measurements give the scale reference to laboratory measurements.

1.1 Field measurements

Field measurements are necessary for investigating methods to predict the geometric characteristics of breaking waves and breaking circumstances. In nature, physical measurements of individual waves are complex due to the wide range of wave heights, periods, directions and relative placement of the breaking point.

In the past, many researchers used photographic techniques with photo poles to observe wave properties in the surf zone. Maresca & Seibel (1976) monitored waves, water levels, and longshore currents with single and stereoscopic oblique-image analysis of films shot with 35 mm cameras. Suhayda & Pettigrew (1977) observed wave crest and trough elevations with a 16 mm movie camera to determine wave heights and wave celerity. Weishar & Byrne (1978) gathered information relative to breaking depth, plunge distance, breaking wave height and breaking wave classification using a 16 mm movie camera. Hotta & Mizuguchi (1980) observed water surface fluctuations with 11 synchronized 16 mm movie cameras. Holman & Guza (1984) detected the along-shore and temporal variation in wave runup with three synchronized movie cameras. Ebersole & Hughes (1986) monitored free surface elevation with 16 mm movie cameras. Advances in video remote sensors allow spatial resolution of individual breaking locations, wave period and height (Santel, Linder, & Heipke, 2004), (Benetazzo, 2006), (De Vries, De Schipper, Hill, & Stive, 2011), (Gal, Browne, & Lane, 2011), and (Holman & Haller, 2013).

In addition to photographic techniques, remote sensing methods are used. Those methods can be divided into non-directional wave measurements and directional wave and current measurements. The first group works with pressure transducers for field studies and includes seafloor mounted pressure sensors (Birkemeier, Donoghue, Long, Hathaway, & Baron, 1997), Ridd (1992), Saulter, Russell, Gallagher & Miles (2003), Arnaud, Mory, Abadie & Cassen (2009), Puleo, Faries, Davidson & Hicks (2010), and Puleo, Lanckriet & Blenkinsopp (2014). The second group works with velocity sensors for field studies and is in turn divided into the Eulerian method that measures the fluid flow at a fixed location through time and the Lagrangian method that follows fluid parcels through time and space. The Eulerian method includes Acoustic Doppler Current Profilers (ADCP)

(Terray, Brumley, & Strong, 1999), (Hansen, Carstensen, Christensen, & Aagaard, 2017), (Velasco & Polonichko, 2009), Acoustic Doppler Velocimeters (ADV) (MacVicar, Beaulieu, Champagne, & Roy, 2007), Electromagnetic Current Meters (EMCM) (Rodriguez, Sanchez-Arcilla, Redondo, & Mosso, 1999), (Elgar, Raubenheimer, & Guza, 2001), and Acoustic Doppler Profilers (ADP) (Senechal, et al., 2011), (Puleo, Lanckriet, & Wang, 2012). The Lagrangian method includes GPS-tracked drifters (Schmidt, et al., 2003), (MacMahan, Brown, & Thornton, 2009), (Austin, Masselink, Scott, & Russell, 2014).

Today, a breaking wave is often studied combining field measurements and a laboratory flume (Goda, 2010) or a numerical algorithm (Black & Rosenberg, 1992), (Shand, Bailey, & Shand, 2012). Throughout the years, various limitations have been imposed on the studies of breaking waves - height predictors are often based on regular waves rather than on irregular wave systems (MacCowan, 1894), (Weggel, 1972), (Battjes J., 1974), (Ostendorf & Madsen, 1979), (Seyama & Kimura, 1988), (Kamphuis, 1991), (Smith & Kraus, 1991), (Rattanapitikon & Shibayama, 2000), (Goda, 2010), or limitations of tank dimensions (Robertson, Hall, Nistor, & Zytner, 2013) etc.

1.2 Laboratory measurements

Extensive experimental work has focused on coastal hydrodynamics and sediment transport in the laboratories to understand complicated dynamics involved in accurate field measurements. However, since the size of most wave flumes is fairly limited, it is difficult to obtain adequately large values of the Reynolds number for modelling boundary layer dynamics. A simplified commonly used experimental setup, a U-shaped oscillating tunnel (U-tube), was suggested by Lundgren & Sorensen (1958), where the orbital motion in the test section differs from the real wave-induced flow by being entirely uniform in the along tube direction and the vertical axis of the orbit is nearly zero.

In real wave motion, the wall generated turbulence, as in the U-tube experiments, is complemented with the turbulence generated at the free surface, which is absent in the U-tube oscillating flow. The U-shape oscillatory wave motion is an acceptable solution for modelling characteristics of the wave bottom boundary layer on a constant water depth with regular non-breaking waves. However, the method is lacking accuracy on the sloping bottom with breaking waves, where the free surface generated turbulence can extend into a full water column. Studies by Ting & Kirby (1994), Ting & Kirby (1995), Ting & Kirby (1996), Chang & Liu (1999), and Liiv (2007) have reported laboratory measurements of velocities and turbulence intensities in periodic breaking waves. All of these measurements were recorded by a Laser Doppler Anemometer (LDA). The latest of these experiments reported by Liiv (2007) is revisited herein to make use of the novel unpublished experimental data.

1.3 Wave data analysis

1.3.1 Existing physical model

The physical model of the wave flume and preliminary data processing of the experimental tests of breaking waves on the sloping bottom developed at Tallinn University of Technology (TalTech) is described in detail by Liiv (2007). Essentially, findings of previous investigations on the bottom boundary layer (Fredsoe & Deigaard, 1992) in U-shaped oscillating tunnels were compared with new experimentally observed results produced in the TalTech wave flume, and it was concluded that calculations of semi-logarithmic dimensionless velocity distributions were significantly different from

those proposed previously. Also, the two-dimensional ensemble-averaged velocity components and turbulent kinetic energy fields are presented by Liiv & Lagemaa (2008).

Experimental studies of breaking waves with the propagation of regular waves over a uniformly sloping bottom were carried out in the 0.6 m wide, 0.6 m deep and 22 m long wave flume with a bottom slope of a constant 1 to 17 positioned on one end and a flap-type wave generator on the other end. The origin of the coordinate system as a reference point (RP) was taken at the still water height 0.3 m, where the inclined bottom of the flume begins. The wave flume is shown in Fig. 2.

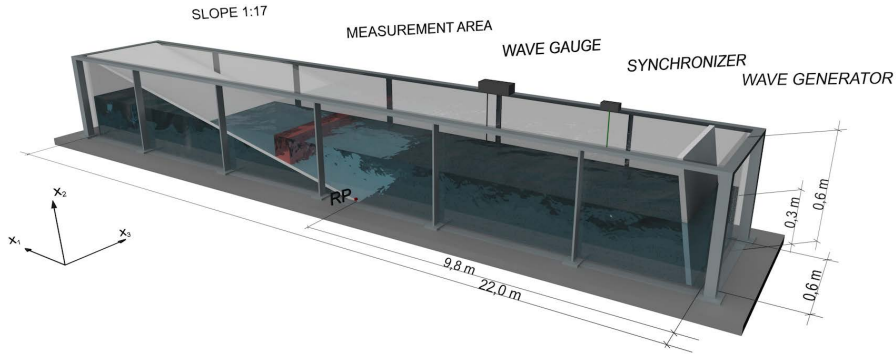


Figure 2. Bird's view of the wave flume: dimensions and notations.

Regular waves were created using a flap-type wave generator. The wave generator divided the constant depth of the water body into a regular waves area and a backwater area. Dumping of the wave generator backside waves was established inside the backwater area by using four layers of metal net with a size of 3 mm by 3 mm and 50 mm step in between the layers. A computer was used to produce signals for making regular sinusoidal waves controlled by the generator. Velocity profiles were measured in the breaking waves using a two-component Argon-ion LDA with an output power of 1.3 W. The measuring system was based on a two-dimensional tracker that operated in forward scatter fringe mode. The two velocity components were measured simultaneously. The flow velocity data was collected with a sampling frequency of 1 kHz during 151 wave periods. During the signal drop-out caused by air bubbles blocking the laser beams, the frequency tracker keeps the output voltage the same as the voltage just before the drop-out. To ensure signal dropping, the drop-out signal was recorded simultaneously with the output of regular channels. The synchronizing mechanism was made by a pair of electrodes and was positioned above the still water level in the constant depth section of the flume. Capacity probes in wave gauge were used to measure variations in the wave height. Table 1 shows the main characteristics of the regular wave in the experimental runs. Here T is the wave period, h_b is the water depth at the breaking point, including the change of the water level due to the wave set-up, d_b is still water depth at the breaking point, x_b is the horizontal coordinate of the breaking point measured from the reference point, H_0 is the deep water wave height, L_0 is the deep water wavelength, H_b is the wave height at the breaking point, and C_0 is the deep water wave celerity. The breaking point characteristics were calculated according to Komar & Gaughan (1972) and include the wave set-up. However, actual wave breaking started from profile no 1 in the outer part of the surf zone and lasted until profile no 19 (Table 2).

Table 1. Regular wave characteristics

T (s)	h_b (m)	d_b (m)	x_b (m)	H_0 (m)	L_0 (m)	H_b (m)	C_0 (m s ⁻²)
2.03	0.106	0.111	2.90	0.072	6.0	0.118	1.72

As the LDA system allows measurements at one point, the measurements were repeated over 29 profiles along the slope. The measuring step in the vertical direction was 1 mm in the near-bed zone, 3 mm in the intermediate zone and 2 mm in the zone affected directly by the water surface motion. The closest measurement point to the bottom was 0.05 mm above the rigid bed of the slope. The parameters observed in the experimental runs are presented in Table 2.

Table 2. Location of measuring points and corresponding wave parameters

Profile no	Distance from the reference point RP (m)	Still water depth d (m)	Water depth with wave set-up h (m)	Wave celerity C (m s ⁻²)
1	2.65	0.129	0.127	1.117
2	2.66	0.128	0.127	1.115
3	2.67	0.128	0.126	1.111
4	2.68	0.127	0.125	1.108
5	2.69	0.126	0.124	1.104
6	2.70	0.125	0.124	1.101
7	2.71	0.125	0.123	1.098
8	2.72	0.124	0.122	1.094
9	2.73	0.123	0.121	1.091
10	2.74	0.123	0.121	1.090
11	2.75	0.122	0.120	1.086
12	2.76	0.121	0.119	1.082
13	2.77	0.120	0.119	1.079
14	2.78	0.120	0.118	1.077
15	2.79	0.119	0.117	1.071
16	2.80	0.118	0.116	1.069
17	2.81	0.118	0.115	1.064
18	2.82	0.117	0.114	1.059
19	2.91	0.110	0.104	1.012
20	2.94	0.108	0.104	1.010
21	2.97	0.106	0.102	1.001
22	3.00	0.104	0.101	0.997
23	3.03	0.102	0.100	0.990
24	3.06	0.100	0.099	0.983
25	3.09	0.098	0.097	0.975
26	3.12	0.095	0.095	0.964
27	3.15	0.093	0.093	0.955
28	3.18	0.091	0.091	0.944
29	3.21	0.089	0.089	0.933

During experimental runs, horizontal and vertical components, the corresponding signal drop-outs, water level variation, and the signal from the synchronizing mechanism were stored. To determine the ensemble-averaged unsteady mean velocity and velocity fluctuation, data was collected for 151 waves.

1.3.2 Measurement data analysis

Preliminary data collecting and processing was done by Liiv (2007) where the flow velocity was divided into modified ensemble-averaged mean velocity according to Petti & Longo (2001) and the velocity fluctuating component. However, all in-depth raw-data analysis with smoothing according to (Zarchan & Musoff, 2000) and further processing was done by the thesis author. For author's **Publication I**, profiles no 1, 19 and 27 were chosen to analyze the shear velocity changes over the surf zone and at the different timesteps. For author's **Publication II**, profile no 13 was chosen to analyze eddy viscosity changes in time and space. For author's **Publications III and IV**, three neighbouring profiles no 16, 17 and 18 were chosen to analyze the modified eddy velocity changes during the breaking waves.

Wave patterns are characterized by the mean free surface displacement within the wave period (Fig. 3) along with the chosen profiles (see Table 2), normalized by the local time average water depth. According to Fig. 3, wave breaking appears from 0.7 to 0.9 of the dimensionless wave periods. Profile no 16 is positioned in deeper water as compared to the position of profile no 17, which is positioned in deeper water than the position of profile no 18 on the slope.

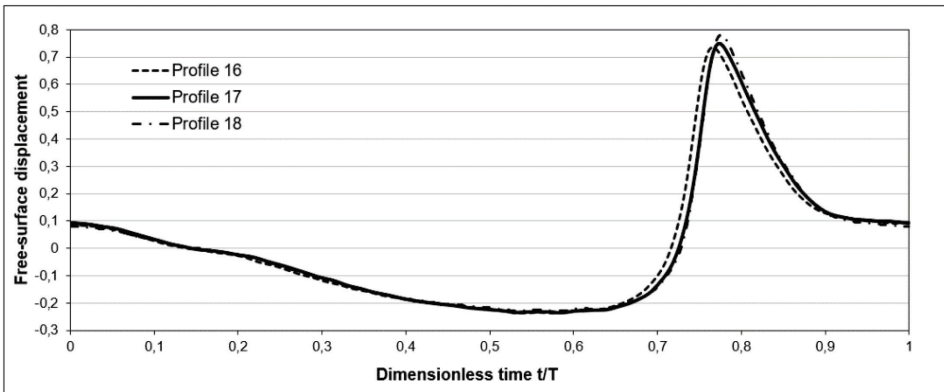


Figure 3. Mean free-surface displacement for three profiles.

The following figures show the measured wave characteristics on five different heights at profile no 17: Fig. 4 on 0.067 m; Fig. 5 on 0.052 m; Fig. 6 on 0.040 m; Fig. 7 on 0.028 m, and Fig. 8 on 0.006 m on the sloping bottom. These heights were chosen because 0.006 m and 0.067 m were the closest measuring heights to the bottom and to the surface, respectively. The rest of the measuring heights are at the equal distances between the two.

Section a) in the figures shows $\langle U_1 \rangle$ as horizontal velocity (shown by the continuous curve) and $\langle U_2 \rangle$ as vertical velocity (shown by the dashed curve), section b) shows $\langle u_1 \rangle$ as horizontal velocity fluctuation (shown by the continuous curve) and $\langle u_2 \rangle$ as vertical velocity fluctuation (shown by the dashed curve), section c) shows $\frac{\partial \langle u_1 \rangle}{\partial x_1}$ as horizontal velocity gradients along the channel direction (shown by the continuous curve) and

$\frac{\partial \langle U_1 \rangle}{\partial x_2}$ as horizontal velocity gradient in the channel vertical direction (shown by the dashed curve), and section d) shows $\frac{\partial \langle U_2 \rangle}{\partial x_1}$ as vertical velocity gradient along the channel direction (shown by the continuous curve) and $\frac{\partial \langle U_2 \rangle}{\partial x_2}$ as vertical velocity gradient along the channel vertical direction (shown by the dashed curve).

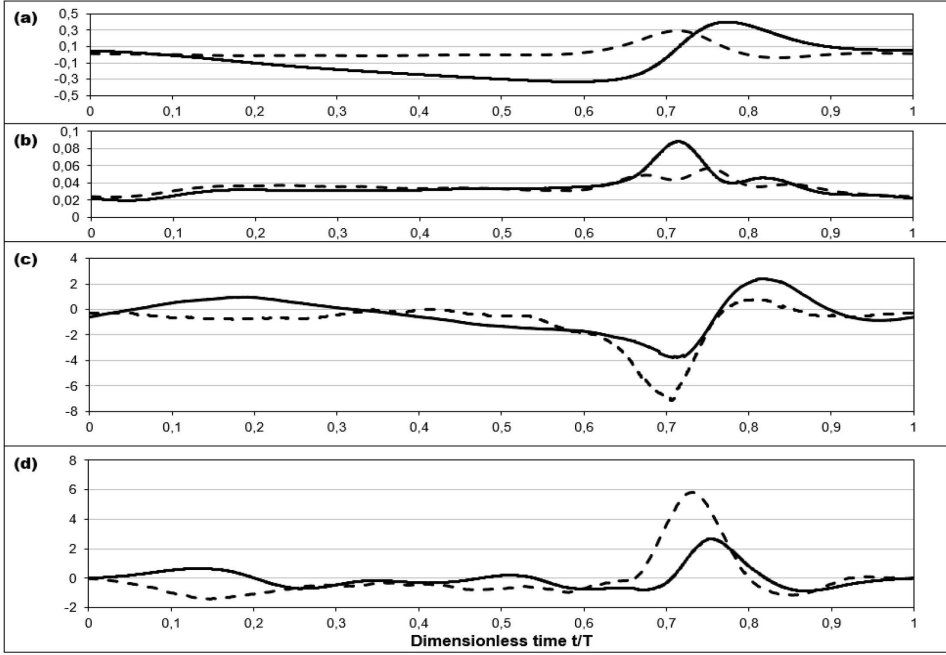


Figure 4. Wave characteristics 0.067 m above the sloping bottom from the measurements: a) horizontal velocity $\langle U_1 \rangle$ ($m s^{-1}$) (continuous curve) and vertical velocity $\langle U_2 \rangle$ ($m s^{-1}$) (dashed curve); b) horizontal velocity fluctuation $\langle u_1 \rangle$ ($m s^{-1}$) (continuous curve) and vertical velocity fluctuation $\langle u_2 \rangle$ ($m s^{-1}$) (dashed curve); c) horizontal velocity gradients along the channel direction $\frac{\partial \langle U_1 \rangle}{\partial x_1}$ (s^{-1}) (continuous curve) and horizontal velocity gradient in the channel vertical direction $\frac{\partial \langle U_1 \rangle}{\partial x_2}$ (s^{-1}) (dashed curve); d) vertical velocity gradient along the channel direction $\frac{\partial \langle U_2 \rangle}{\partial x_1}$ (s^{-1}) (continuous curve) and vertical velocity gradient along the channel vertical direction $\frac{\partial \langle U_2 \rangle}{\partial x_2}$ (s^{-1}) (dashed curve).

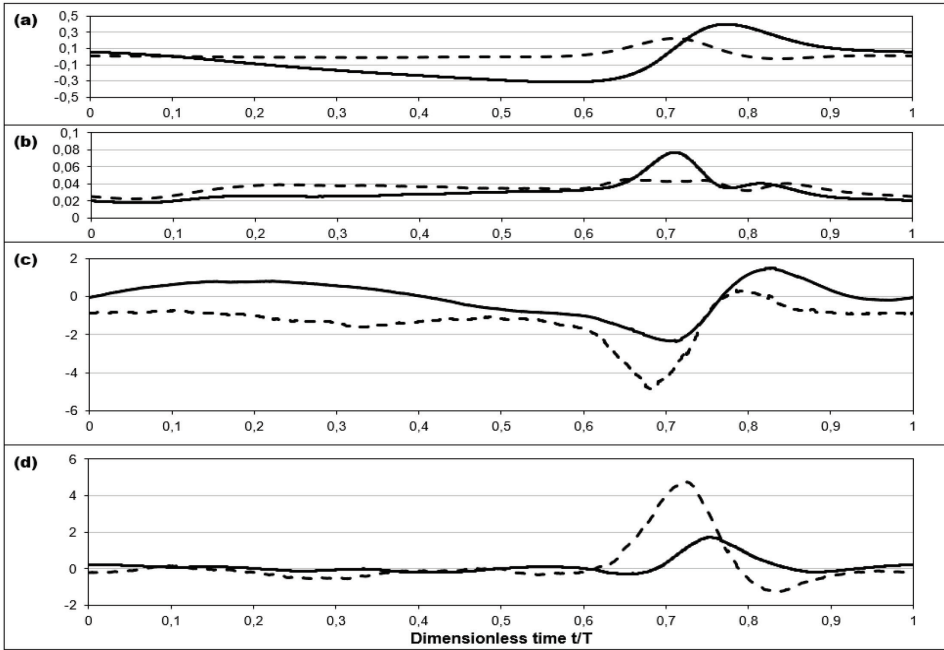


Figure 5. Wave characteristics 0.052 m above the sloping bottom from the measurements: a) velocities $\langle U_1 \rangle$ and $\langle U_2 \rangle$ ($m s^{-1}$); b) fluctuations $\langle u_1 \rangle$ and $\langle u_2 \rangle$ ($m s^{-1}$); c) velocity gradients $\frac{\partial \langle U_1 \rangle}{\partial x_1}$ and $\frac{\partial \langle U_2 \rangle}{\partial x_1}$ (s^{-1}); d) velocity gradients $\frac{\partial \langle U_1 \rangle}{\partial x_2}$ and $\frac{\partial \langle U_2 \rangle}{\partial x_2}$ (s^{-1}) (explanation to axis titles under Fig. 4).

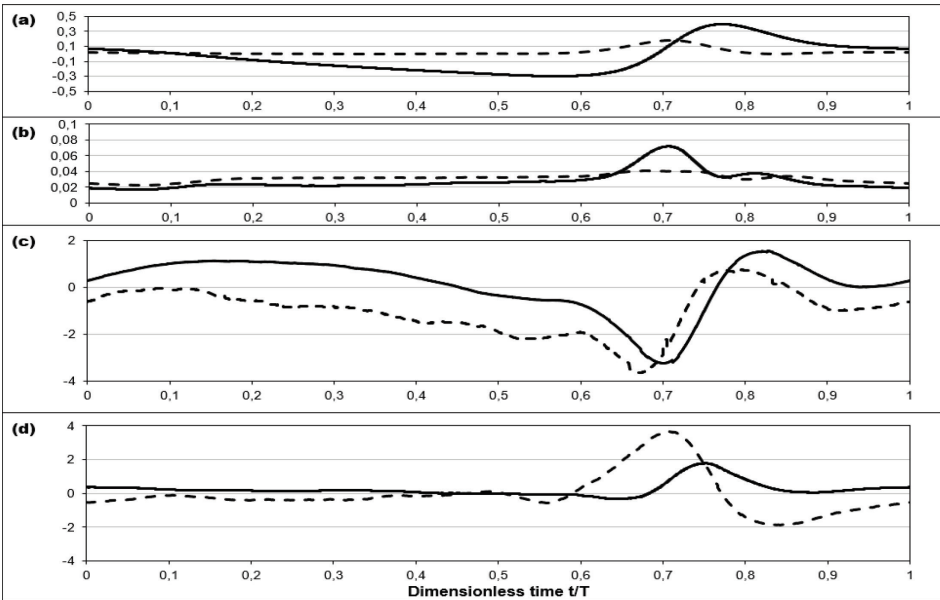


Figure 6. Wave characteristics 0.040 m above the sloping bottom from the measurements: a) velocities $\langle U_1 \rangle$ and $\langle U_2 \rangle$ ($m s^{-1}$); b) fluctuations $\langle u_1 \rangle$ and $\langle u_2 \rangle$ ($m s^{-1}$); c) velocity gradients $\frac{\partial \langle U_1 \rangle}{\partial x_1}$ and $\frac{\partial \langle U_2 \rangle}{\partial x_1}$ (s^{-1}); d) velocity gradients $\frac{\partial \langle U_1 \rangle}{\partial x_2}$ and $\frac{\partial \langle U_2 \rangle}{\partial x_2}$ (s^{-1}) (explanation to axis titles under Fig. 4).

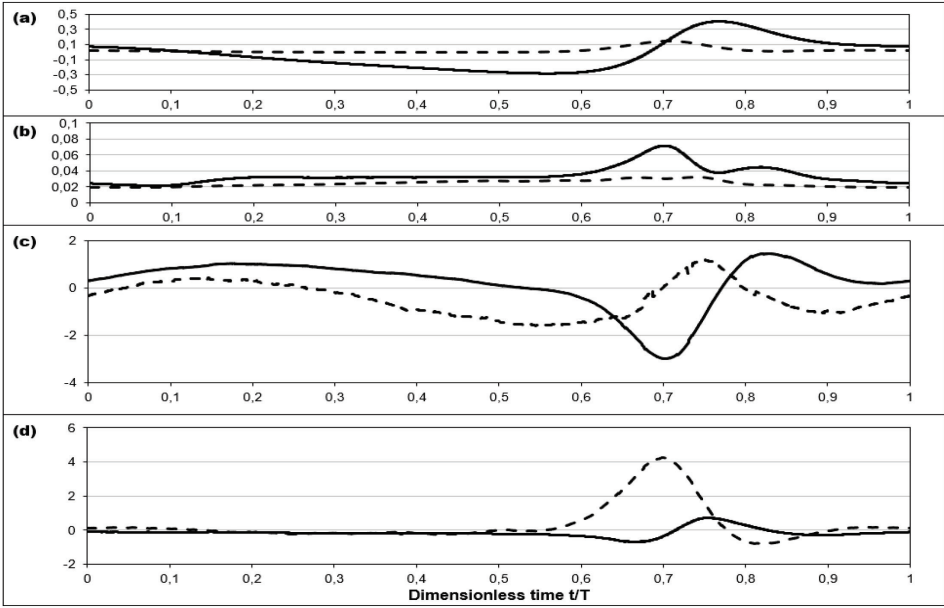


Figure 7. Wave characteristics 0.028 m above the sloping bottom from the measurements: a) velocities $\langle U_1 \rangle$ and $\langle U_2 \rangle$ ($m s^{-1}$); b) fluctuations $\langle u_1 \rangle$ and $\langle u_2 \rangle$ ($m s^{-1}$); c) velocity gradients $\frac{\partial \langle U_1 \rangle}{\partial x_1}$ and $\frac{\partial \langle U_1 \rangle}{\partial x_2}$ (s^{-1}); d) velocity gradients $\frac{\partial \langle U_2 \rangle}{\partial x_1}$ and $\frac{\partial \langle U_2 \rangle}{\partial x_2}$ (s^{-1}) (explanation to axis titles under Fig. 4).

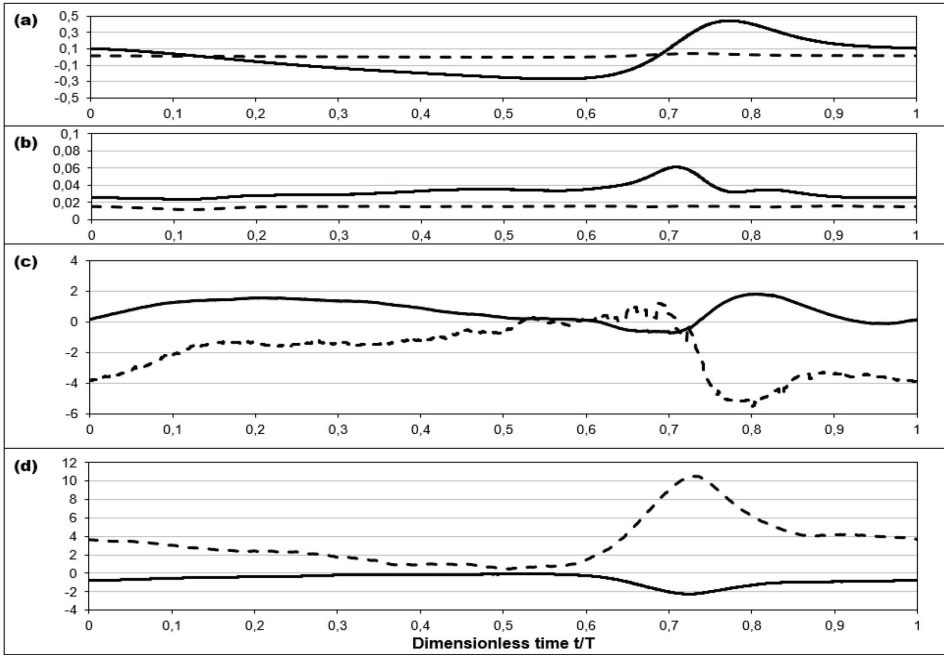


Figure 8. Wave characteristics 0.006 m above the sloping bottom from the measurements: a) velocities $\langle U_1 \rangle$ and $\langle U_2 \rangle$ ($m s^{-1}$); b) fluctuations $\langle u_1 \rangle$ and $\langle u_2 \rangle$ ($m s^{-1}$); c) velocity gradients $\frac{\partial \langle U_1 \rangle}{\partial x_1}$ and $\frac{\partial \langle U_1 \rangle}{\partial x_2}$ (s^{-1}); d) velocity gradients $\frac{\partial \langle U_2 \rangle}{\partial x_1}$ and $\frac{\partial \langle U_2 \rangle}{\partial x_2}$ (s^{-1}) (explanation to axis titles under Fig. 4).

Table 3 shows the maximum and minimum values of velocities and velocity fluctuations. The highest horizontal velocity $\langle U_1 \rangle$ values are directly under the wave crest while the lowest values are directly under the wave trough. $\langle U_1 \rangle$ values are near-constant throughout the water depth, varying from the highest 0.395 to 0.444 m s^{-1} to the lowest -0.332 to -0.269 m s^{-1} . $\langle U_1 \rangle$ value amplitude is between 0.687 to 0.732 m s^{-1} . The horizontal velocity fluctuation $\langle u_1 \rangle$ values are more intense under the surface roller, values increasing from the bottom boundary layer 0.061 m s^{-1} to the surface boundary layer 0.088 m s^{-1} .

The highest vertical velocity $\langle U_2 \rangle$ values are directly under the surface roller while there is no distinct local minimum throughout the wave period. $\langle U_2 \rangle$ values increase from near-zero from the bottom boundary layer to the amplitude of 0.290 m s^{-1} surface boundary layer. The vertical velocity fluctuation $\langle u_2 \rangle$ values increase from 0.012 m s^{-1} from the bottom boundary layer to 0.057 m s^{-1} to the surface boundary layer.

Furthermore, the negative or positive sign before velocities states their direction inside the oscillating elliptical motion. High values of horizontal velocity are associated with the increasing wave celerity during and after breaking and those water particles are drawn from the wave trough into the crest to maintain continuity.

Table 3. Maximum and minimum values of velocities and velocity fluctuations

	$\langle U_1 \rangle_{max}$ (m s^{-1})	$\langle U_1 \rangle_{min}$ (m s^{-1})	$\langle U_2 \rangle_{max}$ (m s^{-1})	$\langle U_2 \rangle_{min}$ (m s^{-1})	$\langle u_1 \rangle_{max}$ (m s^{-1})	$\langle u_1 \rangle_{min}$ (m s^{-1})	$\langle u_2 \rangle_{max}$ (m s^{-1})	$\langle u_2 \rangle_{min}$ (m s^{-1})
Fig.3	0.400	-0.332	0.290	-0.041	0.088	0.020	0.057	0.024
Fig.4	0.400	-0.314	0.224	-0.024	0.077	0.018	0.045	0.023
Fig.5	0.395	-0.298	0.178	-0.006	0.072	0.017	0.041	0.023
Fig.6	0.405	-0.282	0.142	-0.002	0.072	0.021	0.033	0.019
Fig.7	0.444	-0.269	0.044	0.001	0.061	0.024	0.016	0.012

Table 4 shows the maximum and minimum values of velocity gradients. Negative sign before the velocity gradient means that the velocity is slowing down, positive sign before the velocity gradient refers to the velocity accelerating. The highest acceleration takes place on the bottom boundary layer by the vertical velocity gradient in the channel vertical direction, creating uplifting motion towards the surface roller. The slowest motion takes place on the surface boundary layer by the horizontal velocity gradient in the channel vertical direction, under the highest point of the wave crest.

Table 4. Maximum and minimum values of velocity gradients

	$\frac{\partial \langle U_1 \rangle}{\partial x_1}_{max}$ (s^{-1})	$\frac{\partial \langle U_1 \rangle}{\partial x_1}_{min}$ (s^{-1})	$\frac{\partial \langle U_1 \rangle}{\partial x_2}_{max}$ (s^{-1})	$\frac{\partial \langle U_1 \rangle}{\partial x_2}_{min}$ (s^{-1})	$\frac{\partial \langle U_2 \rangle}{\partial x_1}_{max}$ (s^{-1})	$\frac{\partial \langle U_2 \rangle}{\partial x_1}_{min}$ (s^{-1})	$\frac{\partial \langle U_2 \rangle}{\partial x_2}_{max}$ (s^{-1})	$\frac{\partial \langle U_2 \rangle}{\partial x_2}_{min}$ (s^{-1})
Fig.3	2.384	-3.768	0.781	-7.174	2.678	-0.882	5.808	-1.396
Fig.4	1.528	-2.378	0.332	-4.859	1.722	-0.288	4.737	-1.240
Fig.5	1.564	-3.231	0.762	-3.651	1.803	-0.333	3.682	-1.869
Fig.6	1.430	-3.004	1.191	-1.616	0.720	-0.668	4.271	-0.768
Fig.7	1.843	-0.748	1.252	-5.507	-0.053	-2.301	10.572	0.459

2 Turbulence models in coastal engineering

Wave breaking on the sloping bottom in shallow waters is defined as the transformation of the irrotational wave motion into the turbulent rotational flow. This can be observed for plunging breaking waves, when part of the wavefront becomes unstable and overturns into the wave trough in front of it. This drastic transition of large scale vortices inside the wave shape occurs in the outer region of the surf zone (Svendsen, Madsen, & Hansen, 1978). Meanwhile, in the inner region, the flow is very similar to a hydraulic jump or to a moving bore.

Regarding hydrodynamics, in the outer region of the surf zone, wave energy is dissipated dominantly due to the large-scale vortices (Battjes, 1988). However, inside the inner region of the surf zone, the loss of wave energy is governed by the bore-like broken waves that transform turbulent motion to small-scale vortices.

To model the turbulence generated by the wave-breaking in the surf zone, the estimation of the turbulence dissipation rate of wave energy is a primary aim. Turbulent dissipation rate is taken as the basis for the turbulent kinetic energy. First investigations for energy dissipation in the breaking waves were conducted by Le Mehaute, Divoky, & Lin (1968) and by Divoky, Le Mehaute, & Lin (1970). The relation between turbulent kinetic energy and the rate of its dissipation was reported by Launder & Sharma (1974).

Based on visual observation, Peregrine & Svendsen (1978) described the nature of the flow in a quasi-steady breaking wave; their conclusion was that the turbulence is generated primarily in the toe region of the bore and spreads downstream and dissipates in awake. Experimentally proved by Battjes & Sakai (1980) and by Stive & Wind (1982), this applies to the inner region, while the outer region needs further investigation.

You, Wilkinson & Nielsen (1992) assumed that eddy viscosity in turbulent oscillatory boundary layers can be a time-independent and real-valued parameter. Until then, several time-constant eddy viscosity profiles were proposed by Kajiwara (1968), Brevik (1981), Myrhaug (1982) for oscillatory flows and by Lundgren (1972), Smith (1977), Grant & Madsen (1979) for combined steady and oscillatory flows. More specific details about different assumptions were made in Fredsoe & Deigaard (1992). Even though, the concept of time-independents and real-valuing, the parabolic-uniform profile developed by Myrhaug (1982) was further used by Liu & Sato (2006) and Van Rijn (2007). Also, the exponential-linear profile developed by Gelfenbaum & Smith (1986) and Beach & Sternberg (1988) was further used by Hsu & Jan (1998) and Absi (2010).

To further previous empirical works that give a more flexible and accurate description of the turbulence in breaking wave, Briganti, Musumeci, Bellotti, Brocchini, & Foti (2004) suggested that more specific eddy viscosity profiles are needed for wave modelling.

The turbulence intensity in a thin bottom boundary layer can be strongly unsteady and very high valued. Justesen (1985) was the first to investigate the use of turbulence modelling in the turbulent wave boundary layer.

Studies of turbulence properties have established the importance of bed shear stress on the bottom boundary layer in the surf zone. While Deigaard (1993) measured the time variation of the bed shear stress and showed the effect of the turbulence produced by wave-breaking, Cox, Kobayashi & Okayasu (1996) concluded that the bottom friction factor for quasi-steady breaking can be estimated from a quadratic

friction equation based on the measured horizontal velocity with the estimated shear velocity above the bottom boundary layer.

2.1 Classification of turbulence models

Eddy viscosity is not a fluid property; it depends on the state of the turbulence, therefore, turbulence models can be divided into several groups (see Fig. 9). This chapter concentrates on Reynolds-Averaged Navier-Stokes (RANS) models. Computation models, like Large Eddy Simulation (LES) and Direct Numerical Simulation (DNS), will be addressed in Chapter 3.

RANS models can be divided into linear (EVM) and non-linear eddy viscosity models (NLEVM), referring to the tensor used for the model. The linear models accept a Boussinesq approach between the mean strain rate tensor and the turbulent stresses. The nonlinear models adopt a higher-order tensor representation connecting in one case powers of the mean velocity gradient tensor or in another case, combinations of the rotation rate tensors and mean strain rate.

Under 1st order, there are 0-equation models, also known as algebraic models. Under this category are constant eddy viscosity, mixing length (Prandtl, 1925) and Prandtl's free shear layer (Prandtl, 1942) models. Also, Cebeci-Smith model (Smith & Cebeci, 1967), Baldwin-Lomax model (Baldwin & Lomax, 1978) and Johnson-King model (Johnson & King, 1985) belong to this group. 1-equation models include Kolmogorov-Prandtl k -equation model, even though they introduced it independently, the same conclusions were reached in Kolmogorov (1942) and Prandtl & Wieghardt (1945). Bradshaw's model (Bradshaw, Ferriss, & Atwell, 1967) is also a 1-equation model where heat and mass transfer calculations and buoyancy effects are related. Also, Baldwin-Barth's model (Baldwin & Barth, 1990) and Spalart-Allmaras' model (Spalart & Allmaras, 1994) belong to this group. 2-equation turbulence models are the most common models. $k - \varepsilon$ and $k - \omega$ models are commonly used for most types of engineering problems, and they are based on Boussinesq's eddy viscosity assumption. Considering their popularity, further developments in both cases are common.

Non-linear eddy viscosity models, under 2nd order, are featured by the polynomial tensor representation for the second-moments or Reynolds stresses. Explicit algebraic Reynolds Stress models attempt to obtain explicit solutions to the algebraic stress models. Pope (1975) developed the model for two-dimensional flows, which was later extended for three-dimensional flows by Gatski & Speziale (1993). Algebraic stress models have been further developed by Apsley & Leschziner (1998) and Abe, Jang & Leschziner (2003). Regarding to the Reynolds stress anisotropy, the first quadratic model was proposed by Speziale (1987) and then by Nisizima & Yoshizawa (1987). The quadratic model has been further improved by Rubinstein & Barton (1990), Myong & Kasagi (1990) and Shih, Zhu & Lumley (1993). The cubic model was developed by Suga (1995), Craft, Launder & Suga (1996) and Craft, Launder & Suga (1997).

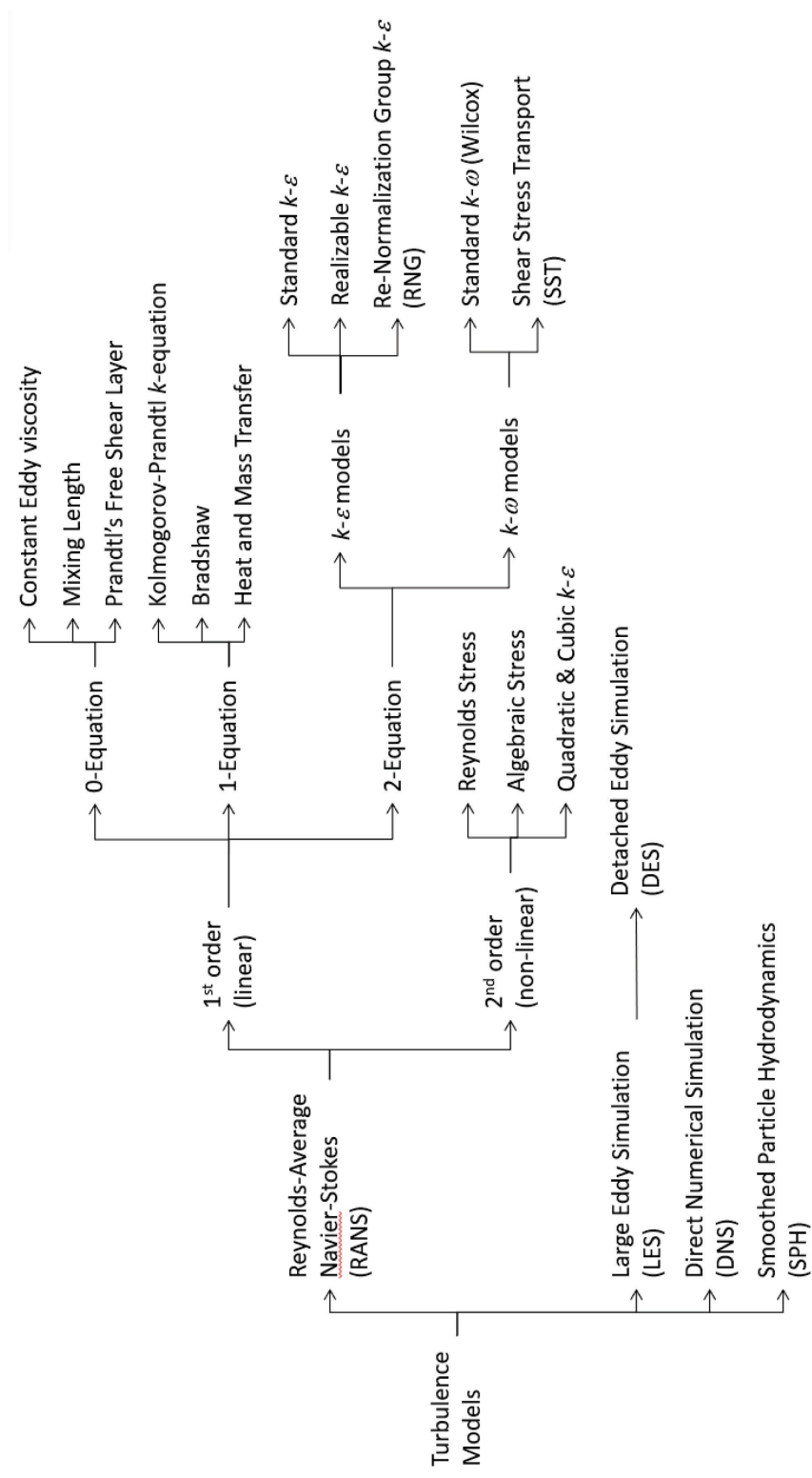


Figure 9. Classification of turbulence models.

2.2 Theoretical model

2.2.1 The turbulent-viscosity hypothesis

The first proposal for modelling the turbulence was suggested by Boussinesq (1877) and is known as Boussinesq's eddy viscosity assumption, which assumes that it is possible to model the momentum transfer produced by turbulent eddies with an eddy viscosity. Boussinesq's assumption states that the Reynolds stress tensor is related to the mean strain rate tensor.

According to this, an essential association of the linear eddy viscosity with the mean flow straining field can be determined through the Reynolds stresses at any given point and time inside of the turbulent flow field. The Reynolds stress anisotropy is

$$a_{ij} \equiv \langle u_i u_j \rangle - \frac{2}{3} k_T \delta_{ij}. \quad (1)$$

The author has adopted an approach with compressible fluid, as wave breaking mixes water and thus air results in a compressible medium. Here Reynolds stresses are defined as:

$$\begin{aligned} -\langle u_i u_j \rangle &= -\frac{2}{3} k_T \delta_{ij} + \nu_T \left(\frac{\partial \langle U_i \rangle}{\partial x_j} + \frac{\partial \langle U_j \rangle}{\partial x_i} - \frac{2}{3} \frac{\partial \langle U_k \rangle}{\partial x_k} \delta_{ij} \right) = \\ &= -\frac{2}{3} \left(k_T + \nu_T \frac{\partial \langle U_k \rangle}{\partial x_k} \right) \delta_{ij} + \nu_T \left(\frac{\partial \langle U_i \rangle}{\partial x_j} + \frac{\partial \langle U_j \rangle}{\partial x_i} \right), \end{aligned} \quad (2)$$

where k_T is the turbulent kinetic energy, δ_{ij} is the Kronecker delta and ν_T is the eddy viscosity. Reynolds stress is proportional to the mean rate of the strain, where the positive scalar coefficient ν_T is the eddy viscosity. It is only the anisotropic component a_{ij} that is effective in transporting momentum, while the isotropic component $\frac{2}{3} k_T$ can be absorbed in a modified mean pressure. Inclusion of $\frac{2}{3} \rho k_T \delta_{ij}$ into the Eq. (2) is required for tensorial algebra purposes when solving the transport equation for the turbulent kinetic energy. The total viscous stresses are given by augmenting the molecular viscosity with an eddy viscosity (Bertin, Periaux, & Ballmann, 1992).

2.2.2 Channel flow case

Considering a statistically two-dimensional flow in which statistics are independent of the cross-channel coordinate x_3 (see Fig. 2), the Reynolds stress tensor for a turbulent flow in the flume may be approximated as:

$$\langle u_i u_j \rangle = \begin{bmatrix} \langle u_1^2 \rangle & \langle u_1 u_2 \rangle & 0 \\ \langle u_1 u_2 \rangle & \langle u_2^2 \rangle & 0 \\ 0 & 0 & \langle u_3^2 \rangle \end{bmatrix}, \quad (3)$$

which applies to the turbulent channel flow. In the present study, bottom height increases along the channel coordinate x_1 direction and in the channel vertical coordinate x_2 direction.

In a two-dimensional turbulent oscillatory flow, the instantaneous local velocity components (U_1 for the horizontal component, U_2 for the vertical component) may be decomposed into phase ensemble components ($\langle U_1 \rangle, \langle U_2 \rangle$) and turbulent components ($\langle u_1 \rangle, \langle u_2 \rangle$), e.g.,

$$\vec{U} = \overline{\langle U \rangle} + \overline{\langle u \rangle}. \quad (4)$$

The vertically averaged (over three measurement points) variables are functions of time and distance, e.g.,

$$\langle U_i \rangle = \frac{1}{\Delta x_j} \int_{x_j}^{x_j + \Delta x_j} U_i dx_j. \quad (5)$$

Reynolds stress anisotropy, Eq. (1), can be applied to derive a formula for the eddy viscosity coefficient that results from the non-diagonal elements:

$$\nu_T = \frac{-\langle u_1 u_2 \rangle}{\frac{\partial \langle U_1 \rangle}{\partial x_2} + \frac{\partial \langle U_2 \rangle}{\partial x_1}}, \quad (6)$$

and from the diagonal elements:

$$\nu_T = \frac{\frac{2}{3} k_T - \langle u_i u_i \rangle}{2 \frac{\partial \langle U_i \rangle}{\partial x_i} - \frac{2}{3} \left(\frac{\partial \langle U_1 \rangle}{\partial x_1} + \frac{\partial \langle U_2 \rangle}{\partial x_2} \right)}. \quad (7)$$

It should be noted that Eq. (6) can be used in the case of compressible and also incompressible fluid, and Eq. (7) can be used only in the case of compressible fluid or in the case of incompressible fluid if the compression rate is zero, i.e. $\nabla \cdot \langle \vec{U} \rangle = 0$.

The turbulent kinetic energy

$$k_T \approx \frac{1}{2} (\langle u_1^2 \rangle + \langle u_2^2 \rangle + \langle u_3^2 \rangle) \quad (8)$$

is approximated for the two-dimensional turbulent oscillatory flow as:

$$k_T \approx \frac{1}{2} (\langle u_1^2 \rangle + \langle u_2^2 \rangle), \quad (9)$$

where the turbulent kinetic energy calculation is simplified due to conditions

$$\langle u_1 \rangle > \langle u_2 \rangle \gg \langle u_3 \rangle. \quad (10)$$

Turbulent production term used in the turbulent kinetic energy equation, is

$$\mathcal{P} = -\langle u_i u_j \rangle \frac{\partial \langle U_i \rangle}{\partial x_j} \quad (11)$$

Assuming that in the quasi-steady breaking wave, the bottom surface is hydraulically smooth such that the height of the surface roughness is insignificant to affect the flow, we suggest that the velocity profile near the bottom depends only on the parameters that are relevant near the bottom and does not depend on the free-stream velocity or the thickness of the flow. So, the shear velocity is

$$U_* = \sqrt{\frac{\tau_b}{\rho}}, \quad (12)$$

where τ_b is the bottom shear stress and ρ is the density of water.

The bottom shear stress is calculated:

$$\tau_b = \mu \frac{\partial \langle U_i \rangle}{\partial x_j}, \quad (13)$$

where μ is the dynamic viscosity of the fluid and $\frac{\partial \langle U_i \rangle}{\partial x_j}$ is the velocity gradient on the bottom.

2.3 Empirical models

In the momentum transport models, such as two-equation models, e.g., $k - \varepsilon$ model, velocity and length are related to the turbulent kinetic energy as well as to the rate at which energy is dissipated. Even in relatively simple flows, the eddy viscosity concept can fail due to regions inside of which the shear stress and the velocity gradient of the flow have opposite signs (cf. Eq. (6)) (Rodi, 1980).

In 2-equation models, the most widely used $k - \varepsilon$ turbulence closures model was suggested by (Launder & Sharma (1974):

$$\nu_T = C_\mu \frac{k_T^2}{\varepsilon}, \quad (14)$$

where $C_\mu = 0.09$ is an empirical constant of proportionality, which states that at high Reynolds number, the rates of production and dissipation are of a similar order of magnitude. Turbulent kinetic energy k_T is taken according to Eq. (9) and turbulence dissipation rate due to viscous loss:

$$\varepsilon = 2\nu \overline{S_{ij} S_{ij}}, \quad (15)$$

where $\overline{S_{ij}} = \frac{1}{2} \left(\frac{\partial \langle U_i \rangle}{\partial x_j} + \frac{\partial \langle U_j \rangle}{\partial x_i} \right)$. At the same time, turbulence dissipation rate for 1-equation turbulent model, is

$$\varepsilon = \frac{C_\mu^{3/4} k_T^{3/2}}{L}, \quad (16)$$

where L is the turbulence length scale.

Puleo, Mouraenko & Hanes (2004) concluded that comparing laminar, linear, parabolic eddy viscosities, $k - 1$ -equation turbulence closure, $k - \varepsilon$ and $k - \omega$ 2-equation turbulence closures with laboratory measurements, the eddy viscosity models where the vertical profile shape is specified performs just as well as other turbulence closures. It was found that the linear profile of eddy viscosity produces slightly better results than the $k - \omega$ model on rough beds. However, $k - \omega$ result provides the best prediction of the bed stress. While, in terms of turbulent kinetic energy, the k and $k - \omega$ showed relatively high predictability.

Woelke (2007) concluded that in flows with adverse pressure gradients, all turbulence models based on the turbulence dissipation rate overpredict the turbulent length scale. That issue is improved with Realizable $k - \varepsilon$ model and provides better performance under strong adverse pressure gradients, recirculations and separations. However, RNG $k - \varepsilon$ model handles only low-Reynolds numbers in near-wall flows. At the same time, all $k - \varepsilon$ models provide excellent results in free shear flows. Comparing $k - \omega$ to $k - \varepsilon$ models, the first one performs accurately near walls, leading to improved wall shear stress and heat transfer predictions, while it fails in free shear flows.

According to Menter (1994), the Shear Stress Transport (SST) model takes advantage of the standard $k - \varepsilon$ model's better performance in free shear flows and $k - \omega$ model's better performance in near-wall shear flows and is tested mainly for aerodynamic applications.

Toorman (2000) found that the near-wall damping effects that are taken account in the $k - \varepsilon$ model by multiplication of the constant C_μ have been developed only for

smooth walls and are dependent on the Reynolds number, which leads to wrong values of the wall stress.

2.4 Development of the calculation method

The measurement data described in Section 1.3.2 was used in further calculations. Author's **Publication I** analyzed shear velocity changes on the bottom and surface boundary over the surf zone and at the different timesteps. For author's **Publication II**, the measured data was used to calculate eddy viscosity changes in time and space. As Boussinesq's eddy viscosity assumption does not allow negative values of this quantity, the result is a loss of mean mechanical energy and a gain of turbulent kinetic energy. In addition, in the case of measured velocity, peaked values of eddy viscosity are filtered out, as they are caused by mathematical instability due to division by zero, modifications in the used theory were required. In author's **Publication III**, turbulent kinetic energy and averaged eddy velocity based on modified data were calculated and analyzed.

2.4.1 Processing of experimental results

The approach presented by Briganti, Musumeci, Bellotti, Brocchini, & Foti (2004) was tested by using the formulae Eq. (6) and Eq. (7) in the present study, where the mean velocity and its derivatives were specifically treated. The irrotational flow was removed from the measured velocity by removing the oscillating part of the flow from the mean velocity and modifying its derivatives fields by the depth-dependent and time-independent constants in a oscillating frame of reference. So, the velocity corresponding to a rotational part was obtained by subtracting the velocity above the bottom boundary layer from the local velocity, and the mean velocity gradient components were modified by functions $A(x_2)$, $B(x_2)$, $C(x_2)$, $D(x_2)$, which depend on the distance from the bottom. In present approach, the used functions follow some conditions, i.e.,

$$A(x_2) \ll B(x_2) \quad (17)$$

and

$$C(x_2) = D(x_2). \quad (18)$$

The latter indicates that the specific correction functions correspond to the irrotational flow of the velocity field. In other words, according to the approach by Briganti, Musumeci, Bellotti, Brocchini, & Foti (2004), the rotational velocity can be expressed as

$$\overline{\langle U \rangle}_p = \overline{\langle U \rangle}_b + a_1 x_2 \hat{a}_1 + a_2 x_2^2 \hat{a}_2, \quad (19)$$

where coefficients $a_1 = f_1(A, B, C, D)$ and $a_2 = f_2(A, B, C, D)$ and unit vectors are \hat{a}_1 and \hat{a}_2 . It should be mention here that in the present model higher order velocity profiles are considered, i.e. $\sum_{i=0}^n a_i x_2^i \hat{a}_i$, where $n > 2$.

It should be pointed out that the assumption of a purely shear straining velocity field in the bottom and surface boundary layers, which allows the use of Eq. (6), is not valid for all instants. There are compressible flow areas in the shoaling region, where the flow depends on the superposition of the incoming waves, surface breaking and reflected wave. In the Boussinesq-type models for surface waves, the flow is represented through a decomposition of the velocity into a potential and a rotational

part (Briganti, Musumeci, Bellotti, Brocchini, & Foti, 2004). The direct ensemble-averaged measured velocity solutions confirm that both eddy viscosity formulae Eq. (6) and Eq. (7) can result in peaks and negative values. This is apparently due to the velocity corresponding to a potential part where its gradient components do not represent the shear straining. Thus, an irrotational flow may be removed from the measured velocity by linear decomposition of the mean velocity and its derivatives. The velocity corresponding to a rotational part may be obtained by subtracting the velocity just outside the bottom boundary layer from the local velocity:

$$\overline{\langle U \rangle}_t = \overline{\langle U \rangle} - \overline{\langle U \rangle}_b . \quad (20)$$

Furthermore, mean velocity gradient components should be modified by the functions that depend on the distance above the bottom:

$$\left(\frac{\partial \langle U_1 \rangle}{\partial x_1} \right)_t = \frac{\partial \langle U_1 \rangle}{\partial x_1} - A(x_2) , \quad (21)$$

$$\left(\frac{\partial \langle U_2 \rangle}{\partial x_2} \right)_t = \frac{\partial \langle U_2 \rangle}{\partial x_2} - B(x_2) , \quad (22)$$

$$\left(\frac{\partial \langle U_1 \rangle}{\partial x_2} \right)_t = \frac{\partial \langle U_1 \rangle}{\partial x_2} - C(x_2) , \quad (23)$$

$$\left(\frac{\partial \langle U_2 \rangle}{\partial x_1} \right)_t = \frac{\partial \langle U_2 \rangle}{\partial x_1} - D(x_2) , \quad (24)$$

Table 5. Change of functions $A(x_2)$, $B(x_2)$, $C(x_2)$, $D(x_2)$ over depth

Function (s^{-1})	Height on the sloping bottom (m)				
	0.067	0.052	0.040	0.028	0.006
$A(x_2)$	0	1	1	4	4
$B(x_2)$	13	14	15	15	33
$C(x_2) = D(x_2)$	-45	-45	-44	-45	-135

The compressibility of the fluid considered in Eq. (7) is based on the experimental observations, showing that the wave motion in the surf zone is accompanied by a substantial amount of air mixed into the water due to surface breaking. A change in the water density over time implies that the fluid in breaking waves could compress and expand, which is associated with compression, shear and extension stresses. Only the compression stress is not included in an incompressible flow. Consequently, for a two-dimensional flow in a breaking wave, which corresponds to the experimental results, the non-zero divergence of the mean velocity is found, i.e.,

$$\frac{\partial \langle U_1 \rangle}{\partial x_1} + \frac{\partial \langle U_2 \rangle}{\partial x_2} \neq 0, \quad (25)$$

a vertical velocity gradient component is negligible, i.e.,

$$\frac{\partial \langle U_3 \rangle}{\partial x_3} \approx 0, \quad (26)$$

and can be therefore ignored in Eq. (7).

2.4.2 Modified wave characteristics

The following figures show modified wave characteristics after the irrotational flow has been removed on five different heights at one profile: Fig. 10 on 0.067 m; Fig. 11 on 0.052 m; Fig. 12 on 0.040 m; Fig. 13 on 0.028 m, and Fig. 14 on 0.006 m on the sloping bottom.

Section a) in the figures shows $\langle U_1 \rangle_t$ as modified horizontal velocity (shown by the continuous curve) and $\langle U_2 \rangle_t$ as modified vertical velocity (shown by the dashed curve), section b) shows $\langle u_1 \rangle$ as horizontal velocity fluctuation (shown by the continuous curve) and $\langle u_2 \rangle$ as vertical velocity fluctuation (shown by the dashed curve), section c) shows $\left(\frac{\partial \langle U_1 \rangle}{\partial x_1}\right)_t$ as modified horizontal velocity gradients in along-channel direction (shown by the continuous curve) and $\left(\frac{\partial \langle U_1 \rangle}{\partial x_2}\right)_t$ as modified horizontal velocity gradient in vertical direction (shown by the dashed curve) and section d) shows $\left(\frac{\partial \langle U_2 \rangle}{\partial x_1}\right)_t$ as modified vertical velocity gradient along-channel direction (shown by the continuous curve), and $\left(\frac{\partial \langle U_2 \rangle}{\partial x_2}\right)_t$ as modified vertical velocity gradient vertical direction (shown by the dashed curve).

After modifying the velocities, the lowest horizontal velocity $\langle U_1 \rangle_t$ values are now under the surface roller while there is no distinct local maximum throughout the wave period. $\langle U_1 \rangle_t$ value amplitude is between 0.192 m s^{-1} on the surface to 0.007 m s^{-1} near the bottom. This is almost four times smaller than the value directly from the measurements.

The vertical velocity $\langle U_2 \rangle_t$ values and behaviour have stayed similar to the measured values. $\langle U_2 \rangle_t$ values increase from near-zero from the bottom boundary layer to the amplitude of 0.318 m s^{-1} surface boundary layer.

Most drastical change occurred in the $\left(\frac{\partial \langle U_1 \rangle}{\partial x_2}\right)_t$ velocity gradient after the modification, the amplitude of minimum and maximum values is 30 times higher than before on the surface (dashed curve in Fig. 10c), and 100 times higher on the bottom (dashed curve in Fig. 14c). While the $\left(\frac{\partial \langle U_2 \rangle}{\partial x_2}\right)_t$ velocity gradient after the modification changed the amplitude of minimum and maximum values two times higher than before on the bottom (dashed curve in Fig. 14d); however, on the surface, the change was not that significant (dashed curve in Fig. 10d). Velocity gradients $\left(\frac{\partial \langle U_1 \rangle}{\partial x_1}\right)_t$ and $\left(\frac{\partial \langle U_2 \rangle}{\partial x_1}\right)_t$ stayed close to similar to the measured values (Fig. 10-14c continuous curve and Fig. 10-14d continuous curve, respectively).

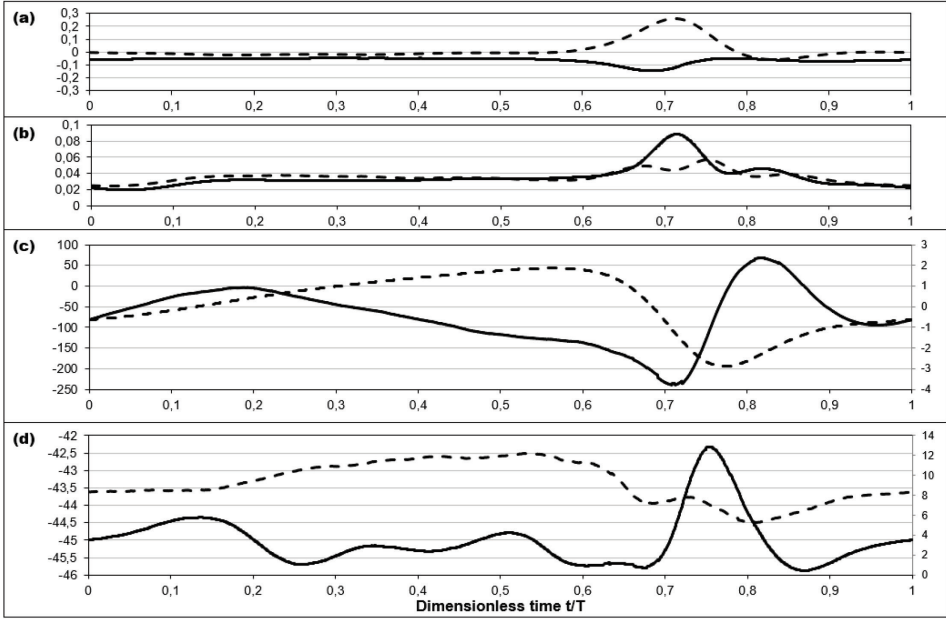


Figure 10. Wave characteristics 0.067 m above the sloping bottom after irrotational flow removal: a) modified horizontal velocity $\langle U_1 \rangle_t$ ($m s^{-1}$) (continuous curve) and modified vertical velocity $\langle U_2 \rangle_t$ ($m s^{-1}$) (dashed curve); b) horizontal velocity fluctuations $\langle u_1 \rangle$ ($m s^{-1}$) (continuous curve) and vertical velocity fluctuation $\langle u_2 \rangle$ ($m s^{-1}$) (dashed curve); c) modified horizontal velocity gradient along the channel direction $\left(\frac{\partial \langle U_1 \rangle}{\partial x_1}\right)_t$ (s^{-1}) (continuous curve) and modified horizontal velocity gradient in the channel vertical direction $\left(\frac{\partial \langle U_1 \rangle}{\partial x_2}\right)_t$ (s^{-1}) (dashed curve); d) modified vertical velocity gradient along the channel direction $\left(\frac{\partial \langle U_2 \rangle}{\partial x_1}\right)_t$ (s^{-1}) (continuous curve) and modified vertical velocity gradient along the channel vertical direction $\left(\frac{\partial \langle U_2 \rangle}{\partial x_2}\right)_t$ (s^{-1}) (dashed curve).

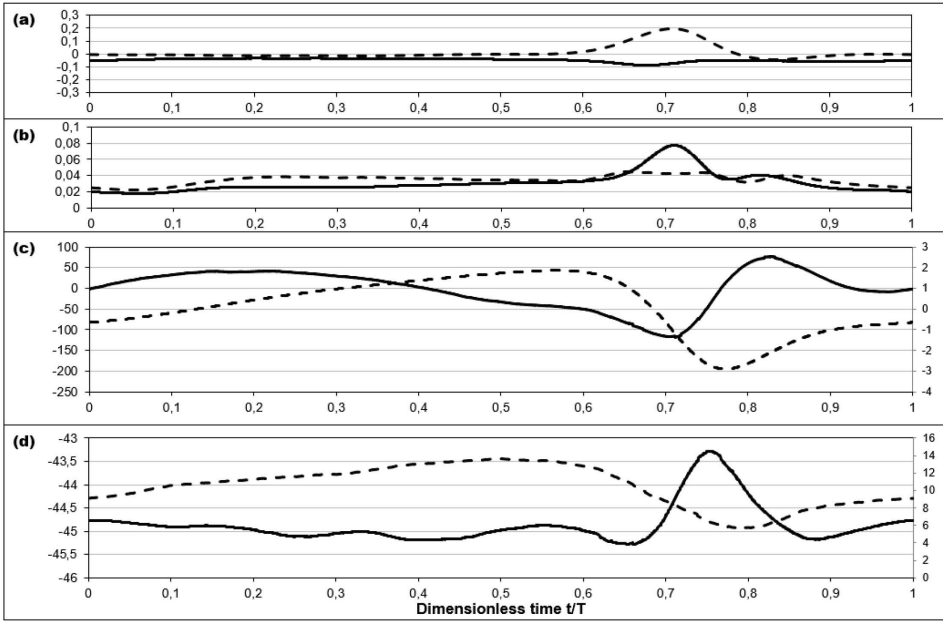


Figure 11. Wave characteristics 0.052 m above the sloping bottom after irrotational flow removal: a) modified velocities $\langle U_1 \rangle_t$ and $\langle U_2 \rangle_t$ ($m s^{-1}$); b) fluctuations $\langle u_1 \rangle$ and $\langle u_2 \rangle$ ($m s^{-1}$); c) modified gradients $\left(\frac{\partial \langle U_1 \rangle}{\partial x_1}\right)_t$ and $\left(\frac{\partial \langle U_1 \rangle}{\partial x_2}\right)_t$ (s^{-1}); d) modified gradients $\left(\frac{\partial \langle U_2 \rangle}{\partial x_1}\right)_t$ and $\left(\frac{\partial \langle U_2 \rangle}{\partial x_2}\right)_t$ (s^{-1}) (explanation to axis titles under Fig. 10).

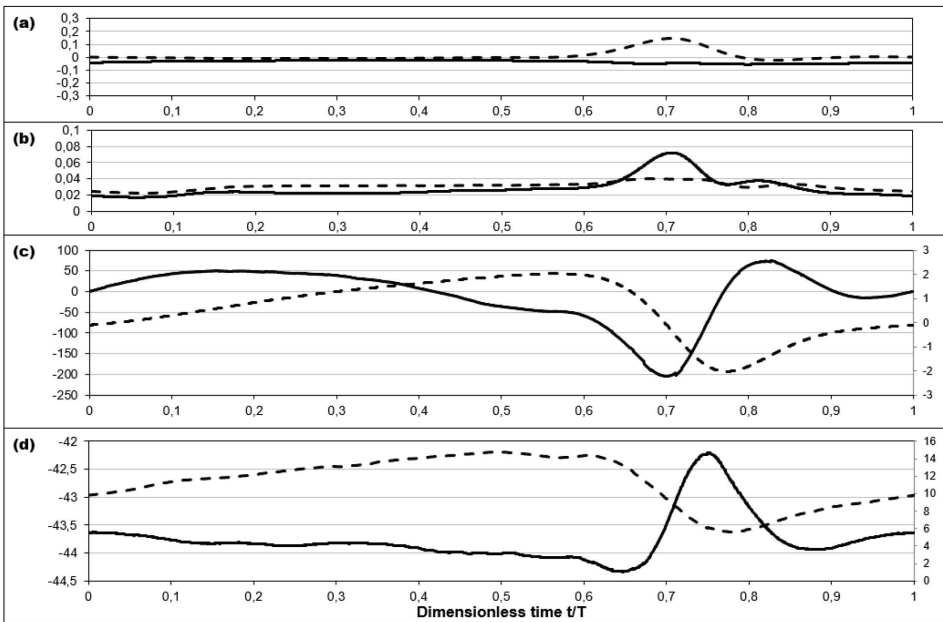


Figure 12. Wave characteristics 0.040 m above the sloping bottom after irrotational flow removal: a) modified velocities $\langle U_1 \rangle_t$ and $\langle U_2 \rangle_t$ ($m s^{-1}$); b) fluctuations $\langle u_1 \rangle$ and $\langle u_2 \rangle$ ($m s^{-1}$); c) modified gradients $\left(\frac{\partial \langle U_1 \rangle}{\partial x_1}\right)_t$ and $\left(\frac{\partial \langle U_1 \rangle}{\partial x_2}\right)_t$ (s^{-1}); d) modified gradients $\left(\frac{\partial \langle U_2 \rangle}{\partial x_1}\right)_t$ and $\left(\frac{\partial \langle U_2 \rangle}{\partial x_2}\right)_t$ (s^{-1}) (explanation to axis titles under Fig. 10).

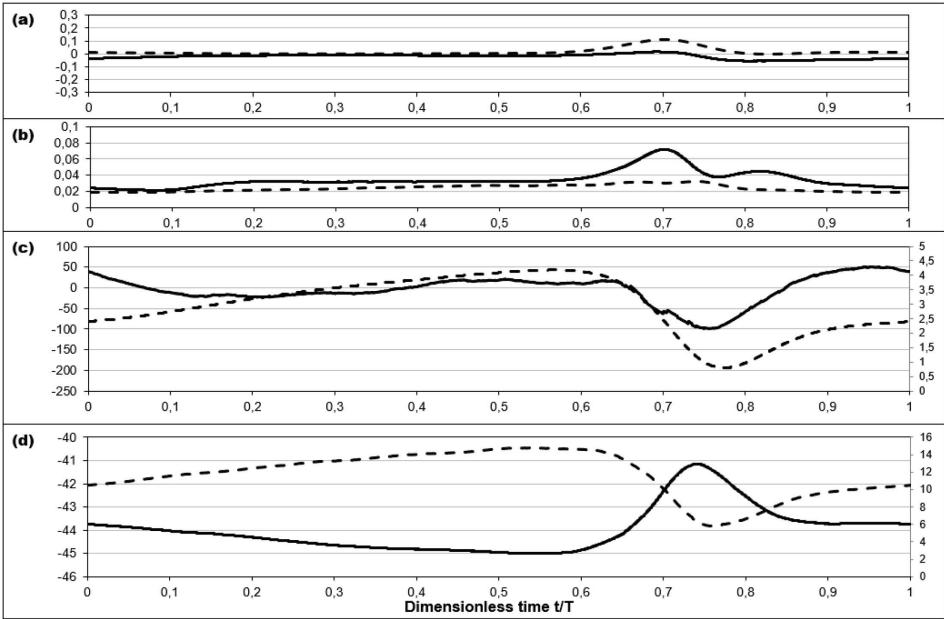


Figure 13. Wave characteristics 0.028 m above the sloping bottom after irrotational flow removal: a) modified velocities $\langle U_1 \rangle_t$ and $\langle U_2 \rangle_t$ ($m s^{-1}$); b) fluctuations $\langle u_1 \rangle$ and $\langle u_2 \rangle$ ($m s^{-1}$); c) modified gradients $\left(\frac{\partial \langle U_1 \rangle}{\partial x_1}\right)_t$ and $\left(\frac{\partial \langle U_1 \rangle}{\partial x_2}\right)_t$ (s^{-1}); d) modified gradients $\left(\frac{\partial \langle U_2 \rangle}{\partial x_1}\right)_t$ and $\left(\frac{\partial \langle U_2 \rangle}{\partial x_2}\right)_t$ (s^{-1}) (explanation to axis titles under Fig. 10).

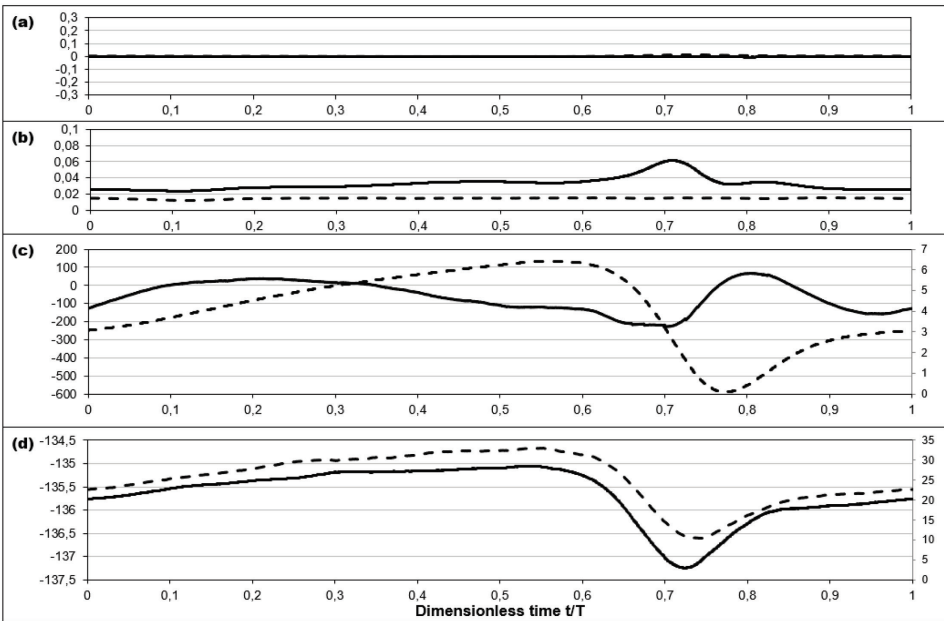


Figure 14. Wave characteristics 0.006 m above the sloping bottom after irrotational flow removal: a) modified velocities $\langle U_1 \rangle_t$ and $\langle U_2 \rangle_t$ ($m s^{-1}$); b) fluctuations $\langle u_1 \rangle$ and $\langle u_2 \rangle$ ($m s^{-1}$); c) modified gradients $\left(\frac{\partial \langle U_1 \rangle}{\partial x_1}\right)_t$ and $\left(\frac{\partial \langle U_1 \rangle}{\partial x_2}\right)_t$ (s^{-1}); d) modified gradients $\left(\frac{\partial \langle U_2 \rangle}{\partial x_1}\right)_t$ and $\left(\frac{\partial \langle U_2 \rangle}{\partial x_2}\right)_t$ (s^{-1}) (explanation to axis titles under Fig. 10).

2.4.3 Shear velocity

An empirical Shields diagram (Shields, 1936) that demonstrates the critical shear stress for the start of sediment uplift as a relation between the grain Reynolds number based on the shear velocity and the nondimensional shear stress, is the most commonly used method for sediment transport. An alternative method is to use the movability number, which is defined as the ratio of the shear velocity to the particle's settling velocity (Simões, 2014). That requires accurate defining of the shear velocity on the bottom boundary layer.

Calculated shear velocity according to Eq. (12) (see Fig. 15) was calculated at the height of 0.006 m on the sloping bottom, which was the closest measuring height to the bottom. Also, Fig. 15 shows local horizontal and vertical velocities. Highest values of shear velocity are directly under the wave crest, i.e., dimensionless wave period 0.78, and lowest values are directly under the wave trough, i.e., dimensionless wave period 0.5 – 0.6. Shear velocity demonstrates good correlation with local horizontal velocity taking use of linear assumption; however, the shear velocity values are times lower due to dynamic viscosity in Eq. (12).

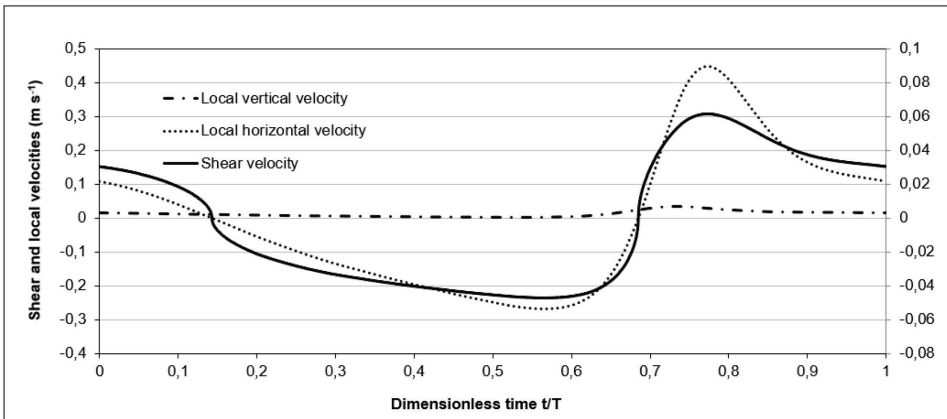


Figure 15. Calculated shear velocity U_* ($m s^{-1}$) and local horizontal velocity $\langle U_1 \rangle_b$ ($m s^{-1}$) and vertical velocity $\langle U_2 \rangle_b$ ($m s^{-1}$) of 0.006 m above the sloping bottom.

Based on the ensemble-averaged shear velocities in all 29 profiles, Fig. 16 presents the variation of shear velocity on the bottom of the surf zone model at different dimensionless time moments: a) 0.3, b) 0.5, c) 0.7, d) 0.8 and e) 0.9. Also, the surface elevations are shown in the plots of Fig. 16. It can be seen that at the given time moment, the shear velocity is different in different profiles and the behaviour over the wave cycle varies in different locations in the surf zone.

Fig. 16 also shows that there is a good correlation between the surface elevation and the shear velocity. The approaching wave crest increases the values of the bottom shear velocity. It can also be seen that the value of the shear velocity drops rapidly to the wave trough levels after the passing of the wave crest. It stays nearly constant under the wave trough. The figures demonstrate that the direction of the shear velocity mainly follows the direction of the flow outside the boundary layer. An exception to the trend is the area directly in front of the wave crest. In this area, the jet generated by the overturning of the wave crest hits the water and reaches the bottom. It can be seen

that despite the overall direction of the flow, the shear velocity is directed mainly towards the coastline. Further profiles are shown in author's **Publication I**.

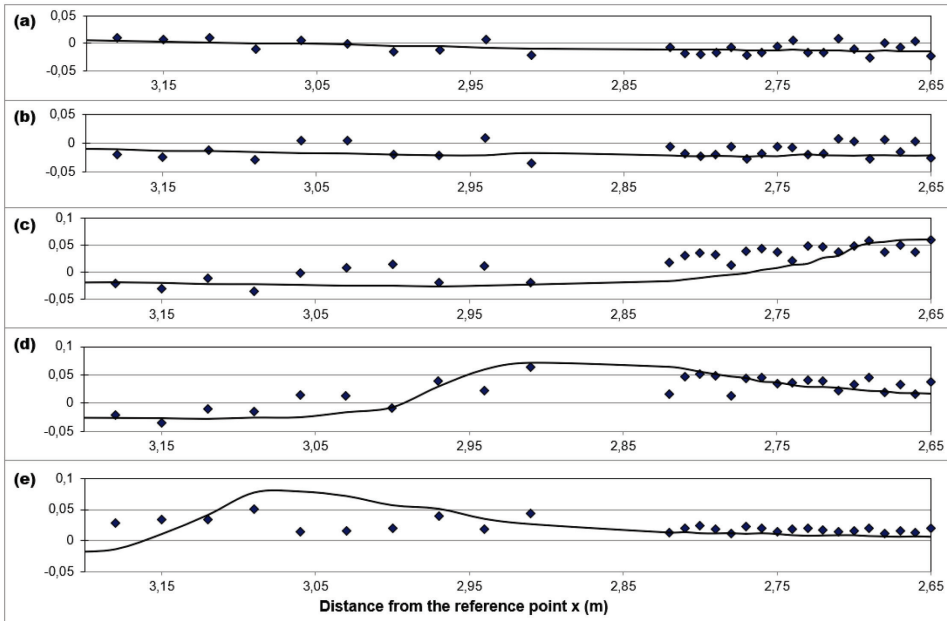


Figure 16. Correlation between the shear velocity U_* ($m s^{-1}$) (dots) and the mean free-surface displacement along the sloping bottom (continuous curve) on different dimensionless wave periods.

2.4.4 Turbulent kinetic energy

Measured turbulent kinetic energy according to Eq. (9) (see Fig. 17) was calculated at five different heights at one profile: a) 0.067 m; b) 0.052 m; c) 0.040 m; d) 0.028 m, and e) 0.006 m on the sloping bottom. Turbulent kinetic energy demonstrates two local maximums: at instants when the surface roller is passing measurement profile 17, i.e., dimensionless wave period 0.65 – 0.75, and directly after the wave crest, i.e., dimensionless wave period 0.80 – 0.85. After breaking of a wave, there is a local minimum in the turbulent kinetic energy value occurring during a dimensionless wave period 0.00 – 0.10, which then converges to more or less constant value during a dimensionless wave period 0.10 – 0.60. It can be seen (Fig. 18 and Fig. 28) that the turbulent kinetic energy varies almost linearly with the increasing height from the bed.

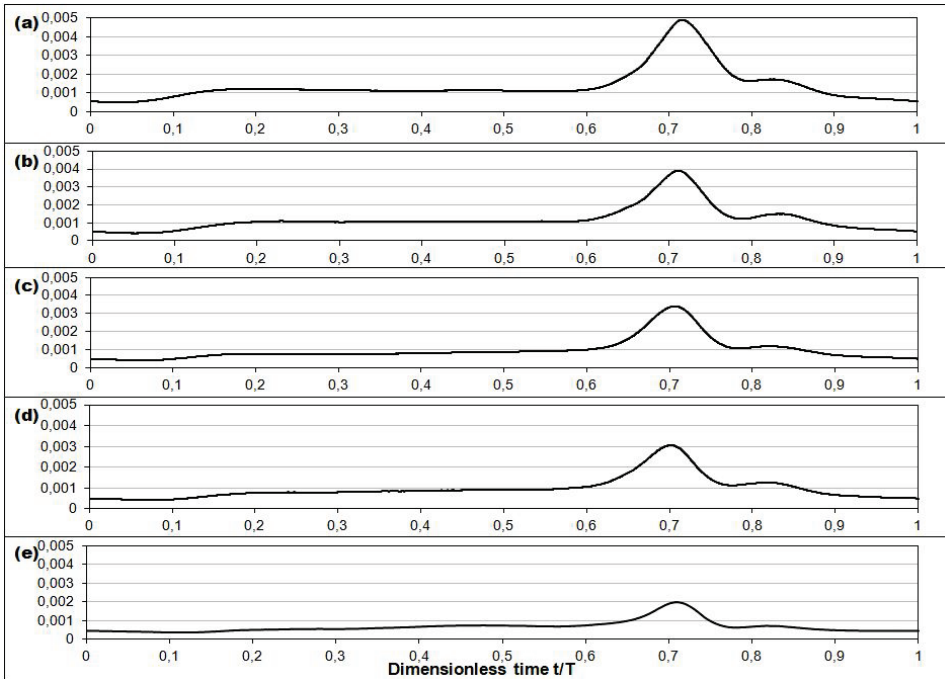


Figure 17. Measured turbulent kinetic energy k_T ($m^2 s^{-2}$) on separate plots at different heights above the sloping bottom: a) 0.067 m; b) 0.052 m; c) 0.040 m; d) 0.028 m and e) 0.006 m.

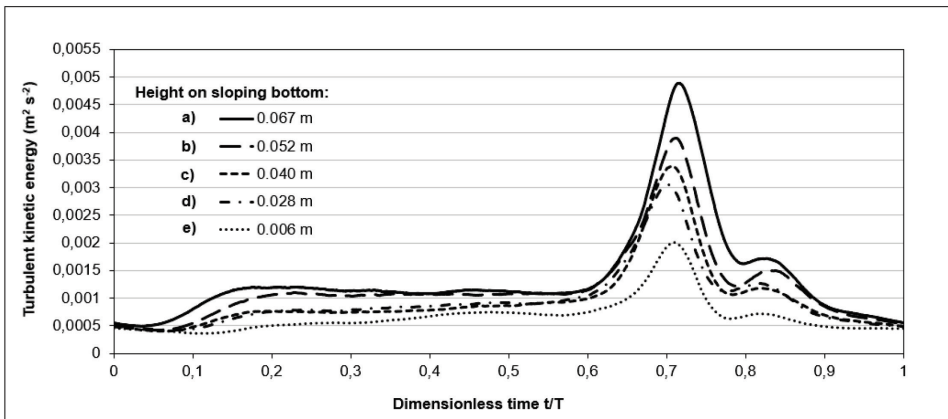


Figure 18. Measured turbulent kinetic energy k_T ($m^2 s^{-2}$) on the same plot at different heights above the sloping bottom: a) 0.067 m; b) 0.052 m; c) 0.040 m; d) 0.028 m and e) 0.006 m.

Turbulent production from Eq. (11) follows turbulent kinetic energy movements (see Fig. 19), and stays positive throughout the period.

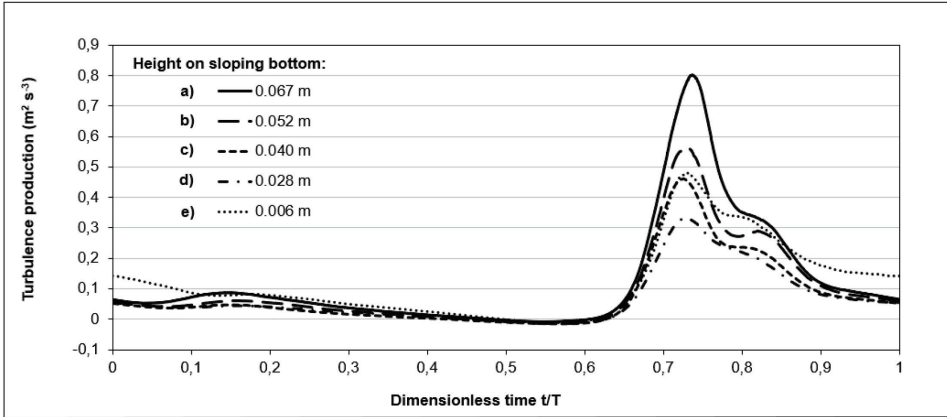


Figure 19. Measured turbulent production \mathcal{P} ($m^2 s^{-3}$) on the same plot at different heights above the sloping bottom: a) 0.067 m; b) 0.052 m; c) 0.040 m; d) 0.028 m and e) 0.006 m.

2.4.5 Eddy viscosity

The eddy viscosity was determined at a height of 0.067 m above the bottom in Fig. 20, at a height of 0.052 m above the bottom in Fig. 21, at a height of 0.040 m above the bottom in Fig. 22, at a height of 0.028 m above the bottom in Fig. 23, and at a height of 0.006 m above the bottom in Fig. 24. Using the modified velocity gradient components, the solution resulting from the non-diagonal elements from the Reynolds stress tensor in Eq. (6) is shown by a dash-dot curve in Figs. 20-24. Eddy viscosity based on the first and second diagonal elements from the Reynolds stress tensor in Eq. (7) is shown as curves with shorter and longer dashed lines, respectively in Figs. 20-24. Also, Figs. 20-24 show averaged eddy viscosity values derived from the results of Eq. (6) and Eq. (7) (shown as a continuous curve).

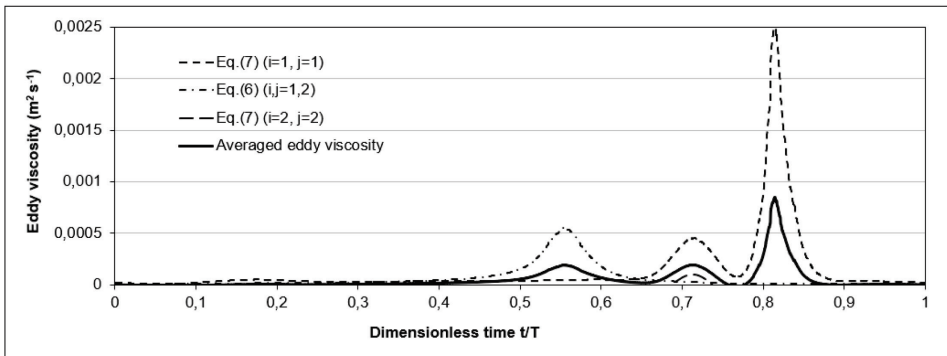


Figure 20. Eddy viscosity ν_T ($m^2 s^{-1}$) based on theoretical equations with the surface direction index i and the flow direction index j 0.067 m above the sloping bottom.

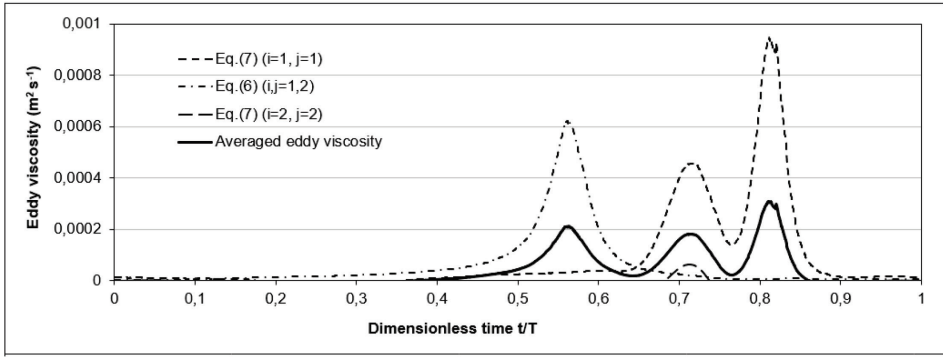


Figure 21. Eddy viscosity ν_T ($m^2 s^{-1}$) based on theoretical equations with the surface direction index i and the flow direction index j 0.052 m above the sloping bottom.

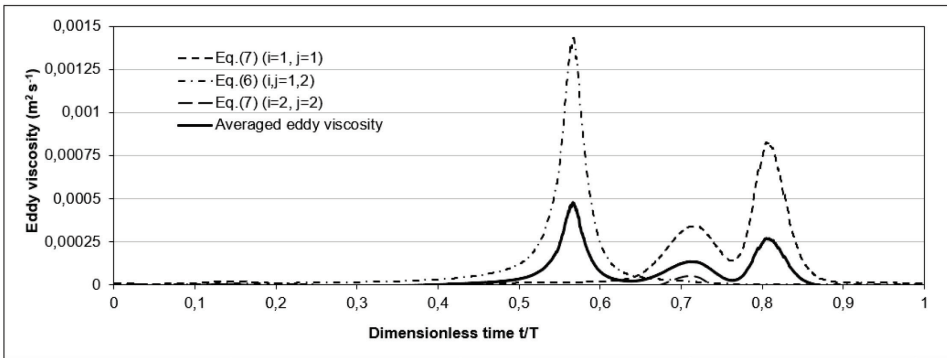


Figure 22. Eddy viscosity ν_T ($m^2 s^{-1}$) based on theoretical equations with the surface direction index i and the flow direction index j 0.040 m above the sloping bottom.

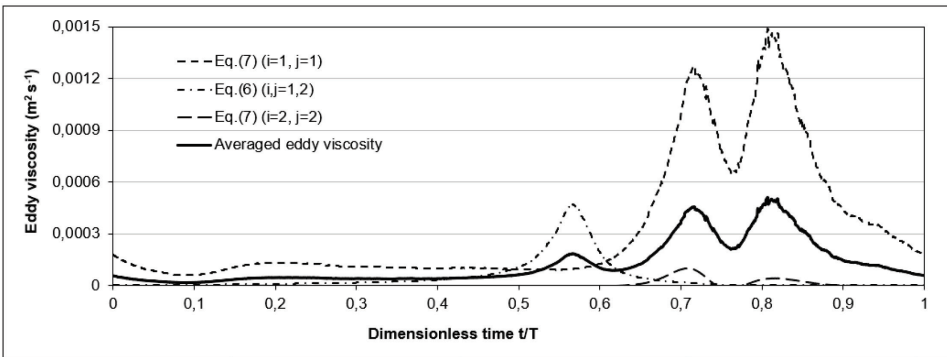


Figure 23. Eddy viscosity ν_T ($m^2 s^{-1}$) based on theoretical equations with the surface direction index ii and the flow direction index ii 0.028 m above the sloping bottom.

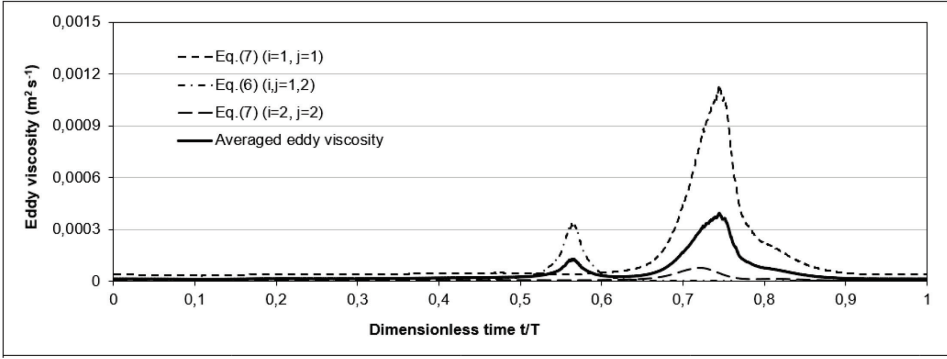


Figure 24. Eddy viscosity ν_T ($m^2 s^{-1}$) based on theoretical equations with the surface direction index ii and the flow direction index jj 0.006 m above the sloping bottom.

The eddy viscosity (see Fig. 25) demonstrates three maximums on four higher measurement points, i.e., 0.028 m, 0.040 m, 0.052 m and 0.067 m: at instants when the surface roller hits the water surface, i.e., dimensionless wave period interval 0.50 – 0.60, when the surface roller is passing the measuring point, i.e., dimensionless wave period interval 0.65 – 0.75, and after the wave crest is passing the measuring point, i.e., dimensionless wave period interval 0.80 – 0.85. The last two maximums out of the three correspond in time with the turbulent kinetic energy maximums.

Furthermore, the eddy viscosity based on the non-diagonal elements from the Reynolds stress tensor with shear deformation in Eq. (6) is responsive of the first maximum, while eddy viscosity based on the first and second diagonal elements from the Reynolds stress tensor with expansion and compression deformation in Eq. (7) is responsive of the last two maximums.

The last eddy viscosity (see Fig. 25e) shows only the first two maximums, leaving out the one from the wave crest passing.

After breaking of a wave, the eddy viscosity value is more or less constant during a dimensionless wave period interval 0.90 – 0.50. However, on the lowest measurement point, i.e., 0.006 m, there are only two first maximums compared to previous higher measurement heights. In other words, the turbulence develops in the layers close to the bottom when the roller generated turbulence develops downwards and the eddy viscosity maximum appears when the surface roller has passed and then disappears in the layer closest to the bottom, i.e., 0.006 m.

It can be observed that both maximums of the measured turbulent kinetic energy from Fig. 17 align with the second and third maximums of averaged eddy viscosity from Fig. 25. As can be seen, the largest maximum of eddy viscosity does not appear in correspondence with the largest turbulent kinetic energy maximum, rather it is related to the secondary maximum.

However, considering the alternative option suggested by Luracelli (Luracelli, Lugni, Falchi, Felli, & Brocchini, 2018), by changing the cross coordinate system to the orthogonal coordinate system, which follows the velocity field, results in two maximums only. This is due to the eddy viscosity relation to the turbulent kinetic energy, i.e. $\nu_T = C_k (c\sqrt{k_T})b$, where $C_k = 0.4$ is von Karman constant, $c\sqrt{k_T}$ is estimation of the turbulent velocity scale and b is the single-phase turbulent layer thickness, estimating the turbulence length scale.

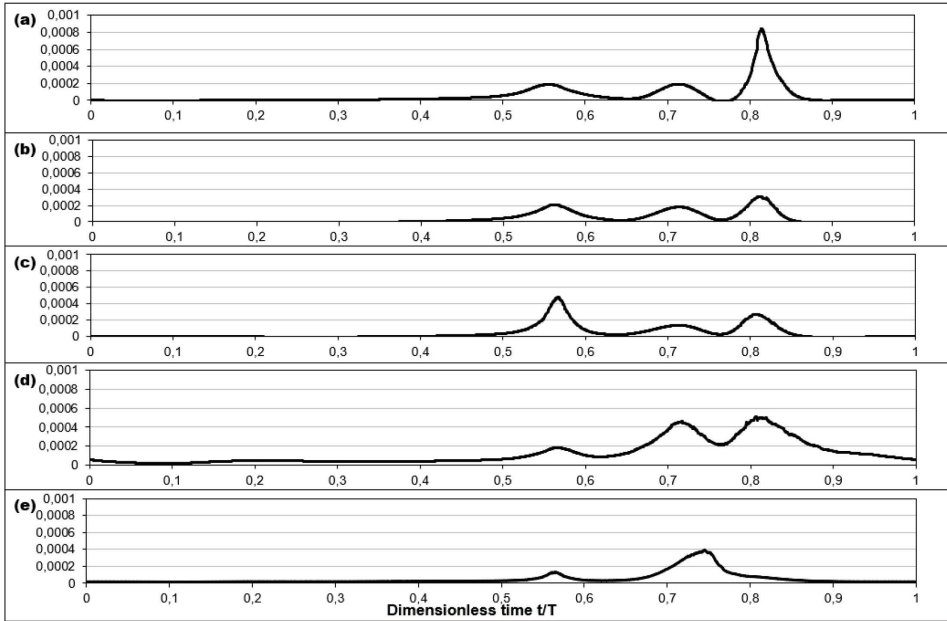


Figure 25. Averaged eddy viscosity v_T ($m^2 s^{-1}$) values on separate plots based on theoretical equations with the surface direction index i and the flow direction index j at different heights above the sloping bottom: a) 0.067 m; b) 0.052 m; c) 0.040 m; d) 0.028 m and e) 0.006 m.

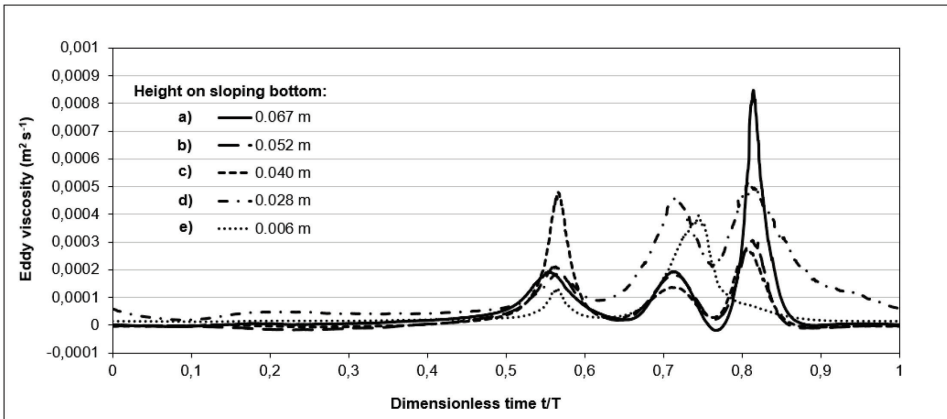


Figure 26. Averaged eddy viscosity v_T ($m^2 s^{-1}$) values on a singular plot based on theoretical equations with the surface direction index i and the flow direction index j at different heights above the sloping bottom: a) 0.067 m; b) 0.052 m; c) 0.040 m; d) 0.028 m and e) 0.006 m.

Furthermore, eddy viscosity values demonstrate obvious maximums in Fig. 26, i.e., highest values at wave period dimensionless instants 0.568753, 0.711681 and 0.814687, the corresponding eddy viscosity profiles of whose are shown in Fig. 27; corresponding turbulent kinetic energy profiles at the same instants are shown in Fig. 28. The highest eddy viscosity value, i.e., $\sim 0.00085 m^2 s^{-1}$, is on the highest measurement point, i.e., 0.067 m, appearing directly after the wave crest passing the measuring point (shown by the continuous curve on Fig. 27). Next highest values of the

eddy viscosity, i.e., $\sim 0.00048 \text{ m}^2 \text{ s}^{-1}$ and $\sim 0.00042 \text{ m}^2 \text{ s}^{-1}$ respectively, are both on the second lowest measurement point, i.e., 0.028 m, when the wave crest has passed the measuring point and when the surface roller is passing (shown by longer dashed-dot curve on Fig. 27). The same highest value range of the eddy viscosity, i.e., $\sim 0.00046 \text{ m}^2 \text{ s}^{-1}$, is on the middle measurement point, i.e., 0.040 m, at the instants when the surface roller hits the water surface (shown by the shorter dashed curve on Fig. 27). In other words, the eddy viscosity generated in the surface roller hitting the surface affects mostly middle depths, while the surface roller passing affects mostly bottom region and the wave crest passing affects both the surface and bottom region. For comparison, Fig. 27 presents the selected dimensionless wave period instant 0.245441 to show eddy viscosity values outside of the maximum values, where the eddy viscosity values are more or less constant over the water depth.

Fig. 27 shows that eddy viscosity profiles over the water depth are more complex than commonly used eddy viscosity profiles like, for instance, work by Briganti, Musumeci, Bellotti, Brocchini, & Foti (2004) where the eddy viscosity is taken as uniform over the water depth and as uniform over the top half of the water depth while linear decrease to zero occurs over the lower half.

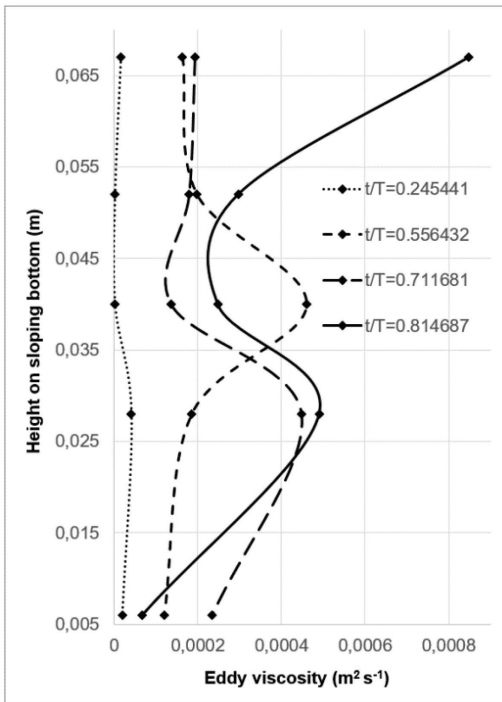


Figure 27. Averaged eddy viscosity ν_T ($\text{m}^2 \text{ s}^{-1}$) values over the water depth at the maximums shown in Fig. 25 and Fig. 26 in the dimensionless wave period: a) 0.245441; b) 0.568753; c) 0.711681 and d) 0.814687.

The eddy viscosity values estimated with formulae Eq. (6) and Eq. (7) represent certain relationships between the velocity fluctuations correlation coefficients, turbulence kinetic energy and mean velocity gradient components. It was found by the author in **Publication II** that the ensemble-averaged measured velocity predicted eddy viscosity is associated with peaks and negative values, which are absent in the broadly

accepted empirical predictions. Mentioned peaks and negative values are related to the velocity corresponding to a potential part of the flow where its gradient components do not represent the shear straining and manifest themselves when the shear stress and the velocity gradient change signs, i.e., flow reversal. This phenomenon has been reported by Perrier, Villaret, Davies, & Hansen (1995), Davies & Villaret (1999) and Malarkey & Davies (2004). We followed the methodology proposed by Briganti, Musumeci, Bellotti, Brocchini, & Foti (2004), where the flow is represented through a decomposition of the velocity into a potential and a rotational part. A possible alternative to solve the eddy viscosity problem was suggested by Shih, Zhu, & Lumley (1996), which was based on the relation between the Reynolds stress tensor and the strain rate of the mean flow through the nonlinear Reynolds stress model.

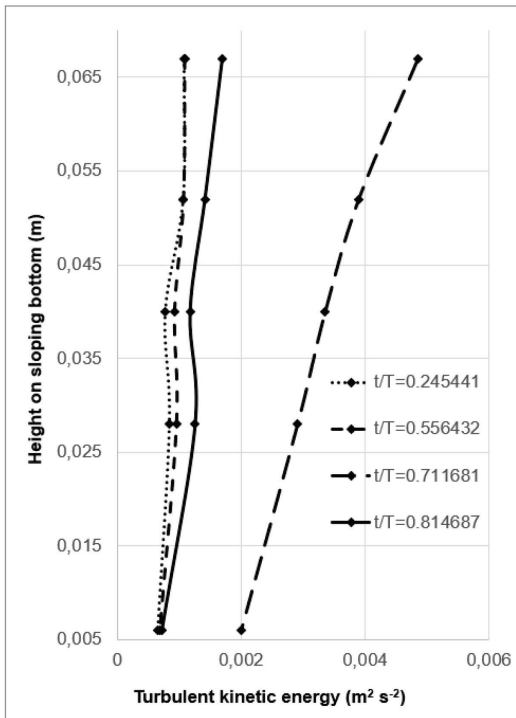


Figure 28. Measured turbulent kinetic energy k_T ($m^2 s^{-2}$) values over the water depth at the averaged eddy viscosity maximums shown in Fig. 27 in the dimensionless wave period: a) 0.245441; b) 0.568753; c) 0.711681 and d) 0.814687.

In the surf zone, the surface wave changes due to the velocity shear near the bottom and free surface non-linear deformation, the turbulence is generated from two sources: bottom boundary layer and surface boundary layer. Also, the present study takes into account that eddy viscosity is not related to the tube flow oscillation approximation, where it is sufficient to use the relationship between the correlation coefficient of cross-flow directional fluctuations and the vertical component of the along channel velocity gradient. Furthermore, a substantial amount of air that is captured within the wave motion due to breaking results in the non-zero divergence of the mean velocity. This indicates that the air mixing in the water of the plunging breaker corresponds to a weakly compressible fluid.

3 Modelling and simulation

3.1 Theoretical background

Turbulence model's classification is outlined in Fig. 9. While Chapter 2 concentrated on RANS models, this chapter concentrates on turbulence models such as LES and DNS used in Computational Fluid Dynamics (CFD).

LES is a mathematical model in CFD for simulating turbulence. It was originally developed by Smagorinsky (1963) to simulate atmospheric air currents, and then modified by Deardorff (1970). By numerically solving the Navier–Stokes equations, the simulation of turbulent flows needs a very wide range of length scales and time. This can be reached with DNS, which is computationally expensive.

The primary goal behind LES is to decrease the computational cost by ignoring the smallest length scales. Through low-pass filtering smaller length scales of the Navier–Stokes equations, computational costs are saved. Removed small-scale information is not irrelevant, but its consequences on the flow field, such as near-wall flows, must be modelled (Piomelli & Balaras, 2002).

One of the main challenges in coastal wave modelling is to derive a model capable of describing simultaneously the dispersive effects and the dissipative effects in waves, while predicting accurately the breaking point. The dispersive effects dominate before wave breaking, and the dissipation dominates after wave breaking. The classical dispersive equations (Green & Naghdi, 1976) lack dissipative terms while the nonlinear shallow-water equations (Barre de Saint Venant, 1871) are non-dispersive. However, the weak nonlinearity assumption (Boussinesq, 1872) in dispersive equations reduces the validity of these equations, which has been improved by Madsen, Murray & Sorensen (1991) and also by Nwogu (1993).

Existing Large Eddy Simulations give options for choosing a turbulence model. For instance, MIKE21 HD (product of MIKE Powered by DHI foundation) can work with uniform eddy viscosity and Smagorinsky model. At the same time, Delft3D (developed by Deltares) besides uniform eddy viscosity, supports the $k - L$ transport model for the turbulent kinetic energy and mixing length, algebraic model and $k - \varepsilon$ transport models for the turbulent kinetic energy and the turbulent kinetic energy dissipation rate. Fluent (developed by ANSYS) could adapt Spalart Allmaras 1-equation model, standard, RNG, Realizable $k - \varepsilon$ models, Standard and SST $k - \omega$ models, and finally Reynolds Stress Model.

3.1.1 The equations of fluid motion

The main equations for a fluid flow are the Navier-Stokes equations, which are derived from fundamental physical laws as conservation of fluid mass and momentum. In the case of turbulent flow, it is important to consider the energy equations to distinguish the viscous flow from the wave processes.

The momentum equation of motion relates acceleration to the net force at an elementary volume:

$$\rho \frac{DU_i}{Dt} = \rho g_i + \frac{\partial \tau_{ij}}{\partial x_j} . \quad (27)$$

A flowing fluid due to viscosity develops additional components of stress. The diagonal terms of the stress tensor become unequal and can be divided into compressive stress and shear stress:

$$\tau_{ij} = -p\delta_{ij} + \sigma_{ij}, \quad (28)$$

where σ_{ij} , is related to the velocity gradients $\frac{\partial U_i}{\partial x_j}$.

For a compressible fluid, difference to the rate of expansion is solved through the coefficient of bulk viscosity, $\kappa = \lambda + \frac{2}{3}\mu$, where λ and μ are scalars that depend on the local thermodynamic state (Kundu & Cohen, 2010). The assumption $\kappa = 0$ allows us to simplify the viscous stress tensor to:

$$\tau_{ij} = -\left(p + \frac{2}{3}\mu\nabla \cdot \vec{U}\right)\delta_{ij} + 2\mu e_{ij} \quad (29)$$

where the symmetric part of the velocity gradient is $e_{ij} = \frac{1}{2}\left(\frac{\partial U_i}{\partial x_j} + \frac{\partial U_j}{\partial x_i}\right)$.

For an incompressible fluid, the divergence of the velocity vector is zero and the viscous stress tensor is simplified to:

$$\tau_{ij} = -p\delta_{ij} + 2\mu e_{ij} \quad (30)$$

The general form of the Navier-Stokes equation of motion for a Newtonian fluid is obtained by substituting Eq. (29) into Eq. (27) to obtain:

$$\rho \frac{D U_i}{D t} = -\frac{\partial p}{\partial x_i} + \rho g_i + \frac{\partial}{\partial x_j} \left[2\mu e_{ij} - \frac{2}{3}\mu(\nabla \cdot \vec{U})\delta_{ij} \right] \quad (31)$$

In the case of an incompressible fluid, the density is considered constant and the mass-conservation equation is simplified to the continuity equation for velocity:

$$\nabla \cdot \vec{U} = 0 \quad (32)$$

and the Navier-Stokes momentum equation is reduced to:

$$\rho \frac{D \vec{U}}{D t} = -\nabla p + \rho \vec{g} + \mu \nabla^2 \vec{U} \quad (33)$$

The decomposition of the velocity into its mean and the fluctuation (Eq. (4)) results in the compressible RANS continuity equation:

$$\frac{\partial \langle \rho \rangle}{\partial t} + \frac{\partial \langle \rho U_i \rangle}{\partial x_i} = 0 \quad (34)$$

and the momentum equation:

$$\rho \frac{D \langle U_i \rangle}{D t} = -\frac{\partial \langle p \rangle}{\partial x_i} + \rho g_i + \frac{\partial}{\partial x_j} \left[2\mu \langle e_{ij} \rangle - \frac{2}{3}\mu(\nabla \cdot \langle \vec{U} \rangle)\delta_{ij} - \rho \langle u_i u_j \rangle \right], \quad (35)$$

where t is the time, x_i is the spatial geometrical scale in the Cartesian direction i ($i = 1,2,3$), $\langle U_i \rangle$ is the averaged mean velocity component in the direction i , $\langle p \rangle$ is the averaged pressure, ρ is the fluid density (constant in time and space), $\rho \langle u_i u_j \rangle$ is the Reynolds stress tensor of the mean flow, and g_i represents the gravity ($g_1 = g_2 = 0, g_3 = -g$) (Richard, Duran, & Fabreges, 2019).

Reynolds stress tensor:

$$\rho \langle u_i u_j \rangle = -\frac{2}{3}(\rho k_T + \mu_T \nabla \cdot \langle \vec{U} \rangle)\delta_{ij} + 2\mu_T \langle e_{ij} \rangle \quad (36)$$

where $\mu_T = \nu_T \rho$, with ν_T is the eddy viscosity and rate of strain tensor of the mean flow already included.

Momentum equation for a compressible fluid is:

$$\rho \frac{D\langle U_i \rangle}{Dt} = -\frac{\partial}{\partial x_i} \left(\langle p \rangle + \frac{2}{3} k_T \right) + \rho g_i + \frac{\partial}{\partial x_j} \left[2\mu_{eff} \langle e_{ij} \rangle - \frac{2}{3} \mu_{eff} (\nabla \cdot \langle \vec{U} \rangle) \delta_{ij} \right], \quad (37)$$

where $\mu_{eff} = \mu + \mu_T$.

For an incompressible fluid, Eq. (34) and Eq. (37) look, respectively:

$$\frac{\partial \langle U_i \rangle}{\partial x_i} = 0 \quad (38)$$

$$\rho \frac{D\langle U_i \rangle}{Dt} = -\frac{\partial}{\partial x_i} \left(\langle p \rangle + \frac{2}{3} k_T \right) + \rho g_i + \frac{\partial}{\partial x_j} [2\mu_{eff} \langle e_{ij} \rangle]. \quad (39)$$

For modelling turbulent stresses in LES models, Boussinesq's assumption is applied. Available turbulence models were shown in the previous chapter.

3.2 Large Eddy Simulations

Detailed modelling of turbulence in breaking waves is a difficult task for several reasons; the velocity field during breaking is extremely chaotic and varies rapidly in space and time. Available models can handle most of the wave phenomena, such as shoaling, refraction, diffraction, but the prediction of the breaking event is challenging. Surface breaking is associated with the irreversible transformation of potential velocity field into motions of different types and scales, including the turbulence, vortices and air-water interactions in the surface roller.

In Large Eddy Simulations (LES), a turbulent closure needs to be provided that accounts for the effects of subgrid-scale motions on a large scale. With sufficiently powerful computers, it is possible to resolve the entire flow down to the molecular viscosity scales 1 cm. However, nowadays, due to computational power, the smallest achievable scale will be around 10 m. A turbulent closure provides an approximation to the 'eddy' terms on the right of the preceding equations. The simplest form of solution is to increase the viscosity and diffusivity until the viscous and diffusive scales are resolved.

Turbulent viscosity $\nu_T(x, t)$ can be disclosed empirically as the product of a shear velocity $U_*(x, t)$ and a length scale $L(x, t)$:

$$\nu_T = U_* L. \quad (40)$$

Considering the mixing length model, L for Eq. (40) is specified based on the geometry of the flow.

For saving computational costs, many calculation methods, as mentioned previously, use a uniform eddy viscosity value for the whole flow field, which is found either directly from the experiments, from available empirical information, or from trial and error calculations to match the observations to the problem considered. This would work only in large water bodies, so momentum equations could be neglected. For the calculation of hydrodynamic properties, the constant eddy viscosity model does not influence the determination of the flow behaviour. In some methods, an eddy viscosity is introduced merely to improve numerical stability (Argyropoulos & Markatos, 2015).

For example, a uniform eddy viscosity term can be chosen based on:

$$\nu_T = 0.02 \frac{\Delta x_1 \Delta x_2}{\Delta t}, \quad (41)$$

where $\Delta x_1 \Delta x_2$ is the grid spacing and Δt is the time steps.

Smagorinsky suggests (Galperin & Orszag, 1993) choosing a viscosity that depends on the resolved motions. Thus, the overall viscous operator has a nonlinear dependence on velocity. Smagorinsky chose his form of viscosity by considering Kolmogorov's ideas about the energy spectrum of 3D isotropic turbulence.

Kolmogorov (1941) supposed that that energy is injected into the flow at large scales (small k) and is 'cascaded' or transferred conservatively by nonlinear processes to smaller and smaller scales until it is dissipated near the viscous scale. By setting the energy flux through a particular wavenumber ϵ , to be a constant in k , there is only one combination of viscosity and energy flux that has the units of length, the Kolmogorov wavelength. It is $L_\epsilon(v) \propto \pi \epsilon^{-1/4} \nu^{3/4}$ (the π stems from conversion from wavenumber to wavelength). To ensure that this viscous scale is resolved in a numerical model, the grid-scale should be decreased until $L_\epsilon(v) > L$ (DNS). Alternatively, an eddy viscosity can be used and the corresponding Kolmogorov length can be made larger than the grid-scale, $L_\epsilon(A_h) \propto \pi \epsilon^{-1/4} A_h^{3/4}$ (for LES).

However, calculations are based on the fourth option iv), the Smagorinsky formula

$$\nu_T = C_S^2 \Delta x_1 \Delta x_2 \sqrt{\left(\frac{\partial \langle U_i \rangle}{\partial x_i}\right)^2 + \frac{1}{2} \left(\frac{\partial \langle U_i \rangle}{\partial x_j} + \frac{\partial \langle U_j \rangle}{\partial x_i}\right)^2 + \left(\frac{\partial \langle U_j \rangle}{\partial x_j}\right)^2}, \quad (42)$$

where C_S is a constant to be chosen in the interval of 0.25 to 1.0 (Canuto & Cheng, 1997).

Above, the length scale of the grid (=spacing) was denoted by L . However, in strongly anisotropic grids, L_x and L_y will be quite different in some locations. In that case, the Courant-Freidrichs-Lewy (CFL) condition (Courant, Friedrichs, & Lewy, 1967) suggests that the minimum of L_x and L_y be used. On the other hand, other viscosities which involve whether a particular wavelength is 'resolved' might be better suited to use the maximum of L_x and L_y . If false, the geometric mean of L_x^2 and L_y^2 is used for all viscosities, which is closer to the minimum and occurs naturally in the CFL constraint. Since the CFL condition on vertical velocity is often what sets the maximum timestep, this viscosity may substantially increase the allowable timestep without severely compromising the verity of the simulation.

Some stability issues (Leendertse, 1967) can arise when using the velocities from the previous time step and the eddy viscosity coefficient becomes large. So, the coefficient must fulfil the criterion

$$\frac{\nu_T \Delta t}{\Delta x_1 \Delta x_2} \leq \frac{1}{2}. \quad (43)$$

3.3 Smoothed Particle Hydrodynamics

In the coastal engineering studies, the meshless numerical modelling, such as Smoothed Particle Hydrodynamics (SPH) solvers, is becoming more useful (Monaghan, 1994). It has been demonstrated that the SPH models are suitable to reproduce free-surface phenomena such as a breaking wave (Dalrymple & Rogers, 2006), (Shao, 2006), (De Padova, Dalrymple, Mossa, & Petrillo, 2009), dam breaks (Gomez-Gesteira, Rogers, Dalrymple, & Crespo, 2010), (Lee, Violeau, Issa, & Ploix, 2010), whitewater formation (Morris, 2000), waves overtopping of harbour structures (Rogers, Dalrymple, & Stansby, 2010), and tsunamis generated landslide (Capone, Panizzo, & Monaghan,

2010). However, near-bottom velocity modelling is problematic in SPH, which may complicate solving practical coastal engineering problems.

The SPH belongs to the class of numerical models, which is based on an assumption that the fluid may be represented as a set of liquid mass particles, "smeared" in space. Each particle is represented as a point-mass of fluid, which carries mass, velocity and other properties, distributed in space, for example, by a Gaussian distribution. Thus, the motion of each particle is calculated through interactions with neighbouring particles using an analytical kernel function, which replaces the Dirac delta function for modelling of the fluid properties of an idealized point mass, as a function that is equal to zero everywhere except at the position of a point mass. In the present study, the turbulence in the wave breaking process is treated by using artificial viscosity and interpolating kernel (Violeau & Rogers, 2016) and an empirical equation of compressibility by Batchelor (1967).

In SPH, the fundamental is the integral interpolant of any function $A(\mathbf{r})$ by

$$A(\mathbf{r}) = \int A(\mathbf{r}')W(\mathbf{r} - \mathbf{r}', h)d\mathbf{r}', \quad (44)$$

where h is called the smoothing length while the integration is over the entire space and $W(\mathbf{r} - \mathbf{r}', h)$ is the interpolating kernel. This function leads to the following approximation of the function at an interpolation point:

$$A_s(\mathbf{r}) = \sum_j m_j \frac{A_j}{\rho_j} W(\mathbf{r}_i - \mathbf{r}_j, h), \quad (45)$$

where $W(\mathbf{r}_i - \mathbf{r}_j, h) = W_{ij}$ represents a weight function (see Fig. 29a), while mass and density are denoted by m_j and ρ_j . The summation is over all particles within the region determined by the kernel function. According to De Padova, Dalrymple, Mossa, & Petrillo (2009), in the limits where the kernel smoothing length h and the interparticle spacing Δr become small, the kernel is assumed to have compact support and to some extent, it should not matter which kernel is used as long as basic requirements are met. However, in practice, values are not small and the choice of the kernel can drastically change the computational results (Rosswog, 2015).

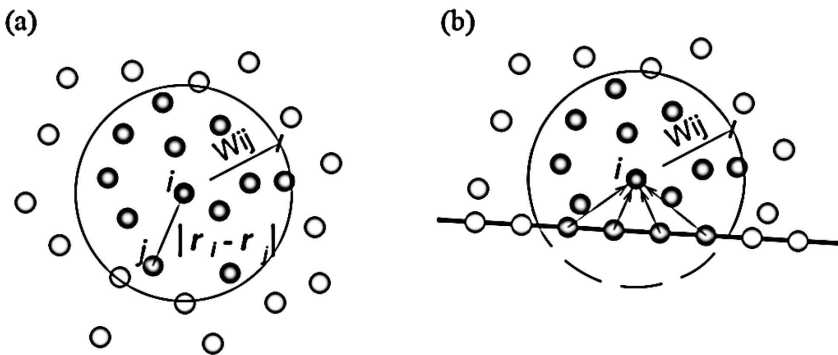


Figure 29. Particles representing fluid inside a smoothing area: a) liquid particles and b) liquid and bottom-boundary particles.

Different approaches based on various existing formulations of the diffusive terms can be considered in the SPH method to describe the momentum equation. Also, in the momentum equation, you can add a field of external forces, such as gravity:

$$\frac{dv_i}{dt} = -\sum_j m_j \left(\frac{p_j}{\rho_j^2} + \frac{p_i}{\rho_i^2} + \Pi_{ij} \right) \nabla_i W_{ij} + g_i, \quad (46)$$

where Π_{ij} is the viscosity term and $g_i = (0, 0, -9.81) m s^{-2}$ is the gravitational acceleration.

To describe the viscosity, the concept of artificial viscosity is introduced for pairs of particles. Under these empirical considerations and some modification of the numerical model empirical constants, the computational stability can be established with a reasonably small artificial viscosity coefficient α (see Eq. (47)):

$$v_{A,ij} = \frac{-\alpha \mu_{ij} \bar{c}_{ij}}{\bar{\rho}_{ij}}, \quad (47)$$

where the velocity-dependent variable is given by

$$\mu_{ij} = \frac{h(v_i - v_j) \cdot (x_i - x_j)}{(x_i - x_j)^2 + (0.01h^2)}. \quad (48)$$

The overbar is an averaging operator, i.e.,

$$\bar{\rho}_{ij} = \frac{1}{2}(\rho_i + \rho_j) \quad (49)$$

where ρ_i and ρ_j are the density at particles i and j , respectively:

$$\bar{c}_{ij} = \frac{1}{2}(c_i + c_j), \quad (50)$$

where c_i and c_j are the sound speed at particles i and j , respectively:

$$h = 1.2\Delta x \quad (51)$$

is the smoothing length, where $\Delta x (= \Delta x_1 = \Delta x_2)$ is the space step and α is a constant that depends on the particular type of simulation being run and requires careful numerical calibration. In this study, it is assumed that the sound speed is constant, i.e.,

$$\bar{c}_{ij} = c = 1440 m s^{-1}. \quad (52)$$

The SPH eddy viscosity at a fixed point $i = a$ is determined as

$$v_{SPH} = \frac{-\alpha c \sum_j \mu_j W_{aj}}{\sum_j \rho_j W_{aj}}, \quad (53)$$

where averaged viscosity at a fixed point is

$$\mu_{average} = \sum_j \mu_j W_{aj} \quad (54)$$

and averaged density of mass at a fixed point is

$$\rho_{average} = \sum_j \rho_j W_{aj}. \quad (55)$$

The density of each particle is

$$\rho_i = \sum_j m_j W_{ij}, \quad (56)$$

where the particle j mass is m_j and the interpolation kernel is W_{ij} . Direct calculation of density is mostly used in the case of water, which is considered as a weakly compressible fluid. Instead of using a weighted summation of mass terms (Monaghan, 1992), the initial density of each particle by Eq. (56) can be set, and it will only vary when particles move relative to each other.

Interaction between the particles on the boundary is described by the Lennard-Jones potential and fluid particle trajectories are determined using the Verlet method for 2D motion.

The fundamentals of the modified SPH method for free surface motion were described by Monaghan (1992); (1994); (2000).

3.4 Development of numerical model and comparison with experimental findings

The modified measurement data described in Section 2.4.2 and calculated averaged eddy viscosity in Section 2.4.5 were used for comparison with existing turbulence models. In author's **Publication III**, a numerical model was proposed and the resulting SPH eddy viscosity was compared with existing uniform, $k - \varepsilon$ and Smagorinsky eddy viscosity. Also, averaged eddy velocity developed by the author based on modified measurement data was added to the analysis.

3.4.1 Processing of numerical results

Numerical experiments were performed with the SPH model to simulate the wave breaking on the sloping bottom. Several modifications were introduced to the model setup. The numerical model domain was divided into two sections: 1) sloping bottom part and 2) horizontal bottom part. The sloping bottom 1:17 section was considered to be the same as in the physical model. The horizontal bottom between the reference point and the wave generator (Fig. 2) is considerably shortened. The reason is that a reduced number of particles per fluid volume allows speed-up of the numerical integration. The additional vertical extension in the sloping bottom end of the wave flume was used to keep the number of particles constant. However, to avoid particles loss due to overtopping from 2D geometrical boundaries, the special criterion in the open-code SPH model was included to detect particles overtopped and move them back to the computational domain.

The wave generator used in the numerical model produced free surface crests motion. This motion becomes apparent in the wave flume after the system self-oscillations vanish. The length of surface waves is around 4 meters and directly observed phase speed in the horizontal bottom part of the numerical model domain is approximately 1.75 m s^{-1} (cf. experimentally observed wave celerity in Table 1). The frequency of the wave absorbing in the sloping bottom is 0.5 Hz. There are different phases, i.e., forward and backward position of the plate of the flap-type generator, in the surface wave production. In the wave generator mode, clearly, the breaking of particles formed free surface. Regardless of a comparatively small number of particles, the wave production in the horizontal bottom and wave breaking along the sloping bottom is qualitatively in good agreement with the experimental observations of the surface boundary layer.

3.4.2 Comparison of experimental and numerical findings

The averaged eddy viscosity presented in Fig. 25 is compared with uniform eddy viscosity by Eq. (41), $k - \varepsilon$ model eddy viscosity by Eq. (13) and Smagorinsky model eddy viscosity by Eq. (42). Results show five different heights at one profile: Fig. 30 on 0.067 m; Fig. 31 on 0.052 m; Fig. 32 on 0.040 m; Fig. 33 on 0.028 m, and Fig. 34 on 0.006 m on the sloping bottom. Fig. 33 contains also SPH eddy viscosity by Eq. (53).

Figures 30-34 show that the first local maximum of the averaged eddy viscosity (continuous curve) at instants when the surface roller hits the water surface, i.e., dimensionless wave period interval 0.50 – 0.60, does not appear on any other eddy viscosity models. The second local maximum of the averaged eddy viscosity when the surface roller is passing the measuring point, i.e., dimensionless wave period interval 0.65 – 0.75, correlates well to the $k - \varepsilon$ model eddy viscosity predictions by Eq. (13) (short dashed curve). The third local maximum of the averaged eddy viscosity after the wave crest is passing the measuring point, i.e., dimensionless wave period interval 0.80 – 0.85, has a small variable on the $k - \varepsilon$ model eddy viscosity as well. At the same time, Smagorinsky model eddy viscosity, Eq. (42) (dash-dot curve) tends to cover over both the second and the third local maximum of the averaged eddy viscosity.

Uniform eddy viscosity based on the mixing length model in Eq. (41) (long dashed curve) shows a constant value of $5.4 \times 10^{-4} \text{ m}^2 \text{ s}^{-1}$. This value is higher than most of the previous eddy viscosity results, except on averaged eddy viscosity third local maximum on the surface and Smagorinsky eddy viscosity on the bottom. According to the numerically determined SPH eddy viscosity in Eq. (53) (dotted curve in Fig. 33), its local maximum is directly under the surface roller. However, within an entire wave period, SPH eddy viscosity gives higher values than the uniform eddy viscosity, which is related to averaging inside of the kernel.

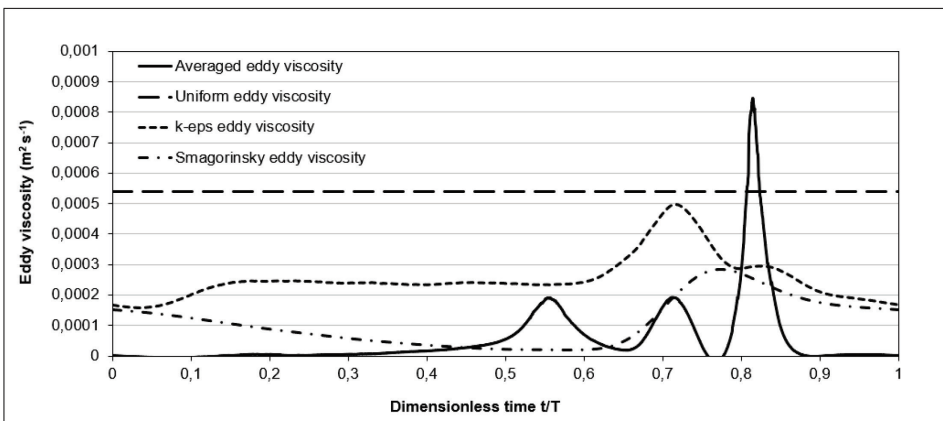


Figure 30. Eddy viscosity ν_T ($\text{m}^2 \text{ s}^{-1}$) estimates from different approximations: theoretically (averaged eddy viscosity) and empirically (uniform, $k - \varepsilon$ and Smagorinsky eddy viscosity) predicted 0.067 m above the sloping bottom.

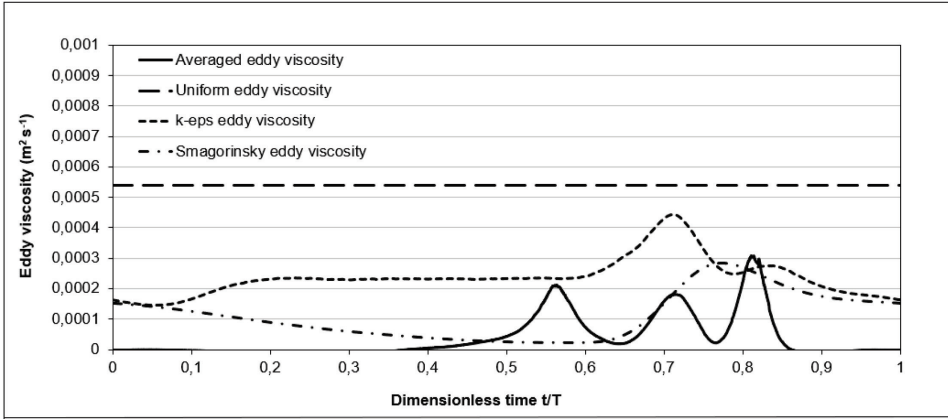


Figure 31. Eddy viscosity ν_T ($m^2 s^{-1}$) estimates from different approximations: theoretically (averaged eddy viscosity) and empirically (uniform, $k - \varepsilon$ and Smagorinsky eddy viscosity) predicted 0.052 m above the sloping bottom.

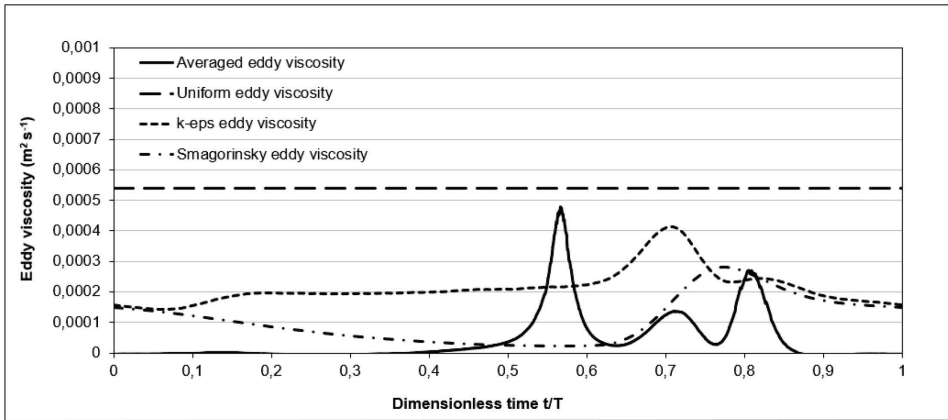


Figure 32. Eddy viscosity ν_T ($m^2 s^{-1}$) estimates from different approximations: theoretically (averaged eddy viscosity) and empirically (uniform, $k - \varepsilon$ and Smagorinsky eddy viscosity) predicted 0.040 m above the sloping bottom.

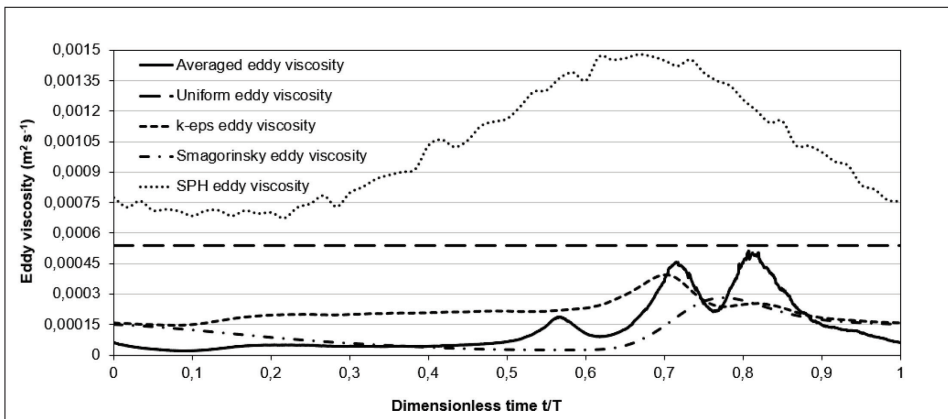


Figure 33. Eddy viscosity ν_T ($m^2 s^{-1}$) estimates from different approximations: theoretically (averaged eddy viscosity), empirically (uniform, $k - \varepsilon$ and Smagorinsky eddy viscosity) and numerically (SPH eddy viscosity) predicted 0.028 m above the sloping bottom.

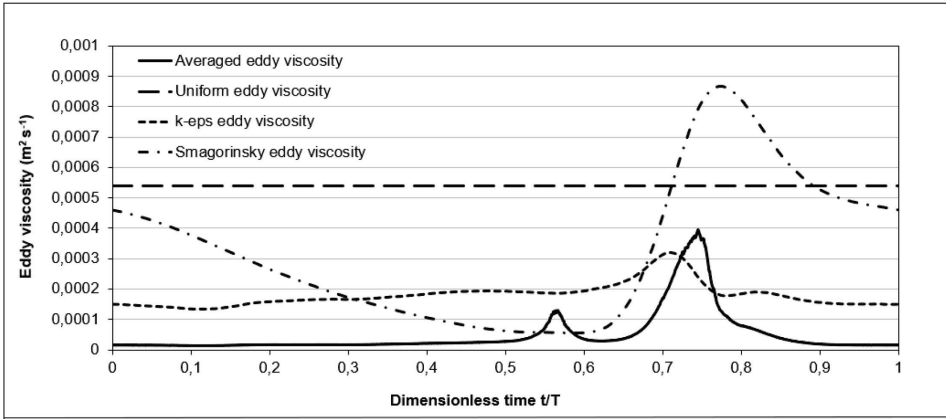


Figure 34. Eddy viscosity ν_T ($m^2 s^{-1}$) estimates from different approximations: theoretically (averaged eddy viscosity) and empirically (uniform, $k - \epsilon$ and Smagorinsky eddy viscosity) predicted 0.006 m above the sloping bottom.

4 Conclusions

Among issues to be dealt with in surf zone hydrodynamics, the accurate determination of eddy viscosity under breaking waves is the most problematic. Most hydrodynamic and sediment transport models tend to neglect the unsteady character of this term. This means that turbulent eddy viscosity on the seabed changes both in time and space.

The investigation of shear velocity in the boundary layer confirmed that the values of shear velocity vary both in time and space. It was shown that the maximum value of the term is always under the wave crest and the value decreases rapidly as the crest passes. The profiles of shear velocity under waves were found to be different in comparison to the corresponding profiles measured in U-pipes.

It was found that if eddy viscosity is determined based on the Boussinesq eddy viscosity assumption, then the results would contain singularities. It was revealed that spurious peaks and negative values in eddy viscosity are related to the velocity corresponding to a potential part of the flow where its gradient components do not represent the shear straining and manifest themselves when the shear stress and the velocity gradient change signs. It was found that if an irrotational flow was removed, the resulting eddy viscosity is positively valued during the whole wave period, which gives evidence that the modified velocity field corresponds well to the shear and compression strain.

The theoretically predicted eddy viscosity was derived from the combined functions of Reynolds stresses, modified mean velocity with its gradient components and turbulent kinetic energy for a compressible fluid. The irrotational flow that masked the turbulence velocity field under a breaking wave was removed using oscillating velocity at the bottom, and four depth dependent functions $A(x_2)$, $B(x_2)$, $C(x_2)$, $D(x_2)$ were used to modify the particular mean velocity gradient components.

Findings of this thesis

- The instantaneous eddy viscosity coefficient is positively valued during the wave period, which gives evidence of the modified velocity field corresponding well to the shear and compression strain that results from the bottom and surface boundary layers.
- Considering variations in the turbulent kinetic energy values during the wave period and over the water column, it is apparent from Eq. (6) and Eq. (7) that the eddy viscosity values are also changing over time and space.
- Regarding the new experimental findings, it can be suggested that using the coastal engineering models, the empirical and numerical predictions should follow the theoretical eddy viscosity time and space-dependent functions in the surf zone.
- It should be taken into account that the turbulence is generated both in the surface and bottom boundary layers, merge in the surf zone. Therefore, empirical predictions are unable to forecast the eddy viscosity values during the wave period and over the water column with acceptable accuracy.
- There is a direct correlation between maximum values of turbulent kinetic energy and eddy viscosity.
- It was demonstrated that the theoretically determined eddy viscosity values are in the same order of magnitude as the empirical and numerical

predictions, and follow reasonably well the production of turbulence during wave breaking.

- It was found that experimentally determined eddy viscosity is of higher complexity under a breaking wave on the sloping bottom than predictions of the empirical formulae.
- Also, it is required to improve the meshless numerical modelling to determine the artificial viscosity and the corresponding eddy viscosity more accurately by many particles “smeared” in space.
- It was found that the SPH eddy viscosity corresponds qualitatively well with the theoretical eddy viscosity determined from the combined functions of Reynolds stresses modified mean velocity and its gradient components and turbulent kinetic energy for a compressible fluid.

Future work

- Author considers an alternative option for the robustness of four depth dependent functions $A(x_2)$, $B(x_2)$, $C(x_2)$, $D(x_2)$ in modifying the mean velocity gradient components, by changing the cross coordinate system to the orthogonal coordinate system, which follows the velocity field.
- SPH modelling approach should be used more comprehensively in dealing with the counterparts of coastal processes, e.g., stratified flow mixing, air-water interaction and sediments transport in the surf zone due to wave breaking.

List of Figures

Figure 1. Breaker types.	14
Figure 2. Bird’s view of the wave flume: dimensions and notations.	17
Figure 3. Mean free-surface displacement for three profiles.	19
Figure 4. Wave characteristics 0.067 m above the sloping bottom from the measurements: a) horizontal velocity U_1 ($m\ s^{-1}$) (continuous curve) and vertical velocity U_2 ($m\ s^{-1}$) (dashed curve); b) horizontal velocity fluctuation u_1 ($m\ s^{-1}$) (continuous curve) and vertical velocity fluctuation u_2 ($m\ s^{-1}$) (dashed curve); c) horizontal velocity gradients along the channel direction $\partial U_1 \partial x_1$ (s^{-1}) (continuous curve) and horizontal velocity gradient in the channel vertical direction $\partial U_1 \partial x_2$ (s^{-1}) (dashed curve); d) vertical velocity gradient along the channel direction $\partial U_2 \partial x_1$ (s^{-1}) (continuous curve) and vertical velocity gradient along the channel vertical direction $\partial U_2 \partial x_2$ (s^{-1}) (dashed curve).	20
Figure 5. Wave characteristics 0.052 m above the sloping bottom from the measurements: a) velocities U_1 and U_2 ($m\ s^{-1}$); b) fluctuations u_1 and u_2 ($m\ s^{-1}$); c) velocity gradients $\partial U_1 \partial x_1$ and $\partial U_1 \partial x_2$ (s^{-1}); d) velocity gradients $\partial U_2 \partial x_1$ and $\partial U_2 \partial x_2$ (s^{-1}) (explanation to axis titles under Fig. 4).	21
Figure 6. Wave characteristics 0.040 m above the sloping bottom from the measurements: a) velocities U_1 and U_2 ($m\ s^{-1}$); b) fluctuations u_1 and u_2 ($m\ s^{-1}$); c) velocity gradients $\partial U_1 \partial x_1$ and $\partial U_1 \partial x_2$ (s^{-1}); d) velocity gradients $\partial U_2 \partial x_1$ and $\partial U_2 \partial x_2$ (s^{-1}) (explanation to axis titles under Fig. 4).	21
Figure 7. Wave characteristics 0.028 m above the sloping bottom from the measurements: a) velocities U_1 and U_2 ($m\ s^{-1}$); b) fluctuations u_1 and u_2 ($m\ s^{-1}$); c) velocity gradients $\partial U_1 \partial x_1$ and $\partial U_1 \partial x_2$ (s^{-1}); d) velocity gradients $\partial U_2 \partial x_1$ and $\partial U_2 \partial x_2$ (s^{-1}) (explanation to axis titles under Fig. 4).	22
Figure 8. Wave characteristics 0.006 m above the sloping bottom from the measurements: a) velocities U_1 and U_2 ($m\ s^{-1}$); b) fluctuations u_1 and u_2 ($m\ s^{-1}$); c) velocity gradients $\partial U_1 \partial x_1$ and $\partial U_1 \partial x_2$ (s^{-1}); d) velocity gradients $\partial U_2 \partial x_1$ and $\partial U_2 \partial x_2$ (s^{-1}) (explanation to axis titles under Fig. 4).	22
Figure 9. Classification of turbulence models.	26
Figure 10. Wave characteristics 0.067 m above the sloping bottom after irrotational flow removal: a) modified horizontal velocity U_{1t} ($m\ s^{-1}$) (continuous curve) and modified vertical velocity U_{2t} ($m\ s^{-1}$) (dashed curve); b) horizontal velocity fluctuations u_1 ($m\ s^{-1}$) (continuous curve) and vertical velocity fluctuation u_2 ($m\ s^{-1}$) (dashed curve); c) modified horizontal velocity gradient along the channel direction $\partial U_1 \partial x_{1t}$ (s^{-1}) (continuous curve) and modified horizontal velocity gradient in the channel vertical direction $\partial U_1 \partial x_{2t}$ (s^{-1}) (dashed curve); d) modified vertical velocity gradient along the channel direction $\partial U_2 \partial x_{1t}$ (s^{-1}) (continuous curve) and modified vertical velocity gradient along the channel vertical direction $\partial U_2 \partial x_{2t}$ (s^{-1}) (dashed curve).	33
Figure 11. Wave characteristics 0.052 m above the sloping bottom after irrotational flow removal: a) modified velocities U_{1t} and U_{2t} ($m\ s^{-1}$); b) fluctuations u_1 and u_2 ($m\ s^{-1}$); c) modified gradients $\partial U_1 \partial x_{1t}$ and $\partial U_1 \partial x_{2t}$ (s^{-1}) ; d) modified gradients $\partial U_2 \partial x_{1t}$ and $\partial U_2 \partial x_{2t}$ (s^{-1}) (explanation to axis titles under Fig. 10).	34

Figure 12. Wave characteristics 0.040 m above the sloping bottom after irrotational flow removal: a) modified velocities $U1t$ and $U2t$ ($m s^{-1}$); b) fluctuations $u1$ and $u2$ ($m s^{-1}$); c) modified gradients $\partial U1 \partial x1t$ and $\partial U1 \partial x2t$ (s^{-1}); d) modified gradients $\partial U2 \partial x1t$ and $\partial U2 \partial x2t$ (s^{-1}) (explanation to axis titles under Fig. 10). 34

Figure 13. Wave characteristics 0.028 m above the sloping bottom after irrotational flow removal: a) modified velocities $U1t$ and $U2t$ ($m s^{-1}$); b) fluctuations $u1$ and $u2$ ($m s^{-1}$); c) modified gradients $\partial U1 \partial x1t$ and $\partial U1 \partial x2t$ (s^{-1}); d) modified gradients $\partial U2 \partial x1t$ and $\partial U2 \partial x2t$ (s^{-1}) (explanation to axis titles under Fig. 10). 35

Figure 14. Wave characteristics 0.006 m above the sloping bottom after irrotational flow removal: a) modified velocities $U1t$ and $U2t$ ($m s^{-1}$); b) fluctuations $u1$ and $u2$ ($m s^{-1}$); c) modified gradients $\partial U1 \partial x1t$ and $\partial U1 \partial x2t$ (s^{-1}); d) modified gradients $\partial U2 \partial x1t$ and $\partial U2 \partial x2t$ (s^{-1}) (explanation to axis titles under Fig. 10). 35

Figure 15. Calculated shear velocity U^* ($m s^{-1}$) and local horizontal velocity $U1b$ ($m s^{-1}$) and vertical velocity $U2b$ ($m s^{-1}$) of 0.006 m above the sloping bottom..... 36

Figure 16. Correlation between the shear velocity U^* ($m s^{-1}$) (dots) and the mean free-surface displacement along the sloping bottom (continuous curve) on different dimensionless wave periods. 37

Figure 17. Measured turbulent kinetic energy kT ($m^2 s^{-2}$) on separate plots at different heights above the sloping bottom: a) 0.067 m; b) 0.052 m; c) 0.040 m; d) 0.028 m and e) 0.006 m. 38

Figure 18. Measured turbulent kinetic energy kT ($m^2 s^{-2}$) on the same plot at different heights above the sloping bottom: a) 0.067 m; b) 0.052 m; c) 0.040 m; d) 0.028 m and e) 0.006 m. 38

Figure 19. Measured turbulent production \mathcal{P} ($m^2 s^{-3}$) on the same plot at different heights above the sloping bottom: a) 0.067 m; b) 0.052 m; c) 0.040 m; d) 0.028 m and e) 0.006 m. 39

Figure 20. Eddy viscosity νT ($m^2 s^{-1}$) based on theoretical equations with the surface direction index i and the flow direction index j 0.067 m above the sloping bottom..... 39

Figure 21. Eddy viscosity νT ($m^2 s^{-1}$) based on theoretical equations with the surface direction index i and the flow direction index j 0.052 m above the sloping bottom..... 40

Figure 22. Eddy viscosity νT ($m^2 s^{-1}$) based on theoretical equations with the surface direction index i and the flow direction index j 0.040 m above the sloping bottom..... 40

Figure 23. Eddy viscosity νT ($m^2 s^{-1}$) based on theoretical equations with the surface direction index i and the flow direction index j 0.028 m above the sloping bottom..... 40

Figure 24. Eddy viscosity νT ($m^2 s^{-1}$) based on theoretical equations with the surface direction index i and the flow direction index j 0.006 m above the sloping bottom. 41

Figure 25. Averaged eddy viscosity νT ($m^2 s^{-1}$) values on separate plots based on theoretical equations with the surface direction index i and the flow direction index j at different heights above the sloping bottom: a) 0.067 m; b) 0.052 m; c) 0.040 m; d) 0.028 m and e) 0.006 m. 42

Figure 26. Averaged eddy viscosity νT ($m^2 s^{-1}$) values on a singular plot based on theoretical equations with the surface direction index i and the flow direction index j at different heights above the sloping bottom: a) 0.067 m; b) 0.052 m; c) 0.040 m; d) 0.028 m and e) 0.006 m. 42

Figure 27. Averaged eddy viscosity νT ($m^2 s^{-1}$) values over the water depth at the maximums shown in Fig. 25 and Fig. 26 in the dimensionless wave period: a) 0.245441; b) 0.568753; c) 0.711681 and d) 0.814687. 43

Figure 28. Measured turbulent kinetic energy kT ($m^2 s^{-2}$) values over the water depth at the averaged eddy viscosity maximums shown in Fig. 27 in the dimensionless wave period: a) 0.245441; b) 0.568753; c) 0.711681 and d) 0.814687..... 44

Figure 29. Particles representing fluid inside a smoothing area: a) liquid particles and b) liquid and bottom-boundary particles. 49

Figure 30. Eddy viscosity νT ($m^2 s^{-1}$) estimates from different approximations: theoretically (averaged eddy viscosity) and empirically (uniform, $k - \epsilon$ and Smagorinsky eddy viscosity) predicted 0.067 m above the sloping bottom..... 52

Figure 31. Eddy viscosity νT ($m^2 s^{-1}$) estimates from different approximations: theoretically (averaged eddy viscosity) and empirically (uniform, $k - \epsilon$ and Smagorinsky eddy viscosity) predicted 0.052 m above the sloping bottom..... 53

Figure 32. Eddy viscosity νT ($m^2 s^{-1}$) estimates from different approximations: theoretically (averaged eddy viscosity) and empirically (uniform, $k - \epsilon$ and Smagorinsky eddy viscosity) predicted 0.040 m above the sloping bottom..... 53

Figure 33. Eddy viscosity νT ($m^2 s^{-1}$) estimates from different approximations: theoretically (averaged eddy viscosity), empirically (uniform, $k - \epsilon$ and Smagorinsky eddy viscosity) and numerically (SPH eddy viscosity) predicted 0.028 m above the sloping bottom..... 53

Figure 34. Eddy viscosity νT ($m^2 s^{-1}$) estimates from different approximations: theoretically (averaged eddy viscosity) and empirically (uniform, $k - \epsilon$ and Smagorinsky eddy viscosity) predicted 0.006 m above the sloping bottom..... 54

List of Tables

Table 1. Regular wave characteristics	18
Table 2. Location of measuring points and corresponding wave parameters	18
Table 3. Maximum and minimum values of velocities and velocity fluctuations	23
Table 4. Maximum and minimum values of velocity gradients	23
Table 5. Change of functions Ax^2 , Bx^2 , Cx^2 , Dx^2 over depth	31

References

- Abe, K., Jang, Y.-J., & Leschziner, M. (2003). An investigation of wall-anisotropy expressions and length-scale equations for non-linear eddy-viscosity models. *International Journal of Heat and Fluid Flow*, *24*, 181–198.
- Absi, R. (2010). Concentration profiles for fine and coarse sediments suspended by waves over ripples: An analytical study with the 1-DV gradient diffusion model. *Advances in Water Resources*, *33*, 411–418.
- Apsley, D., & Leschziner, M. (1998). A new low-Reynolds-number nonlinear two-equation turbulent model for complex flows. *International Journal of Heat and Fluid Flow*, *19*, 209–222.
- Argyropoulos, C., & Markatos, N. (2015). Recent advances on the numerical modelling of turbulent flows. *Applied Mathematical Modelling*, *39*(2), 693–732.
- Arnaud, G., Mory, M., Abadie, S., & Cassen, M. (2009). Use of a resistive rods network to monitor bathymetric evolution in the surf/swash zone. *Journal of Coastal Research*, *SI 56*, 1781–1785.
- Austin, M., Masselink, G., Scott, T., & Russell, P. (2014). Water-level controls on macro-tidal rip currents. *Continental Shelf Research*, *75*, 28–40.
- Baldwin, B., & Barth, T. (1990). A One-Equation Turbulence Transport Model for High Reynolds Number Wall-Bounded Flows. *NASA Technical Memorandum*, 1–26.
- Baldwin, B., & Lomax, H. (1978). Thin Layer Approximation and Algebraic Model for Separated Turbulent Flows. *16th Aerospace Sciences Meeting* (pp. 78–257). Huntsville, AL, USA: AIAA.
- Barre de Saint Venant, A. (1871). Théorie du mouvement non-permanent des eaux, avec application aux crues des rivières et à l'introduction des marées dans leur lit. *C. R. Acad. Sci. Paris*, *73*, 147–154.
- Batchelor, G. (1967). *An Introduction to fluid dynamics*. Cambridge, United Kingdom: Cambridge University Press.
- Battjes, J. (1974). Surf Similarity. *14th International Conference on Coastal Engineering* (pp. 466–480). Copenhagen, Denmark: American Society of Civil Engineers.
- Battjes, J. A. (1988). Surf-zone dynamics. *Annual Review of Fluid Mechanics*, *20*, 257–291.
- Battjes, J., & Sakai, T. (1980). Velocity field in a steady breaker. In: *Proceedings 17th Conference on Coastal Engineering, Sydney, ASCE*, 499–511.
- Beach, R., & Sternberg, R. (1988). Suspended sediment transport in the surf zone: response to cross-shore infragravity motion. *Marine Geology*, *80*, 61–79.
- Benetazzo, A. (2006). Measurements of short water waves using stereo matched image sequences. *Coastal Engineering*, *53*, 1013–1032.
- Bertin, J. J., Periaux, J., & Ballmann, J. (1992). *Advances in Hypersonics: Modeling Hypersonic Flows*. Boston: Birkhäuser.
- Birkemeier, W., Donoghue, C., Long, C., Hathaway, K., & Baron, C. (1997). *1990 delilah nearshore experiment: summary report*. US Army Engineer Waterways Experiment Station: CHL-97-24.
- Black, K., & Rosenberg, M. (1992). Semi-empirical treatment of wave transformation outside and inside the breaker line. *Coastal Engineering*, *16*, 313–345.

- Boussinesq, J. (1872). Théorie des ondes et des remous qui se propagent le long d'un canal rectangulaire horizontal, en communiquant au liquide contenu dans ce canal des vitesses sensiblement pareilles de la surface au fond. *J. Math Pures et Appl. Deuxième Série*, 17, 55–108.
- Boussinesq, J. (1877). Essai sur la théorie des eaux courantes. *Mémoires présentés par divers savants à l'Académie des Sciences*, 23(1), 1–680.
- Bradshaw, P., Ferriss, D., & Atwell, N. (1967). Calculation of boundary layer development using the turbulent energy equation. *Journal of Fluid Mechanics*, 28, 593–616.
- Brevik, I. (1981). Oscillatory rough turbulent boundary layers. *Journal of Waterways, Port, Coastal and Ocean Engineering. ASCE*, 103, 175–188.
- Briganti, R., Musumeci, R. E., Bellotti, G., Brocchini, M., & Foti, E. (2004). Boussinesq modeling of breaking waves: Description of turbulence. *Journal of Geophysical Research*, 109(C07015), 1–17.
- Canuto, V. M., & Cheng, Y. (1997). Determination of Smagorinsky-Lilly constant C_s . *Physics of Fluids*(9), 1368.
- Capone, T., Panizzo, A., & Monaghan, J. (2010). SPH modelling of water waves generated by submarine landslides. *Journal of Hydraulic Research*, 48, 80–84.
- Chang, K.-A., & Liu, P.-F. (1999). Experimental investigation of turbulence generated by breaking waves in water of intermediate depth. *Physics of Fluids*, 11, 3339–3400.
- Courant, R., Friedrichs, K., & Lewy, H. (1967). On the Partial Difference Equations of Mathematical Physics. *IBM Journal of Research and Development*, 11(2), 215–234.
- Cox, D., Kobayashi, N., & Okayasu, A. (1996). Bottom shear stress in the surf zone. *Journal of Geophysical Research*, 101(C6), 14337–14348.
- Craft, T., Launder, B., & Suga, K. (1996). Development and application of a cubic eddy-viscosity model of turbulence. *International Journal of Heat and Fluid Flow*, 17, 108–115.
- Craft, T., Launder, B., & Suga, K. (1997). Prediction of turbulent transitional phenomena with a nonlinear eddy-viscosity model. *International Journal of Heat and Fluid Flow*, 18, 15–28.
- Dalrymple, R., & Rogers, B. (2006). Numerical modelling of water waves with the SPH method. *Coastal Engineering*, 53, 141–147.
- Davies, A. G., & Villaret, C. (1999). Eulerian drift induced by progressive waves above rippled and very rough beds. *Journal of Geophysical Research Atmospheres*, 104(C1), 1465–1488.
- De Padova, D., Dalrymple, R., Mossa, M., & Petrillo, A. (2009). SPH simulations of regular and irregular waves and their comparison with experimental data. *arXiv:0911.1872v1*.
- De Vries, S., De Schipper, M., Hill, D., & Stive, M. (2011). Remote sensing of surf zone waves using stereo imaging. *Coastal Engineering*, 58(3), 239–250.
- Deardorff, J. (1970). A numerical study of three-dimensional turbulent channel flow at large Reynolds numbers. *Journal of Fluid Mechanics*, 41(2), 453–480.
- Deigaard, R. (1993). A note on the three-dimensional shear stress distribution in a surf zone. *Coastal Engineering*, 20(1-2), 157–171.
- Divoky, D., Le Mehaute, B., & Lin, A. (1970). Breaking waves on gentle slopes. *Journal of Geophysical Research*, 75(9), 1681–1692.

- Ebersole, B., & Hughes, S. (1986). *Duck85 photopole experiment*. US Army Engineer Waterways Experiment Station: Misc. Paper CERC-87-8.
- Elgar, S., Raubenheimer, B., & Guza, R. (2001). Current Meter Performance in the Surf Zone. *Journal of Atmospheric and Oceanic Technology*, 18, 1735–1746.
- Fredsoe, J., & Deigaard, R. (1992). *Advanced Series on Ocean Engineering - Volume 3: Mechanics of coastal sediment transport*. Singapore: World Scientific.
- Gal, Y., Browne, M., & Lane, C. (2011). Automatic Estimation of Nearshore Wave Height from Video Timestacks. *2011 International Conference on Digital Image Computing: Techniques and Applications* (pp. 364–369). Noosa, QLD, Australia: IEEE.
- Galperin, B., & Orszag, S. (1993). *Large eddy simulation of complex engineering and geophysical flows*. Cambridge: Cambridge University Press.
- Galvin, C. (1968). Breaker type classification on three laboratory beaches. *Journal of Geophysical Research*, 73(12), 3651–3659.
- Gatski, T., & Speziale, C. (1993). On explicit algebraic stress models for complex turbulent flows. *Journal of Fluid Mechanics*, 254, 59–78.
- Gelfenbaum, G., & Smith, J. (1986). Experimental evaluation of a generalized suspended-sediment transport theory. *Shelf Sands and Sandstones - Memoir 11*, 133–144.
- Goda, Y. (2010). Reanalysis of regular and random breaking wave statistics. *Coastal Engineering Journal*, 52(1), 71–106.
- Gomez-Gesteira, M., Rogers, B., Dalrymple, R., & Crespo, A. (2010). State-of-the-art of classical SPH for free-surface flows. *Journal of Hydraulic Research*, 48, 6–27.
- Grant, W., & Madsen, O. (1979). Combined wave and current interaction with a rough bottom. *Journal of Geophysical Research*, 84(C4), 1797–1808.
- Green, A., & Naghdi, P. (1976). A derivation of equations for wave propagation in water of variable depth. *Journal of Fluid Mechanics*, 78, 237–246.
- Hansen, A., Carstensen, S., Christensen, D., & Aagaard, T. (2017). Performance of a tilt current meter in surf zone. *Proceedings of Coastal Dynamics 2017*, (pp. 944–954). Helsingor, Denmark.
- Holman, R., & Guza, R. (1984). Measuring Runup on Natural Beaches. *Coastal Engineering*, 8, 129–140.
- Holman, R., & Haller, M. (2013). Remote Sensing of the Nearshore. *Annual Review of Marine Science*, 5, 95–113.
- Hotta, S., & Mizuguchi, M. (1980). A Field Study of Wave in the Surf Zone. *Coastal Engineering in Japan*, 23, 59–79.
- Hsu, T.-W., & Jan, C.-D. (1998). Calibration of Businger-Arya type of eddy viscosity models parameters. *Journal of Waterway, Port, Coastal and Ocean Engineering*, 124(5), 281–284.
- Johnson, D., & King, L. (1985). A mathematically simple turbulence closure model for attached and separated turbulent boundary layers. *AIAA Journal*, 23, 1684–1692.
- Justesen, P. (1985). *The Turbulent Wave Boundary Layer: A theoretical study*. Technical University of Denmark: Institute of hydrodynamics and hydraulic engineering.
- Kajiura, K. (1968). A model of the bottom boundary layer in water waves. *Bulletin of the Earthquake Research Institute*, 46, 75–123.
- Kamphuis, J. (1991). Incipient wave breaking. *Coastal Engineering*, 15, 185–203.

- Kolmogorov, A. (1941). The Local Structure of Turbulence in Incompressible Viscous Fluid for Very Large Reynolds' Numbers. *Doklady Akademiia Nauk SSSR*, 30, 301–305.
- Kolmogorov, A. (1942). Equations of turbulent motion of an incompressible fluid. *Izv. Acad. Nauk USSR, ser. Fiz.*, 6, 56–58.
- Komar, P., & Gaughan, M. (1972). Airy wave theory and breaker height prediction. *Proceeding of 13th Coastal Engineering Conference*, (pp. 405–418). Vancouver.
- Kundu, P., & Cohen, I. (2010). *Fluid Mechanics*. United States: Elsevier Inc.
- Lauder, B. E., & Sharma, B. I. (1974). Application of the Energy-Dissipation Model of Turbulence to the Calculation of Flow Near a Spinning Disc. *Letters in Heat and Mass Transfer*, 1(2), 131–138.
- Le Mehaute, B., Divoky, D., & Lin, A. (1968). Shallow water waves: a comparison of theories and experiments. *In: Proceedings 1 lth Conference on Coastal Engineering, ASCE*, 86–107.
- Lee, E., Violeau, D., Issa, R., & Ploix, S. (2010). Application of weakly compressible and truly incompressible SPH to 3-D water collapse in waterworks. *Journal of Hydraulic Research*, 48, 50–60.
- Leendertse, J. (1967). *Aspects of a computational model for long-period water-wave propagation*. Santa Monica: Rand Corp. Mem. RM-5294-PR.
- Liiv, T. (2007). An experimental investigation of the oscillatory boundary layer around the breaking point. *Proceedings of the Estonian Academy of Sciences*, 13(3), 215–233.
- Liiv, T., & Lagemaa, P. (2008). The variation of the velocity and turbulent kinetic energy field in the wave in the vicinity of the breaking point. *Estonian Journal of Engineering*, 14(1), 42–64.
- Liu, H., & Sato, S. (2006). A two-phase flow model for asymmetric sheet-flow conditions. *Coastal Engineering*, 53, 825–843.
- Lundgren, H. (1972). Turbulent currents in the presence of waves. *Proceedings of 13th International Conference on Coastal Engineering* (pp. 623–634). Vancouver, Canada: American Society Of Civil Engineers.
- Lundgren, H., & Sorensen, T. (1958). A pulsating water tunnel. *Proceedings of 6th Conference on Coastal Engineering*, (pp. 356–358). Gainesville, Florida.
- Luracelli, A., Lugni, C., Falchi, M., Felli, M., & Brocchini, M. (2018). Extra Strain Rates in an unsteady spilling breaking wave. *Scientific Reports*, 8(13926), 1–8.
- MacCowan, J. (1894). On the highest waves of a permanent type. *Philosophical Magazine*, 38(5), 351–358.
- MacMahan, J., Brown, J., & Thornton, E. (2009). Low-Cost Handheld Global Positioning System for Measuring Surf-Zone Currents. *Journal of Coastal Research*, 25, 744–754.
- MacVicar, B., Beaulieu, E., Champagne, V., & Roy, A. (2007). Measuring water velocity in highly turbulent flows: field tests of an electromagnetic current meter (ECM) and an acoustic Doppler velocimeter (ADV). *Earth Surface Processes and Landforms*, 32, 1412–1432.
- Madsen, P., Murray, R., & Sorensen, O. (1991). A new form of the Boussinesq equations with improved linear dispersion characteristics. *Coastal Engineering*, 15, 371–388.
- Malarkey, J., & Davies, A. G. (2004). An eddy viscosity formulation for oscillatory flow over vortex ripples. *Journal of Geophysical Research*, 109(C12016), 1–13.

- Maresca, J., & Seibel, E. (1976). Terrestrial Photogrammetric Measurements of Breaking Waves and Longshore Currents in the Nearshore Zone. *Proceedings of the 15th Coastal Engineering Conference* (pp. 681–700). Honolulu, Hawaii: American Society of Civil Engineers.
- Menter, F. (1994). Two Equation Eddy Viscosity Turbulence Models for Engineering Applications. *AIAA Journal*, 32(8), 1598–1605.
- Monaghan, J. (1992). Smoothed particle hydrodynamics. *Annual Review of Astronomy and Astrophysics*, 30, 543–574.
- Monaghan, J. (1994). Simulating free surface flows with SPH. *Journal of Computational Physics*, 110, 399–406.
- Monaghan, J. (2000). SPH without a Tensile Instability. *Journal of Computational Physics*, 159, 290–311.
- Morris, J. (2000). Simulating surface tension with smoothed particle hydrodynamics. *International Journal for Numerical Methods in Fluids*, 33(3), 333–353.
- Myong, H., & Kasagi, N. (1990). Prediction of anisotropy of the near wall turbulence with an anisotropic low-Reynolds number $k-\epsilon$ turbulence model. *Journal of Fluids Engineering*, 112, 521–524.
- Myrhaug, D. (1982). On a theoretical model of rough turbulent wave boundary layers. *Ocean Engineering*, 9(6), 547–565.
- Nisizima, S., & Yoshizawa, A. (1987). Turbulent channel and Couette flows using an anisotropic $k-\epsilon$ model. *AIAA Journal*, 25, 414–420.
- Nwogu, O. (1993). Alternative form of Boussinesq equations for nearshore wave propagation. *J. Waterways Port Coast. Ocean Div. ASCE*, 119, 618–638.
- Ostendorf, D., & Madsen, O. (1979). *An analysis of longshore current and associated sediment transport in the surf zone*. Report No. 241, Department of Civil Engineering, MIT: 169.
- Peregrine, D. (1983). Breaking waves on beaches. *Annual Review of Fluid Mechanics*, 15, 149–178.
- Peregrine, D., & Svendsen, I. (1978). Spilling breakers, bores and hydraulic jumps. In: *Proceedings, 16th Conference on Coastal Engineering, ASCE*, 540–550.
- Perrier, G., Villaret, C., Davies, A. G., & Hansen, E. A. (1995). *Numerical modelling of the oscillatory boundary layer over ripples*. Gdansk, Poland: Delft Hydraulics.
- Petti, M., & Longo, S. (2001). Turbulence experiments in swash zone. *Coastal Engineering*, 43, 1–24.
- Piomelli, U., & Balaras, E. (2002). Wall-layer models for large-eddy simulations. *Annual Review of Fluid Mechanics*, 34, 349–374.
- Pope, S. (1975). A more general effective-viscosity hypothesis. *Journal of Fluid Mechanics*, 72, 331–340.
- Prandtl, L. (1925). Über die ausgebildete Turbulenz. *Journal of Applied Mathematics and Mechanics*, 5, 136–139.
- Prandtl, L. (1942). Bemerkungen zur Theorie der freien Turbulenz. *Journal of Applied Mathematics and Mechanics*, 22, 241–243.
- Prandtl, L., & Wieghardt, K. (1945). Über ein neues Formelsystem für die ausgebildete Turbulenz. *Nachr. Akad. Wiss. Göttingen, Math.-Phys. Klasse*, 6–19.
- Puleo, J. A., Mouraenko, O., & Hanes, D. M. (2004). One-dimensional wave bottom boundary layer model comparison: Specific eddy viscosity and turbulence closure models. *Journal of Waterway, Port, Coastal and Ocean Engineering*, 130, 322–325.

- Puleo, J., Faries, J., Davidson, M., & Hicks, B. (2010). A Conductivity Sensor for Nearbed Sediment Concentration Profiling. *Journal of Oceanic and Atmospheric Technology*, 27, 397–408.
- Puleo, J., Lanckriet, T., & Blenkinsopp, C. (2014). Bed level fluctuations in the inner surf and swash zone of a dissipative beach. *Marine Geology*, 349, 99–112.
- Puleo, J., Lanckriet, T., & Wang, P. (2012). Near bed cross-shore velocity profiles, bed shear stress and friction on the foreshore of a microtidal beach. *Coastal Engineering*, 68, 6–16.
- Rattanapitikon, W., & Shibayama, T. (2000). Verification and modification of breaker height formulas. *Coastal Engineering Journal*, 42(4), 389–406.
- Richard, G., Duran, A., & Fabreges, B. (2019). A new model of shoaling and breaking waves. Part 2. Run-up and two-dimensional waves. *Journal of Fluid Mechanics*, 867, 146–194.
- Ridd, P. (1992). A sediment level sensor for erosion and siltation detection. *Estuarine, Coastal and Shelf Science*, 35, 353–362.
- Robertson, B., Hall, K., Nistor, I., & Zytner, R. (2013). Breaking waves: Review of characteristic relationships. *COastal Engineering Journal*, 55(1), 1–40.
- Rodi, W. (1980). *Turbulence models and their application in hydraulics - A state of the art review*. Delft, The Netherlands: International Association for Hydraulic Research.
- Rodriguez, A., Sanchez-Arcilla, A., Redondo, J., & Mosso, C. (1999). Macroturbulence measurements with electromagnetic and ultrasonic sensors: a comparison under high-turbulent flows. *Experiments in Fluids*, 27, 31–42.
- Rogers, B., Dalrymple, R., & Stansby, P. (2010). Simulation of caisson breakwater movement using SPH. *Journal of Hydraulic Research*, 48, 135–141.
- Rosswog, S. (2015). SPH methods in the modelling of compact objects. *Living Reviews in Computational Astrophysics*, 1(1).
- Rubinstein, R., & Barton, J. (1990). Nonlinear Reynolds stress models and the renormalization-group. *Physics of Fluids A: Fluid Dynamics*, 2, 1472–1476.
- Santel, F., Linder, W., & Heipke, C. (2004). Stereoscopic 3d-image analysis of sea surface. *Proceedings of the ISPRS Commission V Symposium*, (pp. 708–712). Istanbul, Turkey.
- Saulter, A., Russell, P., Gallagher, E., & Miles, J. (2003). Observations of bed level change in a saturated surf zone. *Journal of Geophysical Research*, 108(C4), 1–15.
- Schmidt, W., Woodward, B., Millikan, K., Guza, R., Raubenheimer, B., & Elgar, S. (2003). A GPS-Tracked Surf Zone Drifter. *Journal of Atmospheric and Oceanic Technology*, 20, 1069–1075.
- Senechal, N., Abadie, S., Gallagher, E., MacMahan, J., Masselink, G., Michallet, H., . . . Garlan, T. (2011). The ECORS-Truc Vert'08 nearshore field experiment: presentation of a three-dimensional morphologic system in a macrotidal environment during consecutive extreme storm conditions. *Ocean Dynamics*, 61, 2073–2098.
- Seyama, A., & Kimura, A. (1988). The measured properties of irregular wave breaking and wave height change after breaking on a slope. *Proceedings 21th Conference of Coastal Engineering* (pp. 419–432). Costa del Sol-Malaga, Spain: American Society of Civil Engineers.

- Shand, T., Bailey, D., & Shand, R. (2012). Automated Detection of Breaking Wave Height Using an Optical Technique. *Journal of Coastal Research*, 28(3), 671–682.
- Shao, S. (2006). Simulation of breaking wave by SPH method coupled with k-e model. *Journal of Hydraulic Research*, 44(3), 338–349.
- Shields, I. (1936). *Application of similarity principles and turbulence research to bed-load movement*. Pasadena, CA: California Institute of Technology.
- Shih, T.-H., Zhu, J., & Lumley, J. L. (1996). Calculation of wall-bounded complex flows and free shear flows. *International Journal for Numerical Methods in Fluids*, 23, 1133–1144.
- Shih, T.-H., Zhu, J., & Lumley, J. (1993). *A realizable Reynolds stress algebraic equation model*. NASA Lewis Research Center: NASA tech. memo 105993.
- Simões, F. (2014). Shear velocity criterion for incipient motion of sediment. *Water Science and Engineering*, 7(2), 183–193.
- Smagorinsky, J. (1963). General Circulation Experiments with the Primitive Equations. *Monthly Weather Review*, 91(3), 99–164.
- Smith, A., & Cebeci, T. (1967). *Numerical solution of the turbulent-boundary-layer equations*. Douglas aircraft division.
- Smith, E., & Kraus, N. (1991). Laboratory study of wave breaking over bars and artificial reefs. *Journal of Waterway, Port, Coastal and Ocean Engineering*, 117(4), 307–325.
- Smith, J. (1977). *Modeling of sediment transport on continental shelves*. Interscience, N.Y.: In the Sea.
- Spalart, P., & Allmaras, S. (1994). A One-Equation Turbulence Model for Aerodynamic Flows. *La Recherche Aérospatiale*, 1, 5–21.
- Speziale, C. (1987). On nonlinear k-l and k-ε models of turbulence. *Journal of Fluid Mechanics*, 178, 459–475.
- Stive, M., & Wind, H. (1982). A study of radiation stress and set-up in the nearshore region. *Coastal Engineering*, 6, 1–25.
- Suga, K. (1995). *Development and application of a non-linear eddy viscosity model sensitized to stress and strain invariants*, PhD Thesis. Manchester, UK: Faculty of Technology, University of Manchester.
- Suhayda, N., & Pettigrew, J. (1977). Observation of Wave Height and Wave Celerity in the Surf Zone. *Journal of Geophysical Research*, 82(9), 1419–1424.
- Svendsen, I., Madsen, P., & Hansen, B. (1978). Wave characteristics in the surf zone. *In: Proceedings 16th Conference on Coastal Engineering, ASCE*, 520–539.
- Zarchan, P., & Musoff, H. (2000). *Fundamentals of Kalman Filtering: A Practical Approach*. University of Michigan: American Institute of Aeronautics and Astronautics.
- Terray, E., Brumley, B., & Strong, B. (1999). Measuring waves and currents with an upward-looking ADCP. *Proceedings of the IEEE 6th Working Conference on Current Measurement* (pp. 66–71). San Diego, CA, USA: IEEE.
- Ting, F., & Kirby, J. (1994). Observation of undertow and turbulence in a laboratory surf zone. *Coastal Engineering*, 24, 51–80.
- Ting, F., & Kirby, J. (1995). Dynamics of surf-zone turbulence in a strong plunging breaker. *Coastal Engineering*, 24, 177–204.
- Ting, F., & Kirby, J. (1996). Dynamics of surf-zone turbulence in a spilling breaker. *Coastal Engineering*, 27, 131–160.

- Toorman, E. (2000). *Analysis of near-wall turbulence modelling with k-e models*. Heverlee, Belgium: Hydraulics Laboratory K.U.Leuven.
- Van Rijn, L. (2007). Unified view of sediment transport by currents and waves II: Suspended transport. *Journal of Hydraulic Engineering*, 133(6), 668–689.
- Weggel, R. (1972). Maximum breaker height for design. *Proceedings of the International Conference on Coastal Engineering* (pp. 419–432). Vancouver, British Columbia, Canada: American Society of Civil Engineers.
- Weishar, L., & Byrne, R. (1978). Field study of breaking wave characteristics. *Coastal Engineering*, 16 (27), 487–506.
- Velasco, D., & Polonichko, V. (2009). Current, wave and tidal observations from a horizontal acoustic doppler profiler installed on scripps pier in LA Jolla, California, USA. *Coastal Structure 2007, Proceedings of the 5th International Conference* (pp. 1976–1986). Venice, Italy: World Scientific.
- Violeau, D., & Rogers, B. (2016). Smoothed particle hydrodynamics (SPH) for free-surface flows: past, present and future. *Journal of Hydraulic Research*, 1–26.
- Woelke, M. (2007). Eddy Viscosity Turbulence Models employed by Computational Fluid Dynamics. *Transactions of the Institute of AViation*, 4, 92–113.
- You, Z., Wilkinson, D., & Nielsen, P. (1992). Velocity distribution in turbulent oscillatory boundary layer. *Coastal Engineering*, 18, 21–38.

Acknowledgements

This work was carried out in the Department of Civil Engineering and Architecture at Tallinn University of Technology. Financial support for article publishing and conference attendance was provided by European Social Foundation financing task 1.2.4 Cooperation of Universities and Innovation Development, Doctoral School project “Civil Engineering and Environmental Engineering” code 1.2.0401.09-0080, Institutional Research Funding project IUT19-17 (“Dynamical processes in hydraulic networks, marine structures and sea environment”) and Estonian Ministry of Education and Research.

I owe my deepest gratitude to my original supervisor PhD Toomas Liiv who recommended this topic and guided me through the labyrinths of knowledge. Also, I am sincerely grateful to my supervisor from Tallinn University of Technology, Associate Professor Janek Laanearu, for suggesting new aspects for study and motivating me with his constructive comments for further efforts. I also express my warmest gratitude to late Professor Emeritus Uno Liiv, whom this subject was dear to his heart and with whom we had long discussions over the smallest details of eddies.

In addition, I would like to thank the Department of Civil Engineering and Architecture for the opportunity to study and research further in my field, with special thanks to Ene Pähn for her guiding hand. I am grateful to the staff of the School of Engineering Dean's Office for support and other staff of Tallinn University of Technology for help in the preparation of my thesis.

This thesis was made possible with full support from my family, friends and co-workers. My late mother and late father, who both were truly proud of me, even though I had doubts myself throughout the years – I am deeply sorrowed that neither of you were able to see me finish it. I am grateful to my partner Allan for pushing me to finish everything I started. My two best friends, Egge and Sigrid who I met thanks to my PhD studies, deserve special thanks for giving me all the motivative talks I needed. Thank you all for believing in me, being proud of my achievements, and sharing my dreams.

Abstract

Investigation of the Eddy Viscosity for a Breaking Wave in the Surf Zone

As the accurate determination of turbulent eddy viscosity under breaking waves is among the most problematic issues to be dealt with in the surf zone hydrodynamics, the thesis focuses on that topic. Most hydrodynamic and sediment transport models tend to neglect the unsteady character of this term. In this thesis, variations of eddy viscosity in the surf zone on the bottom of the smooth beach model were calculated and presented. Investigations showed that turbulent viscosity varies both in time and space as the wave propagates and is at least an order of magnitude larger than the corresponding molecular viscosity.

Using the Reynolds stress anisotropy for an incompressible fluid, it was found that the ensemble-averaged measured velocity predicted eddy viscosity is associated with peaks, which are absent in the broadly accepted empirical predictions. The instantaneous eddy viscosity coefficient was determined according to the Reynolds stresses, modified mean velocity and its gradient components and turbulent kinetic energy. The modified mean velocity and its derivatives improve eddy viscosity predictions during the wave period, which gives evidence that the velocity used corresponds well to a rotational part of the flow. In addition to the measurement predictions, empirical formulae were used to estimate the eddy viscosity values during the wave period. Furthermore, a meshless numerical model is proposed to determine artificial viscosity and demonstrate its dependence on eddy viscosity in the case of a weakly compressible fluid.

The thesis focuses on the results obtained during experimental runs in the wave flume of the Laboratory of Fluid Mechanics in Tallinn University of Technology. Experiments were performed on the beach model with an inclination of 1 to 17. Velocities were measured using 2D LDA apparatus in various profiles around the breaking point. Measurements were performed extremely close to the bed, allowing the calculation of bottom shear stresses under a wave.

Almost all works in the field of boundary layer flow under the breaking wave address a flow similar to the flow in an oscillating pressure tube. Although the two flows are similar, there are many differences. While wave motion is essentially an open boundary flow, oscillating pressure tube has no free surface; thus, only turbulence input can come from the solid boundary. The results achieved in such manner are therefore only similar to the results that can be achieved during measurements in the surf zone.

The present thesis deals with boundary layer measurements on an inclined bottom under breaking waves. The measurements over the whole wave cycle were carried out, and the shear velocity, turbulent kinetic energy and eddy viscosity under the breaking wave were calculated based on the measurements. It was found that there is a considerable space and time variation of these characteristics in the surf zone. The turbulence generated during the wave breaking changes the shape of the above-mentioned properties in comparison to the profile measured before breaking.

Lühikokkuvõte

Turbulentse viskoossusteguri määramine murdlaine piirkonnas ranna-alal

Käesolev dissertatsioon keskendub turbulentse viskoossusteguri teoreetilisele määramisele ranna-alal, kuna see on üks problemaatilisemaid küsimusi ranniku lainete hüdrodünaamikas. Mitmed hüdrodünaamika ja sette transpordi mudelid kasutavad empiirilisi valemid turbulentse viskoossusteguri jaoks. Käesolevas töös kasutatud teoreetiline valem turbulentse viskoossusteguri arvutamiseks murdlaine protsessis sileda kaldpõhjaga füüsilises mudelis aga näitab, et laine levimisel varieerub turbulentne viskoossustegur nii ajas kui ruumis ja on vähemalt ühe suurusjärgu võrra suurem kui vastav molekulaarne viskoossustegur.

Kasutades Reynoldsi pinge anisotroopsust kokkusurumatu vedeliku jaoks, leiti, et ansambli keskmestatud voolukiiruse põhjal määratud turbulentse viskoossusteguris esinesid singulaarsused, mis puudusid laialdaselt kasutatavate empiiriliste valemite arvutustulemustes. Seetõttu määrati turbulentne viskoossustegur Reynoldsi pingete, modifitseeritud keskmiste kiiruste ja nende tuletiste ning turbulentse kineetilise energia järgi. Modifitseeritud keskmised kiirused ja nende tuletised parendasid oluliselt turbulentse viskoossusteguri arväärtusi laineperioodi jooksul, millest võib järeldada, et matemaatiliselt muudetud kiirusväli vastas hästi pöörise ga keerisvälja tingimustele. Mõõtmistega saadud turbulentse viskoossusteguri arväärtusi võrreldi ka olemasolevate empiiriliste valemite arvutustulemustega, et näidata erinevate meetoditega saadud turbulentsete viskoossustegurite väärtusi laineperioodi jooksul. Lisanduvalt kasutati nõrgalt kokkusurutava vedeliku teooriat kunstliku viskoossusteguri leidmiseks SPH numbrilise mudeliga. Numbriliselt hinnatud kunstlikust viskoossustegurist tuletatud turbulentset viskoossustegurit võrreldi mõõtmistulemuste põhjal arvutatud turbulentse viskoossusteguriga.

Dissertatsioonis on kasutatud olemasolevaid Tallinna Tehnikaülikooli Hüdromehaanika katselaboratooriumi voolurennis liikuvate lainete eksperimentaalseid tulemusi. Katsed põhinesid ranniku füüsilisel mudelil kaldega 1:17. Kiirusväli mõõdeti lainerenni kaldpinnaga põhjal Doppleri laser anemomeetriga erinevates profiilides pinnalaine murdumispunkti lähiumbruses. Mõõtmised viidi läbi kogu veesügavuse ulatuses, kusjuures tihedamat mõõtmisammu kasutati renni põhja piirikihis. See võimaldas arvutada ostsilleeriva voolamise nihkepingeid põhja piirikihis.

Voolamise dünaamika modelleerimine murdlainega kaasnevas põhjalähedases piirikihis sarnaneb voolamise modelleerimisega ostsilleerivas rõhutorus. Kuigi vabavoolu ja survevoolu mittestatsionaarsed voolamised on sarnased, esineb siiski mitmeid erinevusi. Kui laine liikumisega kaasneb vaba pinnaga piirikiht, siis ostsilleerival voolamisel survetorus puudub vaba pind, mistõttu saab turbulents tekkida ainult fikseeritud pinnaga piirikihist. Rõhulise voolamisega kaasneva viskoosse voolamise dünaamika on ainult näiliselt sarnane vaba pinnaga viskoosse voolamise dünaamikale.

Käesolevas dissertatsioonis käsitletakse voolamise piirikihtide arenguga kaasnevaid turbulentsi parameetreid murdlaine all kaldpõhjal. Mõõtmised viidi läbi 151 laineperioodi jooksul ning nende põhjal arvutati murdlaine nihkekiirus, turbulentne kineetiline energia ja turbulentne viskoossustegur. Töö tulemusena on selgunud, et turbulentse viskoossusteguri määramiseks on vaja kasutada ortigonaalseid kõverjoonelisi koorinaate, mis võimaldavad viskoossusteguri määrata Reynoldsi pingetensori diagonaalelementidest.

Appendix

Publication I

Oldekop, N., & Liiv, T. (2013). Measurement of the variation of shear velocity on bed during a wave cycle. *Journal of Earth Science and Engineering*, 3(5), 322–330.

Measurement of the Variation of Shear Velocity on Bed during a Wave Cycle

Nelly Oldekop and Toomas Liiv

Department of Mechanics, Tallinn University of Technology, Tallinn 19086, Estonia

Received: March 14, 2013/Accepted: April 21, 2013/Published: May 25, 2013.

Abstract: Almost all works in the field of boundary layer flow under the breaking wave consider the flow similar as the flow in an oscillating pressure tube. Although the two flows are similar, there are many differences. The results achieved in such manner are therefore also only similar to the results that can be achieved during measurements in the surf zone. Present article deals with boundary layer measurements on an inclined bottom under breaking waves. The measurements over the whole wave cycle were carried out, and the shear velocity under the breaking wave was calculated based on the measurements. It was found that there is a considerable space and time variation of the term in the surf zone. The turbulence generated during the wave breaking changes the shape of the shear velocity profile in comparison to the profile measured before breaking. As the values of shear velocity are directly correlated with the description of the whole velocity field in the wave, it can be assumed that the enhanced description of the shear velocity results in better understanding of the whole velocity field under breaking waves. Therefore, the article brings a new insight into the field and aims to make a discussion about the need to rethink the way of describing the boundary layer flow in the surf zone.

Key words: Breaking wave, surf zone, turbulence, shear velocity, velocity distribution.

1. Introduction

The shear stresses and shear velocities on the bottom of the surf zone have been studied experimentally relatively little. A few has been mentioned in Refs. [1, 2]. These experiments are carried out using flush mounted constant temperature anemometer. The results of the last work are basis for many theoretical works on the oscillatory boundary layer. For example [3], the work, which shear velocities and shear stresses measured by Cox et al. [1] is taken as input. The theoretical work assumes that the velocity distribution is logarithmic during the whole wave period. Breaking wave boundary layer measurements carried out by Liiv [4] showed that the velocity distribution is directly dependent on the phase of the wave.

The work by Jonsson and Carlsen [5] that is the

basis for many theoretical researches in the field of breaking wave investigation is based on the experiments made in an oscillator U-tube. They presented their data as logarithmic velocity profiles that were in good correlation with the steady open channel velocity profile. It was shown in Ref. [4] that the steady open channel velocity profile fails to describe the flow in the breaking wave on an inclined bottom. This lead to the need of a better understanding of the shear velocities involved in the process.

All works so far have dealt with shear velocity in one point only. This means that based on the experiments, it is impossible to evaluate the dynamics of the shear velocity. This means that the change in shear velocity when spreading shoreward on a slope has not been investigated.

2. Setup and Procedures

The present study aims at narrowing the above mentioned gap. The experimental work of the present study aims at the determination of the unsteady flow

Corresponding author: Toomas Liiv, associated professor, research fields: wave dynamics and boundary layer flow. E-mail: toomas@corson.ee.

field parameters in the wave breaking. Main attention in the study was focused to the area close to the bottom of the surf zone model. Special attention was paid to the measurements in the viscous sub-layer. Based on the experiments performed in the wave flume of Tallinn University of Technology, the variation of the flow field during the breaking process has been investigated. For this purpose, regular waves were generated in the wave flume. The wave flume used was 0.6 m wide, 0.6 m deep and 22 m long (Fig. 1). Beach model with a slope 1:17 was situated in one end of the flume. The origin of coordinate system was taken at the still water level, where the inclination of the flume floor starts.

During current experimental run waves were generated with a constant wave period $T = 2.03$ s. The wave parameters describing the breaking wave are listed in Table 1. Here T is the wave period, h_b is water depth at the breaking point, including the change of the water level due to wave set-up, d_b is still water depth at the breaking point, x_b is the horizontal coordinate of the breaking point measured from the RP (reference point), H_0 is deep water wave height, is L_0 deep water wave length and H_b is wave height at the breaking point.

Experiments were carried out in 29 cross-sections along the bottom of the surf zone model using a 2D LDA (Lithium diisopropylamide) system. Cross-sections were concentrated around the breaking

point of the wave in the outer part of the surf zone (Table 2). The more detailed description of the setup and both measuring and data processing procedures are given in Ref. [4].

The present paper deals with results achieved in the determination of the shear velocity on the bottom.

The shear velocity is evaluated using measured near bed velocities at the lower boundary of an open channel:

$$u^* = \sqrt{\frac{\tau_b}{\rho}} \tag{1}$$

where, τ_b is the shear stress given at the boundary and ρ is the density of water.

The bottom shear stress is calculated based on the measurements in the breaking wave:

$$\tau_b = \mu \frac{du}{dy} \tag{2}$$

where, μ is the dynamic viscosity of the fluid and

$\frac{du}{dy}$ is the velocity gradient on the bottom.

The velocity gradient was determined based on the 0-velocity on the boundary and the velocity measured closest to the bed. The height above the bed of the first measuring point was determined according to Eq. (3).

The laser beams measuring the horizontal velocity component entered the flume under an angle (Fig. 2); it was possible to project the measuring volume to the very bottom of the flume. Thus, it can be said that the

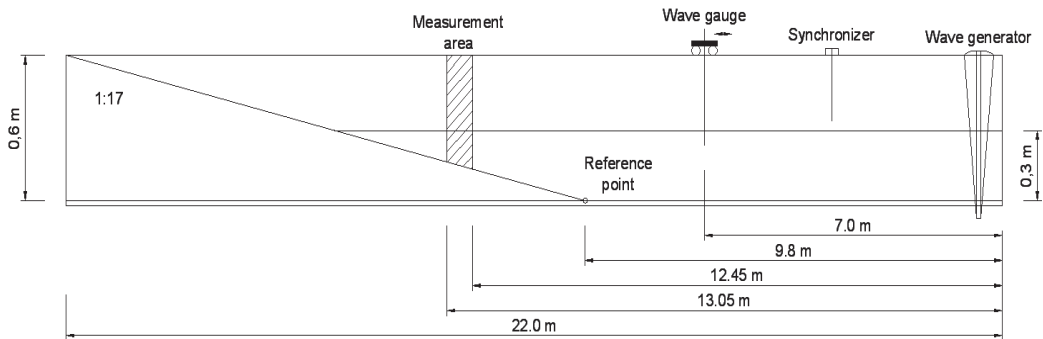


Fig. 1 Wave flume, dimensions in m.

Table 1 Parameters describing the breaking wave.

T (s)	h_b (m)	d_b (m)	x_b (m)	H_0 (m)	H_0/L_0	H_b (m)	H_b/d_b
2.0	0.106	0.111	2.90	0.072	0.012	0.118	1.06

Table 2 Location of measuring points and corresponding wave parameters.

Cross section No.	No. of points	Dis-tance from the RP x (m)	Depth d (m)	Depth h (m)	Wave celerity C (m/s)
29	47	3.21	0.089	0.089	0.933
28	47	3.18	0.091	0.091	0.944
27	48	3.15	0.093	0.093	0.955
26	50	3.12	0.095	0.095	0.964
25	51	3.09	0.098	0.097	0.975
24	51	3.06	0.100	0.099	0.983
23	53	3.03	0.102	0.100	0.990
22	54	3.00	0.104	0.101	0.997
21	55	2.97	0.106	0.102	1.001
20	58	2.94	0.108	0.104	1.010
19	58	2.91	0.110	0.104	1.012
18	61	2.82	0.117	0.114	1.059
17	61	2.81	0.118	0.115	1.064
16	62	2.80	0.118	0.116	1.069
15	62	2.79	0.119	0.117	1.071
14	65	2.78	0.120	0.118	1.077
13	65	2.77	0.120	0.119	1.079
12	64	2.76	0.121	0.119	1.082
11	66	2.75	0.122	0.120	1.086
10	63	2.74	0.123	0.121	1.090
9	67	2.73	0.123	0.121	1.091
8	69	2.72	0.124	0.122	1.094
7	69	2.71	0.125	0.123	1.098
6	70	2.70	0.125	0.124	1.101
5	70	2.69	0.126	0.124	1.104
4	70	2.68	0.127	0.125	1.108
3	69	2.67	0.128	0.126	1.111
2	76	2.66	0.128	0.127	1.115
1	151	2.65	0.129	0.127	1.117

height of the first measuring point is equal to one half of the shorter half axis of the measuring volume. Generally, the dimensions of the measuring volume can be calculated using the formulas:

$$\delta_x = \frac{4F\lambda}{\pi ED_L \cos\left(\frac{\theta}{2}\right)} \text{ and } \delta_z = \frac{4F\lambda}{\pi ED_L \sin\left(\frac{\theta}{2}\right)} \quad (3)$$

where, δ_x and δ_z are the measures of the shorter and longer axes of the measuring volume, λ is the wave length of the laser beam and E is the beam

expansion factor. The rest of the notation is illustrated in Fig. 2. This will give the value of the shorter half axis as 0.12 mm, which is of the same precision as the precision of mounting a hot film probe.

3. Experimental Results

The measured and calculated data are presented in two different ways. Firstly, ensemble averaged variation of the bottom shear velocity in different cross-sections (Figs. 3-5); secondly, the variation of shear velocity on the bottom over the surf zone (Figs. 6-11).

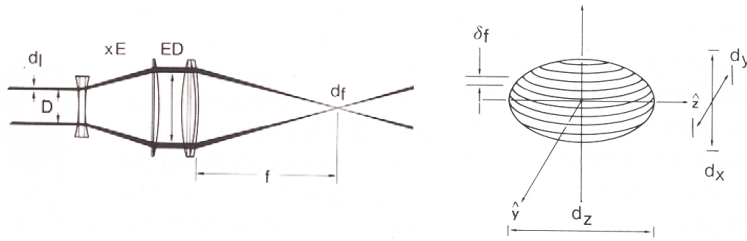


Fig. 2 Explanation to Eq. (3). D is the distance between the laser beams, d_l is the diameter of the laser beam, f is the focal distance of the frontal lens and θ is the angle between the laser beams.

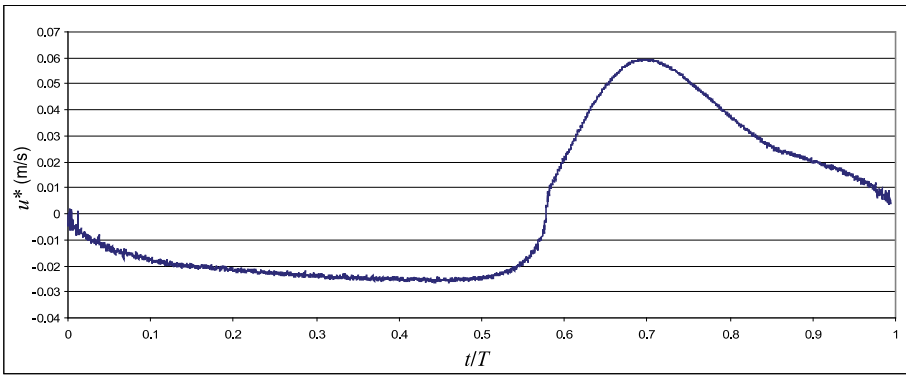


Fig. 3 Ensemble averaged variation of u^* over a wave period, $x = 2.65$ m.

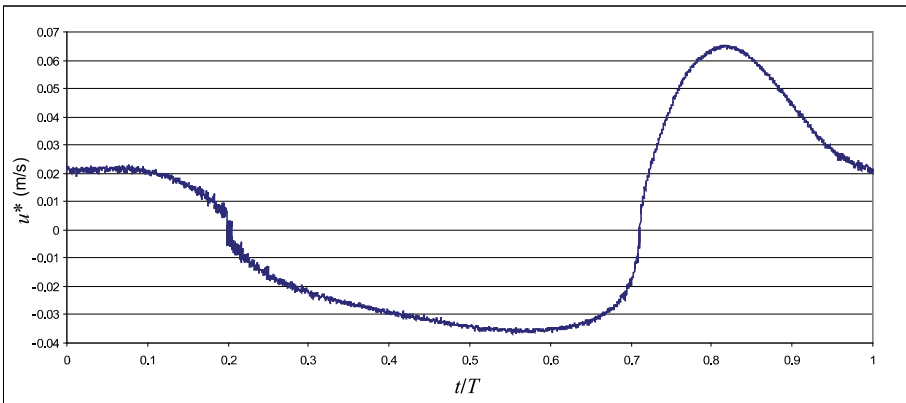


Fig. 4 Ensemble averaged variation of u^* over a wave period, $x = 2.91$ m.

Figs. 3-5 present the ensemble averaged shear velocity in different cross-sections. The figures represent a wave with the period of 2.03 s. The data were collected for 150 wave periods with a sampling frequency of 1,000 Hz, and later ensemble averaged.

The time scale for all three figures is the same, thus it enables the comparison of the data. It can be seen that at the given time moment the shear velocity is different in different cross-sections and the behaviour over the wave cycle varies different locations in the

surf zone.

Based on the ensemble averaged shear velocities in all 29 cross-sections, the following six figures present the variation of shear velocity on the bottom of the surf zone model at different dimensionless time moments. Also plotted on the figures are the surface elevations, which means water level below or above still water level.

Figs. 6-8 present the variation of u^* over the surf zone at $t/T = 0.1-0.5$. At these time moments, the measuring area was located entirely in the wave trough. The value of the shear velocity is nearly constant, directed slightly offshore. The exception is in Fig. 6, the area closest to the shoreline, where the momentum of the crest that has just left the measurement area is still effective.

The investigation of Figs. 9-11 shows that there is a good correlation between the surface elevation η and bottom shear velocity. The approaching wave crest increases the values of bottom shear velocity. It can also be seen that the value of shear velocity drops rapidly to the wave trough levels after the passing of the wave crest. It stays nearly constant under the wave trough. The investigation of the figures reveals that the direction of the shear velocity mainly follows the direction of the flow outside the boundary layer. An exception to the trend is the area directly in front of the wave crest. This is the area, where the jet generated by the overturning of the wave crest hits the water and reaches the bottom. It can be seen that despite the overall direction of the flow, the shear velocity is directed mainly towards the coastline.

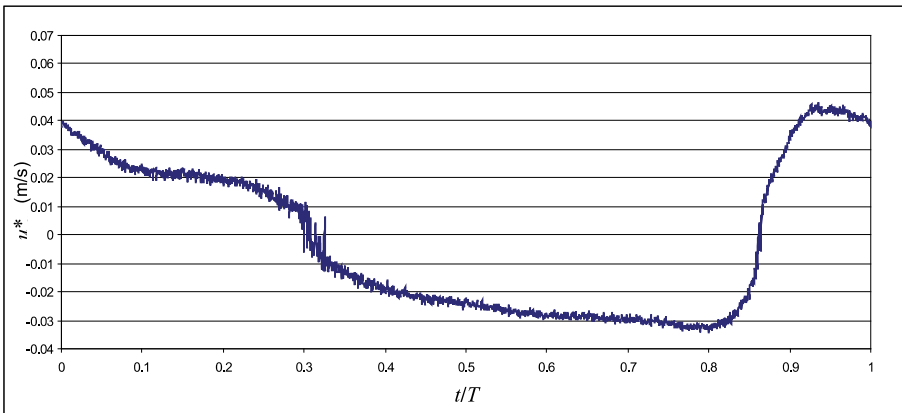


Fig. 5 Ensemble averaged variation of u^* over a wave period, $x = 3.15$ m.

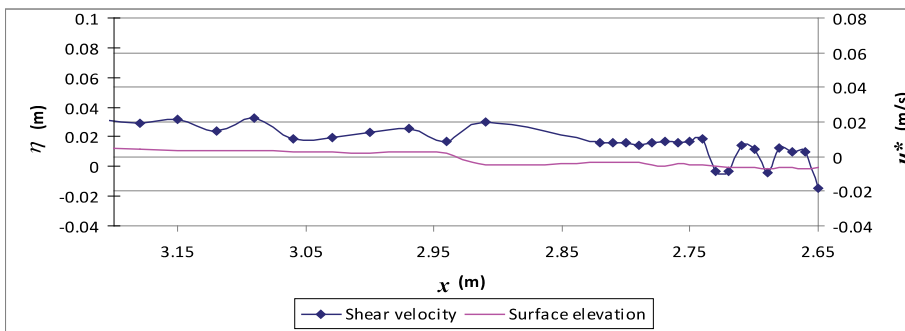


Fig. 6 The variation of u^* and η over the surf zone, $t/T = 0.1$. Horizontal axis gives distance from the origin and vertical is the shear velocity and surface elevation at current time moment.

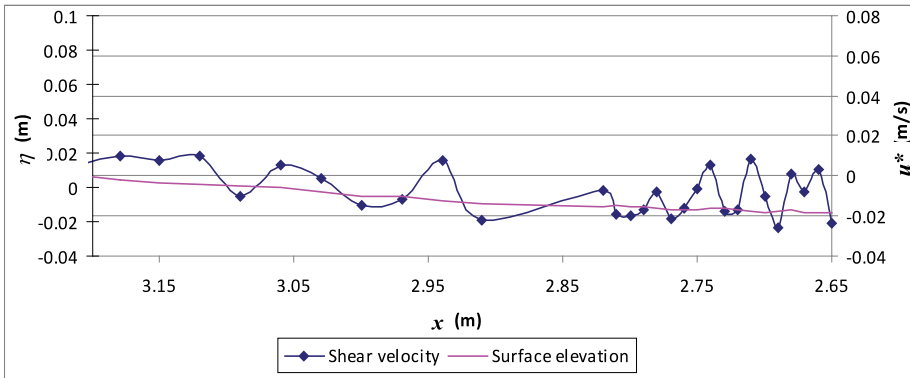


Fig. 7 The variation of u^* and η over the surf zone, $t/T = 0.3$. Horizontal axis gives distance from the origin and vertical is the shear velocity and surface elevation at current time moment.

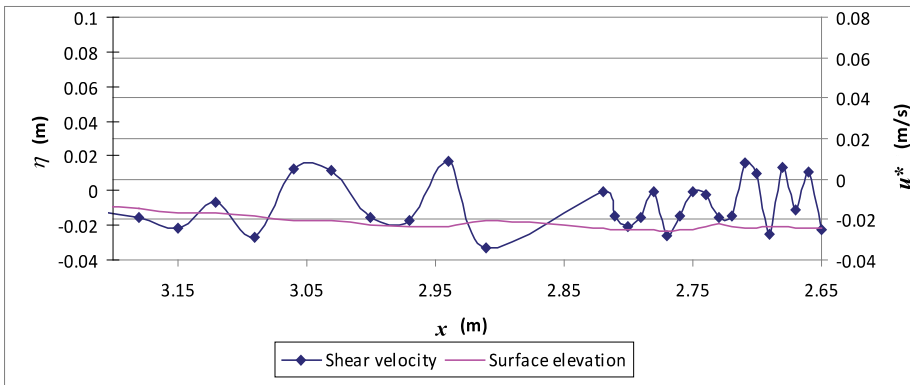


Fig. 8 The variation of u^* and η over the surf zone, $t/T = 0.5$. Horizontal axis gives distance from the origin and vertical is the shear velocity and surface elevation at current time moment.

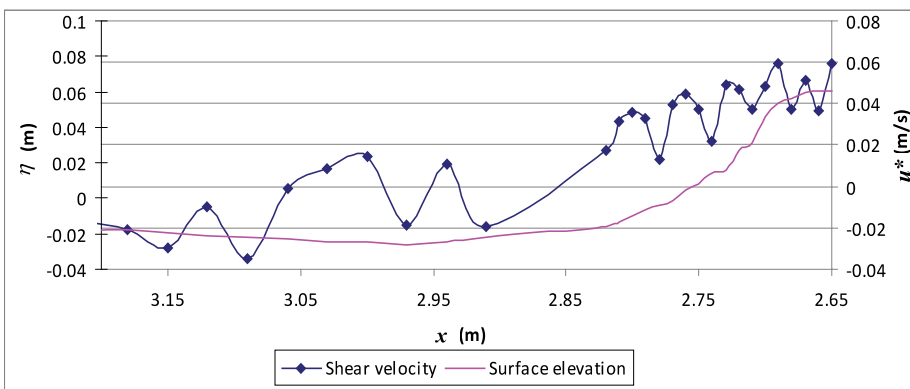


Fig. 9 The variation of u^* and η over the surf zone, $t/T = 0.7$. Horizontal axis gives distance from the origin and vertical is the shear velocity and surface elevation at current time moment.

Measurement of the Variation of Shear Velocity on Bed during a Wave Cycle

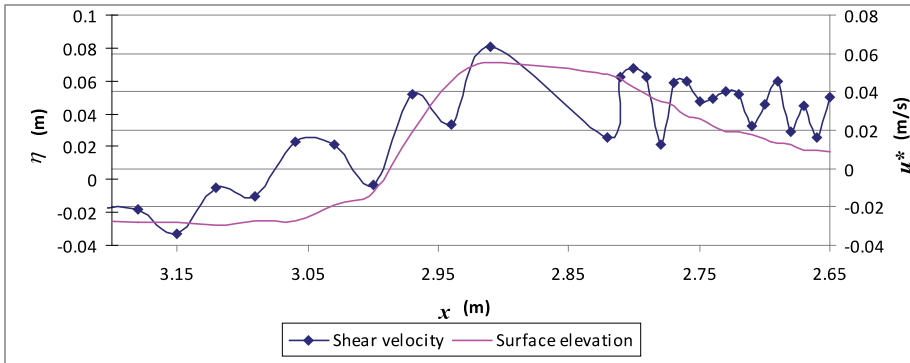


Fig. 10 The variation of u^* and η over the surf zone, $t/T = 0.8$. Horizontal axis gives distance from the origin and vertical is the shear velocity and surface elevation at current time moment.

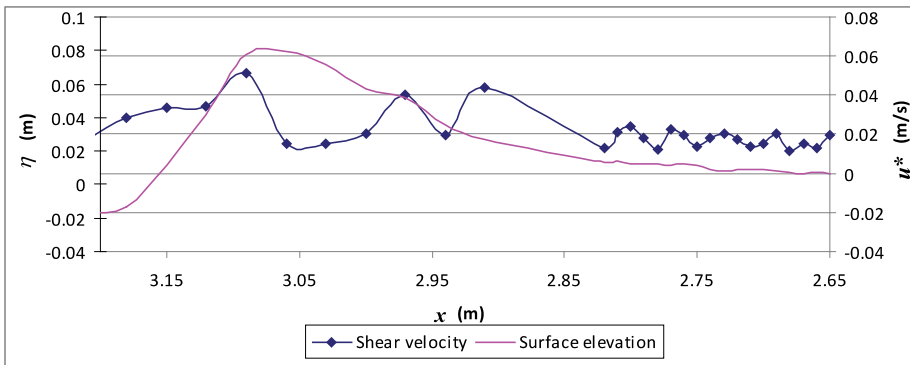


Fig. 11 The variation of u^* and η over the surf zone, $t/T = 0.9$. Horizontal axis gives distance from the origin and vertical is the shear velocity and surface elevation at current time moment.

4. Discussion

The obtained data prove that shear velocity under the breaking wave changes both in time and space. This confirms the previous investigations [4], which have shown that the common approach to describing the velocity in the boundary layer under a breaking wave is not adequate. As it was discussed earlier, most models describing breaking wave boundary layer flow use a velocity profile obtained from experiments of oscillating U-pipes. The choice between the U-pipe and open boundary flow is inclined towards the U-pipe mainly because of the better reliability of the measurements. In case of a hot film probe measurements, there is always a risk of contamination

through open surface. In case of a closed system, like a U-tube, there is no such problem. The assumption of similarity has been made in many investigations as the both oscillatory flow in U-pipe and wave motion have many similar features characterized with time dependent flow rate. At the same time, there are also many differences that can not be ignored. The two main differences that certainly have to be mentioned are the free surface oscillatory flow and the inclined bottom of the surf zone model. The presence of the free surface allows a rapid change of the cross-sectional area due to wave motion, and the generation of a two-phase environment (air-water) on the wave crest and after breaking point over the whole cross-sectional area. The inclined bottom of the flow

brings along issues of cross sectional change of the flow and therefore flow continuity and wave setup that have been noticed to affect wave properties.

The change of shear velocity in time is of great importance when thinking of possibilities of improving the existing mathematical description of boundary layer flow in the surf zone. The most widely used “crude” representation of the logarithmic profile is probably not valid at least during some phases of the flow.

The question of spatial variation is somewhat more intriguing. The question that needs to be determined is whether the obvious difference in values in the shear velocity in the outer and inner part of the surf zone results in the variation of the ratio of local velocity to the shear velocity. There would be no necessity for improving the models if the spatial variation of the shear velocity would be in correlation with the local velocities. However, the initial insight into the problem seems to indicate that there are factors that contribute to the importance of the phenomena. The issue of very low water depths of the wave troughs inside the inner surf zone raises the question of continuity effects to the flow. This needs to be studied further.

Investigation of data obtained during the measurements shows clearly that there is an area with high values of shear velocity travelling under the wave crest. As the velocity profile for logarithmic distribution is the ratio between local and shear velocity, it can be assumed that the steady flow velocity distribution is not valid in this area. This distribution seems to be valid for oscillatory flows in U-pipes [6]. The high shear velocities lead to more uniform velocity profile in comparison with the steady flow situation. This means that the mixing processes and momentum transfer are more effective in the described area.

5. Conclusions

The time variation over the wave period of shear

velocity on the bottom of the surf zone model has been measured experimentally both before and after the initial breaking of the wave has occurred. The results show that the values of shear velocity vary both in time and space in the surf zone. It can be observed that the maximum value is always under the wave crest and the value rapidly decreases after the crest has passed. It was found that the shear velocity profile is different from the shear velocity profile measured in experiments with an U-pipe, where there is a distinct half phases one directed towards the shoreline and one offshore. At the present case, it was found that the offshore flow phase is longer, but with lower shears velocity values.

It was found that the logarithmic velocity distribution of the steady flow that is commonly associated with flows in U-pipes is not valid in the flow under broken waves. This is most probably due to strong mixing processes during the breaking process.

Acknowledgments

Estonian Ministry of Education and Research is greatly acknowledged for funding and supporting this study. European Social Foundation financing task 1.2.4 Cooperation of Universities and Innovation Development, Doctoral School project “Civil Engineering and Environmental Engineering” code 1.2.0401.09-0080 has made publishing this article possible.

References

- [1] D.T. Cox, N. Kobayashi, A. Okayasu, Bottom shear stress in the surf zone, *Journal of Geophysical Research* 101 (C6) (1996) 14337-14348.
- [2] R. Deigaard, M.B. Mikkelsen, J. Fredsoe, Measurements of the Bed Shear Stress in the Surf Zone, Progress report ISVA, Technical University of Denmark, 1991.
- [3] S. Shin, Determination of the Shear Velocities, the Bottom Roughness and Friction Factors, Report 4, Oregon State University Lab of Oregon, 2004.
- [4] T. Liiv, An experimental investigation of the oscillatory boundary layer around the breaking point, *Engineering* 13 (2007) 215-233.

- [5] I.G. Jonsson, N.A. Carlsen, Experimental and theoretical investigations in an oscillatory boundary layer, *Journal Hydraulic Research* 14 (1976) 45-60.
- [6] B.L. Jensen, B.M. Sumer, J. Fredsoe, Turbulent oscillatory boundary layers at high Reynolds number, *Journal Fluid Mechanics* 206 (1989) 265-297.

Publication II

Oldekop, N., Liiv, T., & Lagemaa, P. (2015). The variation of eddy viscosity during wave breaking. *E-Proceedings of the 36th IAHR World Congress*, The Hague, Netherlands, 28 June – 3 July 2015, 1–5.

the variation of turbulent eddy viscosity during a wave cycle

NELLY OLDEKOP⁽¹⁾ & TOOMAS LIIV⁽²⁾

⁽¹⁾ *Department of Mechanics, Tallinn University of Technology, Tallinn, Estonia,
nelly@corson.ee*

⁽²⁾ *Department of Mechanics, Tallinn University of Technology, Tallinn, Estonia,
toomas@corson.ee*

ABSTRACT

One of the most problematic issues that have to be dealt with in connection with the surf zone hydrodynamics is the accurate determination of turbulent eddy viscosity under breaking waves. Most hydrodynamic and sediment transport models tend to neglect the unsteady character of this term. This means, that turbulent eddy viscosity on the seabed changes both in time and space.

This paper focuses on the results obtained during experimental runs in the wave flume of Laboratory of Fluid Mechanics in Tallinn University of Technology. Experiments were performed on the beach model with an inclination of 1 to 17. Velocities were measured using 2D LDA apparatus in various profiles around the breaking point. Measurements were performed extremely close to bed allowing the calculation of bottom shear stresses under wave.

The paper presents results of the study of turbulent eddy viscosity in the surf zone on the bottom of the hydraulically smooth beach model. It was found that turbulent viscosity varies both in time and space as the wave propagates and is at least an order of magnitude larger than the corresponding dynamic viscosity.

Keywords: boundary layer, breaking wave, turbulent eddy viscosity

1. INTRODUCTION

In recent years there has been numerous experiments carried out in the surf zone and not only in the laboratory. Feddersen et al. (2005) measured the wave generated turbulence in the surf zone and eventually developed a model that is able to reproduce the production and dissipation of turbulence during wave breaking. Trowbridge et al. (1995) measured the wave boundary layer. Their measurements indicate that there is a reduction in variance and the increase in phase relative to the flow outside the boundary layer. Bryan et al. (2003) investigated dissipation near the surf zone and Feddersen et al. (2007) measured the distribution of Reynolds stresses.

At the same time many of the mathematical models that calculate the time dependent velocity distribution of flow velocity in the boundary layer use the non-dimensional velocity profiles derived by Jensen (1989). This study is based on experiments conducted in a U-pipe with a rectangular cross-section. In 2013 Oldekop et al. proved that the friction velocity and thus also shear stress varies both in time and space. They showed that the commonly used values obtained from experiments in oscillatory U-pipes are not adequate to resolve the complex processes in the surf zone.

With the exception of the model by Trowbridge et al. (1984) most of the existing turbulent eddy viscosity models for oscillatory boundary layers assume that the turbulent eddy viscosity is a function of the distance from the bed and is not time-dependent. While most data show a general tendency for the local shear stresses to be out of phase with the local velocity gradients. One of the few studies that use time-dependent turbulent eddy viscosity models (Absi, 2006) predicts a sudden increase of the eddy viscosity near flow reversal.

2. EXPERIMENTAL SETUP

The following results on experimental investigation of oscillatory flow were obtained during experiments, described in Oldekop et al. (2013). The experiments were carried out in a wave flume with a surf zone of a constant slope of 1 to 17 (Figure 1). The aim of the investigation was to gather an insight into the flow structure and different hydrodynamic processes in the vicinity of the wave breaking point.

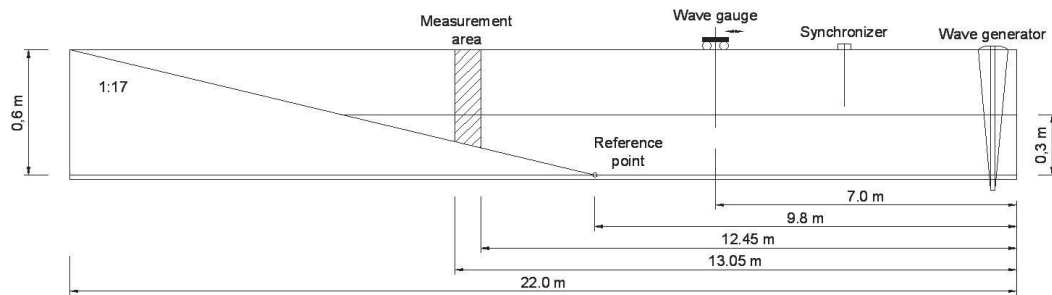


Figure 1. Schematics of the wave flume.

The velocity field inside the breaking waves was measured with the two-component argon-ion laser Doppler anemometer (LDA) with an output power of 1,3 W. Forward scatter mode was used throughout the experiment. As the LDA system allows measurement only at one point, the measurements were repeated over the 29 cross-sections (Table 1) and total of 1852 measuring points. Cross-sections were concentrated around the breaking point of the wave in the outer part of the surf zone.

Table 1. Location of measuring points and corresponding wave parameters.

Cross-section No.	No. of measuring points	Distance from the RP (m)	Still water depth d (m)	Water depth with wave	Wave celerity C (m/s)
			set-up h (m)		
29	47	3.21	0.089	0.089	0.933
28	47	3.18	0.091	0.091	0.944
27	48	3.15	0.093	0.093	0.955
26	50	3.12	0.095	0.095	0.964
25	51	3.09	0.098	0.097	0.975
24	51	3.06	0.100	0.099	0.983
23	53	3.03	0.102	0.100	0.990
22	54	3.00	0.104	0.101	0.997
21	55	2.97	0.106	0.102	1.001
20	58	2.94	0.108	0.104	1.010
19	58	2.91	0.110	0.104	1.012
18	61	2.82	0.117	0.114	1.059
17	61	2.81	0.118	0.115	1.064
16	62	2.80	0.118	0.116	1.069
15	62	2.79	0.119	0.117	1.071
14	65	2.78	0.120	0.118	1.077
13	65	2.77	0.120	0.119	1.079
12	64	2.76	0.121	0.119	1.082
11	66	2.75	0.122	0.120	1.086
10	63	2.74	0.123	0.121	1.090
9	67	2.73	0.123	0.121	1.091
8	69	2.72	0.124	0.122	1.094
7	69	2.71	0.125	0.123	1.098
6	70	2.70	0.125	0.124	1.101
5	70	2.69	0.126	0.124	1.104
4	70	2.68	0.127	0.125	1.108
3	69	2.67	0.128	0.126	1.111
2	76	2.66	0.128	0.127	1.115
1	151	2.65	0.129	0.127	1.117

During current experimental run, waves were generated with a constant wave period of $T=2.03$ s. The wave parameters describing the breaking wave are listed in Table 2. Here T is the wave period; h_b is water depth at the breaking point, including the change of the water level due to wave set-up; d_b is still water depth at the breaking point; x_b is the horizontal coordinate of the breaking point measured from the reference point (RP); H_0 is deep water wave height, L_0 is deep water wave length and H_b is wave height at the breaking point.

Table 2. Parameters describing the breaking wave.

T (s)	h_b (m)	d_b (m)	x_b (m)	H_0 (m)	H_0/L_0	H_b (m)	H_b/d_b
2.03	0.106	0.111	2.90	0.072	0.012	0.118	1.06

The data processing procedures and main results of investigations are described in Liiv et al. (2008). The main attention in the study was focused on the bottom of the surf zone, where data was collected with the vertical step of 1 mm. the closest measuring point to the bottom was considered to show the bottom shear velocity.

In order to evaluate the values of the shear velocity, measured in the described way, calibration calculations were made using the method proposed in Shin (2004).

During the experimental run both, horizontal and vertical components of the velocity, the corresponding signal dropouts, water level variation and signals from the synchronizing mechanism were saved. In order to achieve reliable results during ensemble averaging, data were collected from over 150 wave periods. Sampling frequency was 1000 Hz. For ensemble averaging a modified method was used (Petti et al. 2001).

The theoretical background and equations used for calculations turbulent eddy viscosity is described in detail in Oldekop et al. (2015).

3. EXPERIMENTAL RESULTS

Ensemble averaged variation of velocity gradient and turbulent eddy viscosity at various locations over the vertical are presented on Figure 4 and 6. Figure 3 and 5 give the corresponding horizontal and vertical velocities.

The time scale for all figures is the same, thus it enables to comparison of the data. We can see that at the given time moments the velocity gradient and the corresponding turbulent eddy viscosity are different over the wave period and the values vary significantly at different locations over the water column.

The values of turbulent eddy viscosity are nearly constant over the wave cycle, the values varying from -0.2×10^{-1} Pa.s to $+0.4 \times 10^{-1}$ Pa.s over the wave period. It has to be noticed that the dynamic viscosity mostly associated with the viscosity term is 1.002×10^{-3} Pa.s. This means, that turbulent eddy viscosity is nearly 2 orders of magnitude larger than dynamic viscosity. However there is a distinct increase in the values, occurring every time the velocity gradient du/dy goes though zero. Fluctuations in turbulent eddy viscosity can vary from -75 Pa.s to 150 Pa.s. This shows that we experience a periodical 10^3 time increase in the values of turbulent eddy viscosity under wave

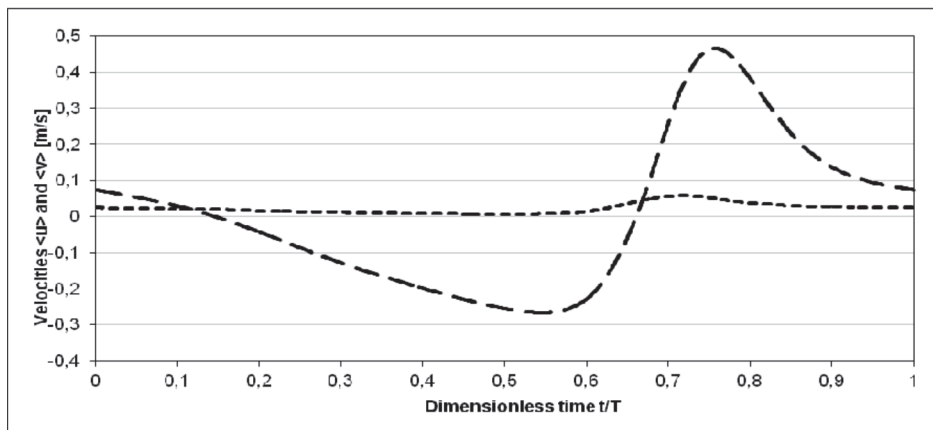


Figure 3. Velocity components u (dashed line) and v (dotted line) in the bottom boundary layer.

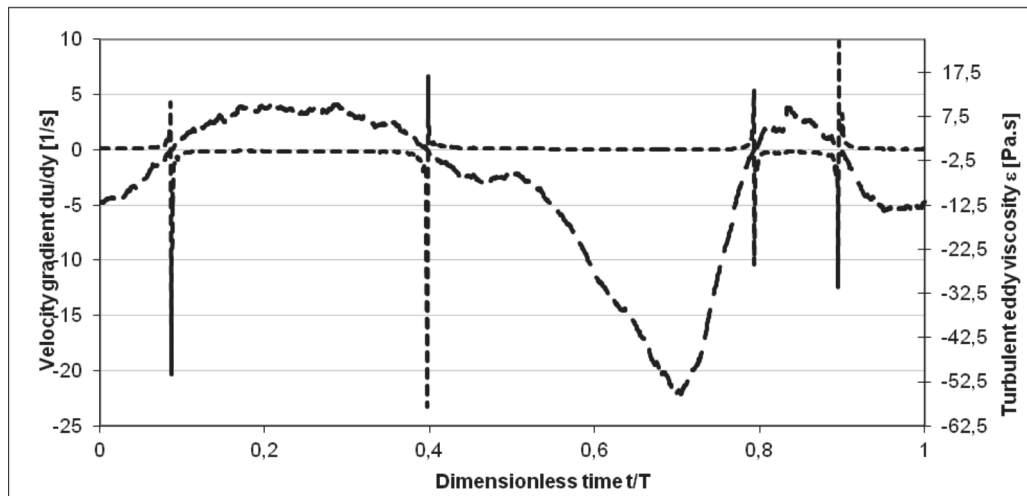


Figure 4. Velocity gradient du/dy (dashed line) and turbulent eddy viscosity ε (dotted line) in the bottom boundary layer.

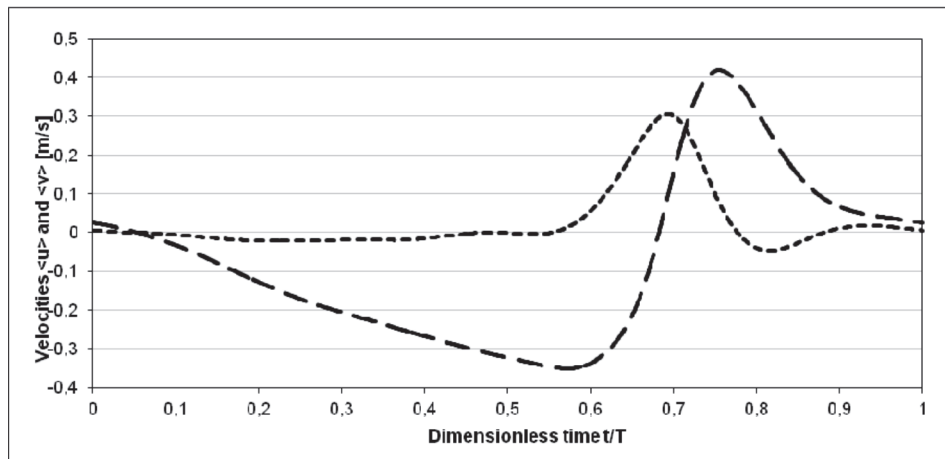


Figure 5. Velocity components u (dashed line) and v (dotted line) in the upper boundary layer.

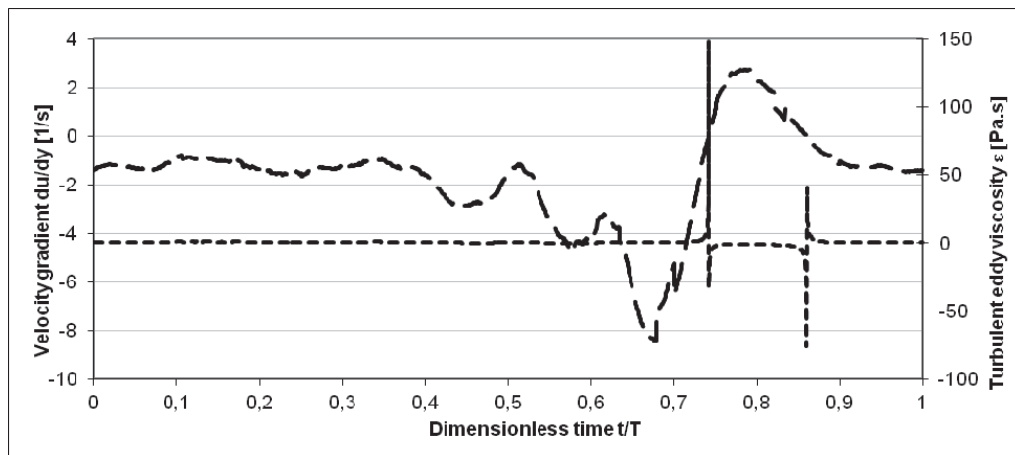


Figure 6. Velocity gradient du/dy (dashed line) and turbulent eddy viscosity ε (dotted line) in the upper boundary layer.

4. DISCUSSION

It can be detected from the data on turbulent eddy viscosity that the variation of the value over the wave period follows a distinct pattern. Absi (2006) suggested that the time-dependent turbulent eddy viscosity model predicts a sudden increase of the turbulent eddy viscosity near flow reversal. Present results do not support this assumption. The comparison of the corresponding data, Figure 4 as well as Figure 6 show that the increase in the values of turbulent eddy viscosity is more likely connected with the sign of the velocity gradient du/dy . At flow reversals at $t/T=0.65$ the turbulent eddy viscosity shows no activity.

It is interesting that the high activity in the turbulent eddy viscosity does not happen simultaneously over the water column. In the bottom layers there are considerably more spikes, while the value of the turbulent eddy viscosity is lower than in the upper layer. This is somewhat predictable as the turbulent energy generation near the surface is concentrated into the wave crest.

5. CONCLUSIONS

In the present study, an experimental data was used to calculate ensemble-averaged turbulent eddy viscosity.

It was found that turbulent eddy viscosity varies both in time and space as the wave propagates and is at least two orders of magnitude larger than the corresponding dynamic viscosity. Although more research on the topic is needed, the results prove the necessity for re-evaluating the usage of data collected in U-pipes as source terms for hydrodynamic and sediment transport models.

ACKNOWLEDGMENTS

Estonian Ministry of Education and Research is greatly acknowledged for funding and supporting this study.

REFERENCES

- Absi R. (2006). A roughness and time dependent mixing length equation. *Journal of Hydraulic, Coastal and Environmental Engineering (Doboku Gakkai Ronbunshuu B)*, Japan Society of Civil Engineers, 62 (4), 437-446.
- Bryan K.R., Black K.P., Gorman R.M. (2003). Spectral estimates of dissipation rate within and near the surf zone. *Journal of Physical Oceanography*, 979-993.
- Fedderson F., Trowbridge J.H. (2005). The effect of wave breaking on surf-zone turbulence and alongshore currents: a modelling study. *Journal of Physical Oceanography*, 35, 2187-2202.
- Fedderson F., Williams A.J. (2007). A direct estimation of the Reynolds stress vertical structure in the nearshore. *Journal of Atmospheric and Oceanic Technology*, 24, 102-116.
- Jensen B.L. (1989). Experimental investigation of turbulent oscillatory boundary layers. Series Paper 45. *Institute of Hydrodynamics and Hydraulic Engineering (ISVA)*, Technical University of Denmark, 157 p.
- Liiv T., Lagemaa P. (2008). The variation of the velocity and turbulent kinetic energy field in the wave in the vicinity of the breaking point. *Estonian Journal of Engineering*, 14 (1), 42-64.
- Oldekop N., Liiv T. (2013). Measurement of the Variation of Shear Velocity on Bed during a Wave Cycle. *Journal of Earth Science and Engineering*, 3 (5), 322-330.
- Oldekop N., Liiv T., Lagemaa P. (2015). The variation of turbulent eddy viscosity during a wave breaking. *Forthcoming*
- Petti M., Longo S. (2001). Turbulence experiments in swash zone. *Coastal Engineering*, 43, 1-24.
- Shin S. (2004). Determination of the shear velocities, the bottom roughness and friction factors. *Oregon Sate University, Lab of Oregon, report 14*.
- Trowbridge J.H., Madsen O.S. (1984). Turbulent wave boundary layers I. model formulation and first order solution. *Journal of Geophysical Research*, 89 (C5),7989-7997.
- Trowbridge J.H., Agrawal Y.C. (1995). Glimpses of wave boundary layer. *Journal of Geophysical Research*, 100 (C10), 20729-20743.

Publication III

Oldekop, N., Liiv, T. & Laanearu, J. (2019). Experimental study of eddy viscosity for breaking waves on sloping bottom and comparisons with empirical and numerical predictions. *Proceedings of the Estonian Academy of Sciences*, 68(3), 299–312.



Experimental study of eddy viscosity for breaking waves on sloping bottom and comparisons with empirical and numerical predictions

Nelly Oldekop^{a*}, Toomas Liiv^b, and Janek Laanearu^a

^a Department of Civil Engineering and Architecture, School of Engineering, Tallinn University of Technology, Ehitajate tee 5, 19086 Tallinn, Estonia

^b Corson LLC, Laki 14a-704, 10621 Tallinn, Estonia

Received 8 February 2019, accepted 6 May 2019, available online 30 June 2019

© 2019 Authors. This is an Open Access article distributed under the terms and conditions of the Creative Commons Attribution-NonCommercial 4.0 International License (<http://creativecommons.org/licenses/by-nc/4.0/>).

Abstract. Focus is on the turbulence for a plunging breaker. Laser Doppler anemometer point measurements were used to determine the velocity matrix of a breaking wave on a sloping bottom. Using the Reynolds stress anisotropy for incompressible fluid, it was found that the ensemble averaged measured velocity predicted eddy viscosity is associated with peaks, which are absent in the broadly accepted empirical predictions. The instantaneous eddy viscosity coefficient was determined according to the Reynolds stresses, modified mean velocity and its gradient components and turbulent kinetic energy. The modified mean velocity and its derivatives improve eddy viscosity predictions during the wave period, which gives evidence that the velocity used corresponds well to a rotational part. In addition to the measurement predictions, empirical formulae were used to estimate the eddy viscosity values during the wave period. Furthermore, a meshless numerical model is proposed to determine artificial viscosity and demonstrate its dependence on eddy viscosity in the case of weakly compressible fluid.

Key words: artificial viscosity, breaking wave, eddy viscosity, experiment, turbulence.

1. INTRODUCTION

In the process of nearshore wave breaking, the sloping bottom can be a solid body such as a rock or a set of small mobile particles as sediments. Wave breaking is of high significance in the coastal process, which is responsible for nearshore sediment transport and concurrent development of bed forms. The knowledge of wave breaking is needed to solve a number of the coastal engineering problems associated with the bottom changes, pollution propagation and wave forces on coastal structures. The bottom and surface boundary layers are treated in very different ways in the coastal engineering models. The turbulence is generated both in the surface and bottom boundary layers, which merge in the surf zone. The coastal environment represents a complex dynamical system, where waves and currents interact with bed forms (Laanearu et al., 2007). An ability to predict the geometrical characteristics of the bed forms in the coastal zone under wave action requires an accurate representation of the physics of the sediment transport processes. The effects of waves on morphodynamical changes depend on the wave's Reynolds number

* Corresponding author, nelly@corson.ee

and the frictional factor of the boundary layer (Madsen and Grant, 1976). To compliment previous works that are using empirical criteria by giving a more flexible and accurate description of the turbulence due to a breaking wave, the eddy viscosity profiles are needed for more accurate nearshore wave modelling (Briganti et al., 2004). The deformation of the wave profile in the surf zone is essentially due to the bottom shapes, whereas the surface waves approaching the coast lose their momentum in the attenuation related to the bottom stress, breaking of surface and concurrent reflection processes due to the run-up. Research progress on the breaking waves and the surf zone dynamics is reviewed by Peregrine (1983), Battjes (1988), and Svendsen and Putrevu (1996).

Detailed modelling of turbulence in breaking waves is a difficult task for a number of reasons; the velocity field during breaking is extremely chaotic and varies rapidly in space and time. Available models can handle most of wave phenomena, such as shoaling, refraction, diffraction, but prediction of the breaking event is challenging. Surface breaking is associated with the irreversible transformation of potential velocity field into motions of different types and scales, including the turbulence, vortices and air-water interactions. Therefore, in the coastal engineering studies, the meshless numerical modelling, such as Smoothed Particle Hydrodynamics (SPH) solvers, is becoming more useful (Monaghan, 1994). It has been demonstrated that the SPH models are suitable to reproduce free surface phenomena such as a breaking wave (Dalrymple and Rogers, 2006; Shao, 2006; De Padova et al., 2009), dam breaks (Gomez-Gesteira et al., 2010; Lee et al., 2010), whitewater formation (Morris, 2000), waves overtopping of harbour structures (Rogers et al., 2010), tsunamis generated landslide (Capone et al., 2010). However, the near-bottom velocity modelling is problematic in SPH, which may complicate solving practical coastal engineering problems.

Extensive experimental work on coastal hydrodynamics and sediment transport in the laboratories is targeted to understanding complicated dynamics involved in accurate field measurements. However, as the size of most wave flumes is fairly limited, it is difficult to obtain adequately large values of the Reynolds number for modelling boundary layer dynamics. Therefore, for a simplified experimental setup, a U-shaped oscillating tunnel (U-tube) is suggested by Lundgren and Sorensen (1958), where the orbital motion in the test section differs from the real wave induced flow by being entirely uniform in the along tube direction and by having no vertical orbital motion. In this study, the wall generated turbulence, as in the U-tube experiments, is complemented with the turbulence generated at free surface, which is absent in the U-tube oscillating flow. The U-shape oscillatory wave motion is an acceptable solution for modelling characteristics of the wave bottom boundary layer on a constant water depth with regular non-breaking waves. However, the method is lacking accuracy on the sloping bottom with breaking waves, where the free surface generated turbulence can extend into a full water column. Studies by Ting and Kirby (1994, 1995, and 1996), Chang and Liu (1999) and Liiv (2007) have reported laboratory measurements of velocities and turbulence intensities in periodic breaking waves. All of these measurements were recorded by a laser Doppler anemometer (LDA). The latest of these experiments reported by Liiv (2007) is revisited herein to make use of the novel unpublished experimental data.

Many empirical models are available to deal with the eddy viscosity for turbulence that is generated in the surf zone. Approximation of Reynolds stress anisotropy allows to determine the eddy viscosity as the product of functions of velocity and of distance. According to the mixing length model, the length is specified on the basis of the geometry of the flow. This is used in a number of wave modelling tools, e.g., MIKE21 FLOW MODEL HD (product of MIKE Powered by DHI). However, in the momentum transport models, such as two equation models, e.g., $k-\varepsilon$ model, velocity and length are related to the turbulent kinetic energy as well as to the rate at which energy is dissipated. Even in relatively simple flows, the eddy viscosity concept can fail due to regions inside of which the shear stress and the velocity gradient of the flow have opposite signs (Rodi, 1980).

The paper is organized as follows. In section 2, the physical model described by Oldekop and Liiv (2013) is revisited to address the experimental observations of the breaking waves and to describe the experimental setup and measurements. In the first subsection of the methodology part, a generalized mathematical formulae are proposed to predict the instantaneous eddy viscosity coefficient according to the Reynolds stresses, mean velocity gradient components and turbulent kinetic energy, which are measured during a number of wave periods. Also, this section presents the empirical formulae extensively

used in the coastal engineering modelling. In the second subsection of the methodology, the meshless numerical model is proposed to reproduce the wave breaking process on the sloping bottom of the shortened wave flume. In the results section, a novel eddy viscosity formulation with modified mean velocity and its derivatives is presented for the case of non-isotropic turbulence. In addition, the averaged eddy viscosity values are compared with the empirical and numerical predictions. In the discussion section, the field modifications of the mean velocity and its derivatives are explained. Finally, conclusions are outlined based on the overall results.

2. PHYSICAL MODEL

Experimental studies of breaking waves with the propagation of regular waves over a uniformly sloping bottom were carried out in the wave flume with a bottom slope of a constant 1 to 17 positioned in one end (Fig. 1). Wave flume itself was 0.6 m in width, 0.6 m in depth and 22 m in length (Fig. 1). The origin of the coordinate system was taken at the still water height 0.3 m, where the inclined bottom of the flume begins (see RP, standing for reference point in Fig. 1).

Waves were created using a flap-type wave generator situated at the other end of the wave flume from the slope (Fig. 1), which enables generation of regular waves. Wave generator divided the constant depth of the water body into a regular waves area and a ballast water area. Dumping of the wave generator backside waves was established inside of the ballast water area by using four layers of metal net with size of 3 mm by 3 mm and 50 mm step in between the layers. A computer was used to produce signals for making regular sinusoidal waves controlled by the generator. Velocity profiles were measured in the breaking waves using a two component Argon-ion laser Doppler anemometer (LDA) with an output power of 1.3 W (Fig. 1). The measuring system was based on a two-dimensional tracker that operated in forward scatter fringe mode. The two velocity components were measured simultaneously. The flow velocity data were collected with a sampling frequency of 1 kHz during 151 wave periods. During the signal drop-out caused by air bubbles blocking the laser beams, the frequency tracker kept the output voltage the same as the voltage just before the drop-out. To ensure signal dropping, the drop-out signal was recorded simultaneously with the output of regular channels. The synchronizing mechanism (Fig. 1) was made by a pair of electrodes and was positioned above the still water level in the constant depth section of the flume. Capacity probes in wave gauge were used to measure variations in wave height (Fig. 1). Table 1 shows the main characteristics of the regular wave in the experimental runs.

As the LDA system allows measurements at one point, the measurements were repeated over 29 profiles along the slope. The measuring step in the vertical direction was 1 mm in the near bed zone, 3 mm

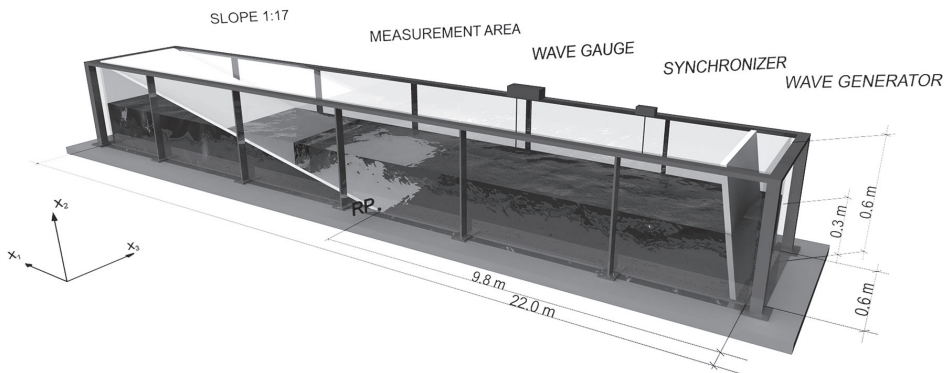


Fig. 1. Bird view of the wave flume: dimensions and notation.

Table 1. Regular wave characteristics

T , s	h_b , m	d_b , m	x_b , m	H_0 , m	L_0 , m	H_b , m	C_0 , m s ⁻²
2.03	0.106	0.111	2.90	0.072	6.0	0.118	1.72

Table 2. Location of measuring profiles and corresponding wave parameters

Profile No.	Distance from the reference point RP, m	Still water depth d , m	Water depth with wave set-up h , m	Wave celerity C , m s ⁻²
16	2.80	0.118	0.116	1.069
17	2.81	0.118	0.115	1.064
18	2.82	0.117	0.114	1.059

in the intermediate zone and 2 mm in the zone affected directly by the water surface motion. The closest measurement point to the bottom was 0.05 mm above the rigid bed of the slope. For this paper, three neighbouring profiles were chosen to analyse the velocity changes during the breaking waves. The parameters observed in the experimental runs are presented in Table 2.

During experimental runs, horizontal and vertical components, the corresponding signal drop-outs, water level variation and the signal from the synchronizing mechanism were stored. To determine ensemble averaged unsteady mean velocity and velocity fluctuation, data were collected for 151 waves.

The physical model of the wave flume and preliminary data processing of the experimental tests of breaking waves on the sloping bottom developed at Tallinn University of Technology (TalTech) is described in detail by Liiv (2007). Essentially, findings of previous investigations on the bottom boundary layer (Fredsoe, 1992) in U-shaped oscillating tunnels were compared with new experimentally observed results produced in the TalTech wave flume, and it was concluded that calculations of semi-logarithmic dimensionless velocity distributions were significantly different from those proposed previously. In addition, the two-dimensional ensemble averaged velocity components and turbulent kinetic energy fields are presented by Liiv and Lagema (2008). The study by Oldekop and Liiv (2013) found a considerable space and time variation in both bottom and wave boundary layers of the shear stress term in the surf zone. They conclude that the turbulence generated during the wave breaking has a strong effect on the shape of the shear velocity profiles. In the study by Oldekop and Liiv (2013), the measured velocity profiles before and after wave breaking are compared to demonstrate the effect of generated turbulence on the wave dynamics in the surf zone.

3. METHODOLOGY

In this section, the turbulence modelling is specified with eddy viscosity coefficients that can be explicitly or implicitly determined. In the case of the theoretical and empirical models, the eddy viscosity is determined by explicit mathematical formulae, and in the case of the numerical model, the eddy viscosity is determined by implicit numerical modelling.

3.1. Theoretical and empirical models

The Reynolds stresses can be used to determine the eddy viscosity at any point of the turbulent flow field. At each point and time, the Reynolds stress anisotropy $a_{ij} \equiv \langle u_i u_j \rangle - \frac{2}{3} k_T \delta_{ij}$, which corresponds to turbulent shear stresses, is determined by the mean velocity gradient $\nabla \langle \mathbf{U} \rangle$ components and eddy viscosity ν_T . The corresponding Reynolds stresses for a compressible fluid are

$$\begin{aligned}
 -\langle u_i u_j \rangle &= -\frac{2}{3} k_T \delta_{ij} + \nu_T \left(\frac{\partial \langle U_i \rangle}{\partial x_j} + \frac{\partial \langle U_j \rangle}{\partial x_i} - \frac{2}{3} \frac{\partial \langle U_k \rangle}{\partial x_k} \delta_{ij} \right) = \\
 &= -\frac{2}{3} \left(k_T + \nu_T \frac{\partial \langle U_k \rangle}{\partial x_k} \right) \delta_{ij} + \nu_T \left(\frac{\partial \langle U_i \rangle}{\partial x_j} + \frac{\partial \langle U_j \rangle}{\partial x_i} \right), \tag{1}
 \end{aligned}$$

where k_T is the turbulent kinetic energy, δ_{ij} is the Kronecker delta and ν_T is the eddy viscosity. Reynolds stress is proportional to the mean rate of the compression and shear strain, where the positive scalar coefficient ν_T is the eddy viscosity. It is only the anisotropic component a_{ij} that is effective in transporting momentum, while the isotropic component $\frac{2}{3}k_T$ can be absorbed in a modified mean pressure. The total viscous stresses are given by augmenting the molecular viscosity with an eddy viscosity (see Bertin et al., 1992).

For the turbulent channel flows, symmetries in the flow geometry determine the properties of the Reynolds stresses. Considering a statistically two-dimensional flow in which statistics are independent of the cross-channel coordinate x_3 (see Fig. 1), the Reynolds stress tensor for a turbulent flow in the flume may be approximated as

$$\langle u_i u_j \rangle = \begin{bmatrix} \langle u_1^2 \rangle & \langle u_1 u_2 \rangle & 0 \\ \langle u_1 u_2 \rangle & \langle u_2^2 \rangle & 0 \\ 0 & 0 & \langle u_3^2 \rangle \end{bmatrix}, \tag{2}$$

which applies to the turbulent channel flow with an inclined bottom, i.e., with a slope in along-channel coordinate x_1 direction and vertical x_2 direction.

In a two-dimensional turbulent oscillatory flow, the instantaneous local velocity components (U_1 for the horizontal component, U_2 for the vertical component) may be decomposed into phase ensemble components ($\langle U_1 \rangle, \langle U_2 \rangle$) and turbulent components ($\langle u_1 \rangle, \langle u_2 \rangle$), e.g. $\vec{U} = \langle \vec{U} \rangle + \langle \vec{u} \rangle$. The vertically averaged (over three measurement points) variables are functions of time and distance, e.g.,

$$\langle U_i \rangle = \frac{1}{\Delta x_j} \int_{x_j}^{x_j + \Delta x_j} U_i dx_j. \tag{3}$$

Making use of the Reynolds stress anisotropy, Eq. (1) can be applied to derive a formula for the eddy viscosity coefficient that results from the non-diagonal elements, which in the present case takes the form

$$\nu_T = \frac{-\langle u_1 u_2 \rangle}{\frac{\partial \langle U_1 \rangle}{\partial x_2} + \frac{\partial \langle U_2 \rangle}{\partial x_1}}, \tag{4}$$

and from the diagonal elements, which in the present case takes the form

$$\nu_T = \frac{\frac{2}{3} k_T - \langle u_i u_i \rangle}{2 \frac{\partial \langle U_i \rangle}{\partial x_i} - \frac{2}{3} \left(\frac{\partial \langle U_1 \rangle}{\partial x_1} + \frac{\partial \langle U_2 \rangle}{\partial x_2} \right)}. \tag{5}$$

The turbulent kinetic energy $k_T = \frac{1}{2} (\langle u_1^2 \rangle + \langle u_2^2 \rangle + \langle u_3^2 \rangle)$ is approximated for the two-dimensional turbulent oscillatory flow as

$$k_T \approx \frac{1}{2}(\langle u_1^2 \rangle + \langle u_2^2 \rangle), \quad (6)$$

where the turbulent kinetic energy calculation is simplified due to conditions $\langle u_1 \rangle > \langle u_2 \rangle \gg \langle u_3 \rangle$.

Turbulent viscosity $\nu_T(x, t)$, can be expressed empirically as the product of a shear velocity $U^*(x, t)$ and a length scale $l^*(x, t)$:

$$\nu_T = U^* l^*. \quad (7)$$

Considering the mixing length model, l^* for Eq. (7) is specified on the basis of the geometry of the flow. In engineering-type modelling, eddy viscosity is usually specified in one of the four different ways: a) by omitting eddy terms; b) by giving constant value for each area; c) by a data file where each grid point has its defined value, or d) by dynamic calculations using Smagorinsky formula. Based on the second option (b), a uniform eddy term is chosen based on:

$$\nu_T = 0.02 \frac{\Delta x_1 \Delta x_2}{\Delta t}, \quad (8)$$

where $\Delta x_1 \Delta x_2$ is the grid spacing $90 \times 3 \text{ mm}^2$ and Δt is the time step 1/1000 s.

However, calculations based on the fourth option (d), the Smagorinsky formula

$$\nu_T = C_S^2 \Delta x_1 \Delta x_2 \sqrt{\left(\frac{\partial \langle U_i \rangle}{\partial x_i}\right)^2 + \frac{1}{2} \left(\frac{\partial \langle U_i \rangle}{\partial x_j} + \frac{\partial \langle U_j \rangle}{\partial x_i}\right)^2 + \left(\frac{\partial \langle U_j \rangle}{\partial x_j}\right)^2}, \quad (9)$$

where C_S is a constant to be chosen in the interval of 0.25–1.0 (Canuto and Cheng, 1997).

Some stability issues can arise when using the velocities from the previous time step and the eddy viscosity coefficient becomes large. So, the coefficient must fulfill the criterion

$$\frac{\nu_T \Delta t}{\Delta x_1 \Delta x_2} \leq \frac{1}{2}. \quad (10)$$

In two-equation models, U^* and l^* for Eq. (7) are related to transport equations, like the most widely used $k - \varepsilon$ turbulence closures model suggested by Launder and Sharma (1974):

$$\nu_T = C_\mu \frac{k_T^2}{\varepsilon}, \quad (11)$$

where $C_\mu = 0.09$ is known as the constant of proportionality, defined empirically through consideration of the flow under local equilibrium conditions, which states that at high Reynolds number, the rates of production and dissipation are of similar order of magnitude. Turbulent kinetic energy k_T is taken according to Eq. (6) and turbulence dissipation rate:

$$\varepsilon = \frac{C_\mu^{3/4} k_T^{3/2}}{L}, \quad (12)$$

where L is the turbulence length scale. Then turbulent kinetic energy and turbulence dissipation rate, eddy viscosity can be determined by the one equation turbulence model.

3.2. Numerical model

In the present study, the turbulence in the wave breaking process is treated by using artificial viscosity and interpolating kernel (Violeau and Rogers, 2016) and an empirical equation of compressibility by Batchelor (1967). Under these empirical considerations and some modification of the numerical model of empirical constants, the computational stability can be established with a reasonably small artificial viscosity coefficient α (see Eq. (13)). Interaction between the particles on the boundary is described by the Lennard-Jones potential and fluid particle trajectories are determined using the Verlet method for 2D motion. According to De Padova et al. (2009), in the limits where the kernel smoothing length and the interparticle spacing become small, the kernel is assumed to have compact support and to some extent, there seems to be no difference which kernel is used as long as basic requirements are met. However, in practice, values are not small and choice of kernel can drastically change the computational results (Rosswog, 2015). The fundamentals of the modified SPH method for free surface motion were described by Monaghan (1992, 1994, 2000).

In the SPH model, the artificial viscosity for a fluid is defined as

$$\nu_{A,ij} = \frac{-\alpha\mu_{ij}\bar{c}_{ij}}{\bar{\rho}_{ij}}, \quad (13)$$

where the following velocity dependent variable is

$$\mu_{ij} = \frac{h(\mathbf{V}_i - \mathbf{V}_j) \cdot (\mathbf{x}_i - \mathbf{x}_j)}{(\mathbf{x}_i - \mathbf{x}_j)^2 + (0.01h^2)}. \quad (14)$$

The overbar is an averaging operator, i.e., $\bar{\rho}_{ij} = \frac{1}{2}(\rho_i + \rho_j)$ and ρ_i and ρ_j are the density at particles i and j , respectively; $\bar{c}_{ij} = \frac{1}{2}(c_i + c_j)$ and c_i and c_j are the sound speed at particles i and j , respectively; $h = 1.2\Delta x$ is the smoothing length, where $\Delta x (= \Delta x_1 = \Delta x_2)$ is the space step and α is a constant that depends on the particular type of simulation being run and requires careful numerical calibration.

The SPH eddy viscosity at a fixed point $i = a$ is determined as

$$\nu_{SPH} = \frac{-\alpha c \sum_j \mu_j W_{aj}}{\sum_j \rho_j W_{aj}}, \quad (15)$$

where averaged viscosity at a fixed point is $\mu_{average} = \sum_j \mu_j W_{aj}$ and averaged density of mass at a fixed point is $\rho_{average} = \sum_j \rho_j W_{aj}$. The density of each particle is $\rho_i = \sum_j m_j W_{ij}$, where the particle j mass is m_j and the interpolation kernel is W_{ij} .

4. RESULTS

The experimental and numerical results correspond to the wave and bottom boundary layer conditions. In the first subsection, the eddy viscosity is specified according to the modified mean velocity and its derivatives. In the second subsection, the artificial viscosity is determined by numerical modelling. In the last subsection, the experimentally evaluated theoretical and empirical formulae of eddy viscosity and the numerically determined eddy viscosity values are compared.

4.1. Experimental results' treatment

It should be pointed out that the assumption of a purely shear straining velocity field in the bottom and surface boundary layers, which allows use of Eq. (4), is not valid for all instants and flow areas in the shoaling region, where the flow results from the superposition of the incoming waves, surface breaking and reflected wave. In the Boussinesq-type models for surface waves, the flow is represented through a decomposition of the velocity into a potential and a rotational part (see Briganti et al., 2004). The direct ensemble averaged measured velocity solutions confirm that both, eddy viscosity formulae Eq. (4) and Eq. (5) can result in peaks and negative values. This is apparently due to the velocity corresponding to a potential part where its gradient components do not represent the shear straining. Thus, an irrotational flow may be removed from the measured velocity by specifically treating the mean velocity and its derivatives. The velocity corresponding to a rotational part may be gained by subtracting the velocity just outside the bottom boundary layer from the local velocity: $\langle \vec{U} \rangle_t = \langle \vec{U} \rangle - \langle \vec{U} \rangle_b$. Furthermore, mean velocity gradient components should be modified by the functions that depend on the distance above the bottom:

$$\begin{aligned} \left(\frac{\partial \langle U_1 \rangle}{\partial x_1} \right)_t &= \frac{\partial \langle U_1 \rangle}{\partial x_1} - A(x_2), & \left(\frac{\partial \langle U_2 \rangle}{\partial x_2} \right)_t &= \frac{\partial \langle U_2 \rangle}{\partial x_2} - B(x_2), & \left(\frac{\partial \langle U_1 \rangle}{\partial x_2} \right)_t &= \frac{\partial \langle U_1 \rangle}{\partial x_2} - C(x_2), \\ \left(\frac{\partial \langle U_2 \rangle}{\partial x_1} \right)_t &= \frac{\partial \langle U_2 \rangle}{\partial x_1} - D(x_2). \end{aligned}$$

The weak compressibility of the fluid considered in Eq. (5) is based on the experimental observations showing that on the wave motion in the surf zone, a substantial amount of air is mixed into the water due to the surface breaking. It should be noted that for a two-dimensional flow, which corresponds to the experimental results, the non-zero divergence of the mean velocity is found, i.e.

$\frac{\partial \langle U_1 \rangle}{\partial x_1} + \frac{\partial \langle U_2 \rangle}{\partial x_2} \neq 0$, and a vertical velocity gradient component is negligible, i.e. $\frac{\partial \langle U_3 \rangle}{\partial x_3} \approx 0$, and can be ignored in Eq. (5).

4.2. Numerical model set-up

Numerical experiments were performed with the modified SPH model to simulate the wave breaking on the sloping bottom. Several modifications were introduced to the model setup. The numerical model domain was divided into two sections: 1) sloping bottom part and 2) horizontal bottom part. The sloping bottom 1:17 section was considered to be the same as in the physical model. The horizontal bottom between the reference point and the wave generator (Fig. 1) is considerably shortened. The reason is that a reduced number of particles per fluid volume allows speed-up of the numerical integration. The additional vertical extension in the sloping bottom end of the wave flume was used to keep the number of particles constant. However, to avoid particles' loss due to overtopping from 2D geometrical boundaries, the special criterion in the open-code SPH model was included to detect particles overtopped and move them back to the computational domain.

The wave generator used in the numerical model produced free surface crests motion. This motion becomes apparent in the wave flume after vanishing of the system self-oscillations. The length of the surface waves is around 4 m and directly observed phase speed in the horizontal bottom part of the numerical model domain is approximately 1.75 m s^{-1} (cf. experimentally observed wave celerity in Table 1). It is assumed that the speed of sound in Eq. (13) is constant, i.e. $\bar{c}_{ij} = 1440 \text{ m s}^{-1}$. The wave absorbing in the sloping bottom has a frequency of 0.5 Hz. The different phases, i.e. forward and backward position of the fluttering plate of the flap-type generator in the surface wave production, are shown in Figs 2a and 2b, respectively. In the wave generator mode, the breaking of particles formed free surface is in clear evidence. Regardless of a comparatively small number of particles, the wave production in the horizontal bottom and wave breaking along the sloping bottom is qualitatively in a good agreement with the experimental observations of the surface boundary layer.

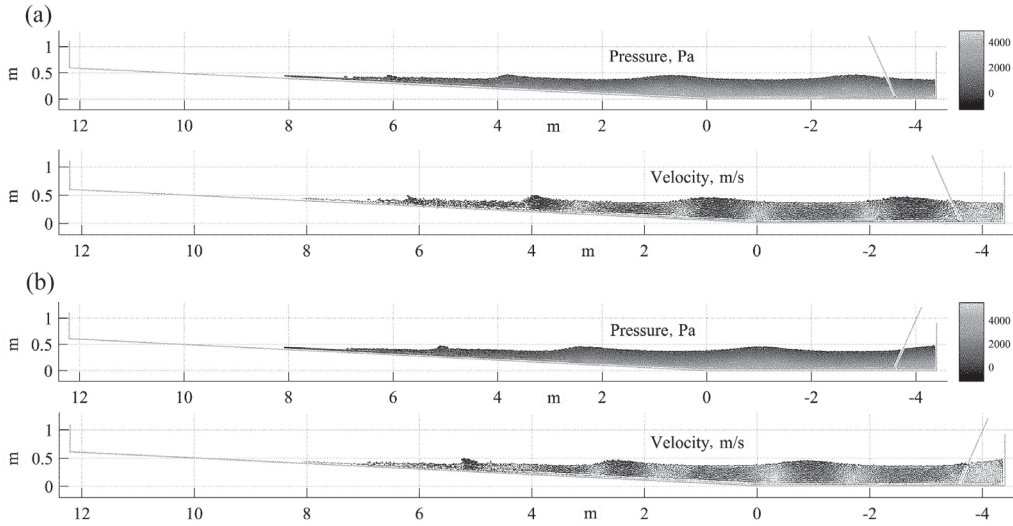


Fig. 2. SPH simulations of surface waves using an oscillating plate in: a) upper sub-plot shows the pressure and lower sub-plot shows the velocity at the time instant after 106.5 s; b) upper sub-plot shows the pressure and lower sub-plot shows the velocity at the time instant after 107.5 s.

In our implementation, the parallel computations were not used and therefore 1 s of simulation (consisting 1500 calculation steps) took around 25 min of real time in the used laptop with Intel® Core™ i7-8650U Processor. The structure of the SPH method is very suitable for parallelizing the computational process between the cores, on a cluster of computers or on a GPU (Ihmsen et al., 2011).

4.3. Comparison of experimental and numerical findings

Wave patterns are characterized by mean free surface displacement within the wave period (Fig. 3) along the chosen profiles (see Table 2), normalized by the local time average water depth. According to Fig. 3, wave breaking appears from 0.7–0.9 of the dimensionless wave period. Profile 16 is positioned in deeper water as compared to the position of profile 17, which is positioned in deeper water than the position of profile 18 on the slope.

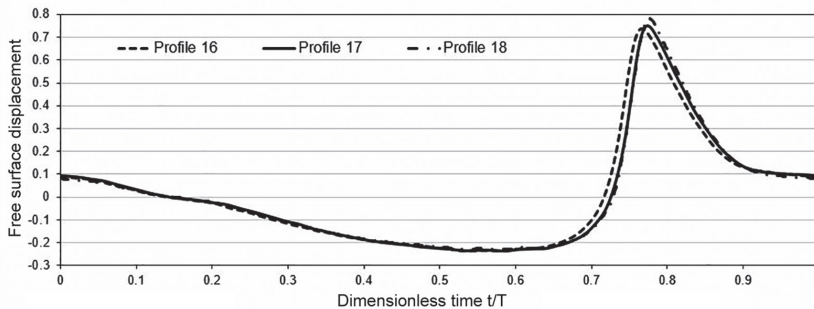


Fig. 3. The mean free surface displacement for three profiles. The profile numbers correspond to the location of measuring profiles 16, 17 and 18 in Table 2.

Measured turbulent kinetic energy according to Eq. (6) (see Fig. 4) was calculated at five different heights at one profile: a) 0.067 m; b) 0.052 m; c) 0.040 m; d) 0.028 m; and e) 0.006 m on sloping bottom. Turbulent kinetic energy demonstrates two local maximums: at instants when the surface roller is passing measurement profile 17, i.e. dimensionless wave period 0.65–0.75, and directly after the wave crest, i.e. dimensionless wave period 0.80–0.85. After breaking of a wave, there is a local minimum in the turbulent kinetic energy value occurring during a dimensionless wave period 0.00–0.10, which then converges to more or less constant value during a dimensionless wave period 0.10–0.60. It can be seen that the turbulent kinetic energy varies almost linearly with the increasing height from the bed.

The eddy viscosity was determined at the height of 0.028 m above bottom. Using the modified velocity gradient components, the solution resulting from the non-diagonal elements from the Reynolds stress tensor in Eq. (4) is shown by a dash-dot curve in Fig. 5. It can be seen that the eddy viscosity shows one distinct local maximum at instants when the surface roller is passing measurement profile 17, occurring at the dimensionless wave period 0.80. Eddy viscosity based on the first and second diagonal elements from the Reynolds stress tensor in Eq. (5) is shown as curves with shorter and longer dashed, respectively in Fig. 5. As can be seen, eddy viscosity shows two local maximums, similar to the turbulent kinetic energy in Fig. 4. However, the second diagonal elements correspond to significantly lower values. Also, Fig. 5 shows averaged eddy viscosity values, derived from the results of Eq. (4) and Eq. (5) (shown as a continuous curve).

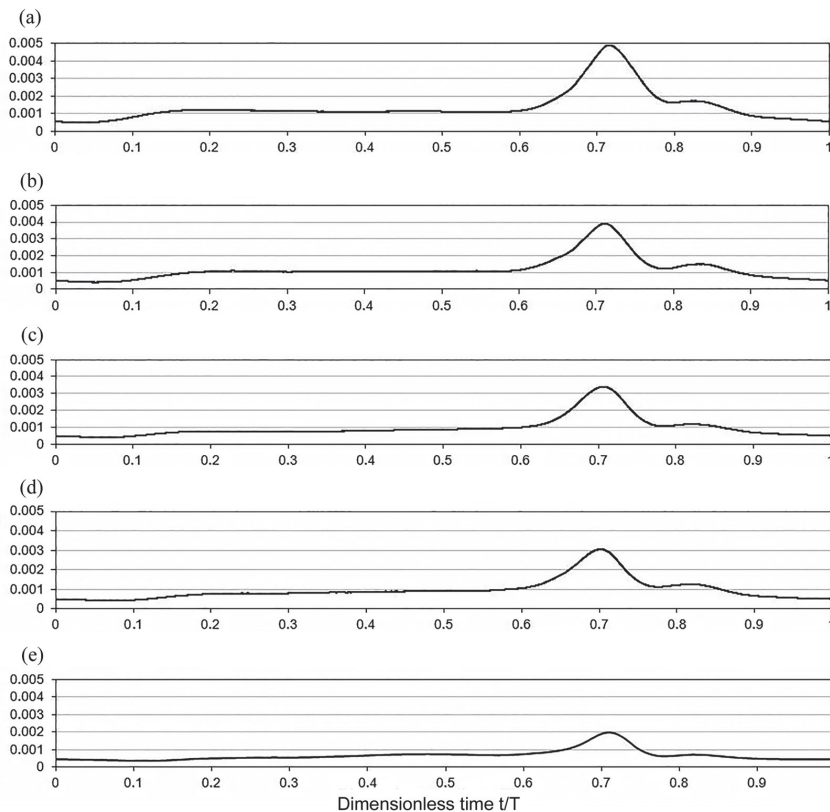


Fig. 4. Measured turbulent kinetic energy at different heights above sloping bottom: a) 0.067 m; b) 0.052 m; c) 0.040 m; d) 0.028 m and e) 0.006 m.

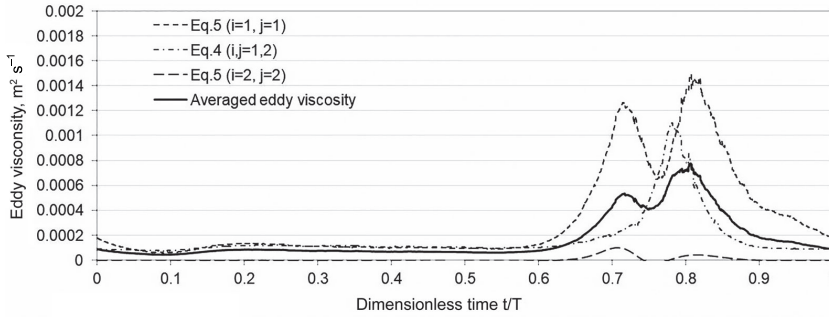


Fig. 5. Eddy viscosity based on theoretical equations with the surface direction index i and the flow direction index j . The averaged eddy viscosity values, derived from the results of Eq. (4) and Eq. (5), are shown as a continuous curve.

The averaged eddy viscosity presented in Fig. 5 is compared with the empirical and numerical modelling results in Fig. 6. The figure shows that the first local maximum of the averaged eddy viscosity corresponds to the $k - \epsilon$ model eddy viscosity predictions by Eq. (11) (short dashed curve in Fig. 5), i.e. it occurs during the dimensionless wave period 0.65–0.75. Further, the second local maximum of the averaged eddy viscosity corresponds to the Smagorinsky model eddy viscosity mixing length model, Eq. (9) (dash-dot curve in Fig. 6), it occurs during the dimensionless wave period 0.75–0.85. However, neither of the local maximums of the empirical models is in full correlation with the averaged eddy viscosity maximum. Furthermore, empirical models have lower values during the entire wave period than the averaged eddy viscosity. Inside the wave trough, all three eddy viscosities show more or less constant values. However, the eddy viscosity values of the Smagorinsky model correspond better to the averaged eddy viscosity, and the $k - \epsilon$ model eddy viscosity shows twice higher values.

Uniform eddy viscosity based on the mixing length model in Eq. (8) (long dashed curve in Fig. 6) shows a constant value of $5.4 \times 10^{-4} \text{ m}^2 \text{ s}^{-1}$. This value is higher than most of previous eddy viscosity results, except on averaged eddy viscosity second local maximum.

According to the numerically determined SPH eddy viscosity in Eq. (15) (dotted curve in Fig. 6), its local maximum is directly under the surface roller. However, within an entire wave period, SPH eddy viscosity gives higher values than the uniform eddy viscosity.

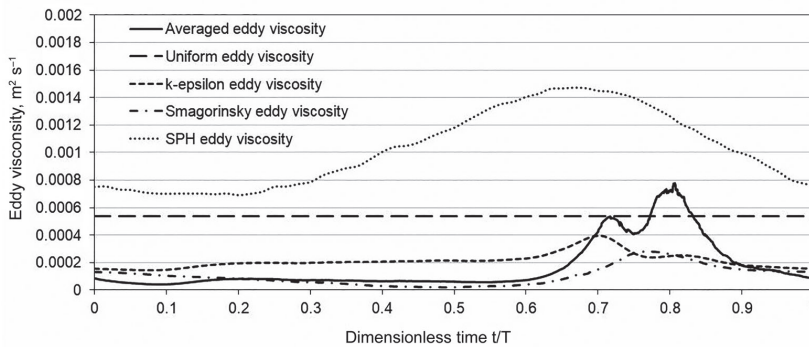


Fig. 6. Eddy viscosity estimates from different approximations: theoretical (averaged eddy viscosity in Fig. 5), empirical (uniform, $k - \epsilon$ and Smagorinsky eddy viscosity) and numerical (SPH eddy viscosity) predictions.

5. DISCUSSION

The eddy viscosity values were estimated according to formulae Eq. (4) and Eq. (5), which represent certain relationships between the velocity fluctuations correlation coefficients, turbulence kinetic energy and mean velocity gradient components. It was found that the ensemble averaged measured velocity predicted eddy viscosity is associated with peaks and negative values (see Oldekop et al., 2015), which are absent in the broadly accepted empirical predictions. Spurious peaks and negative values are apparently related to the velocity corresponding to a potential part of the flow where its gradient components do not represent the shear straining and manifest themselves when the shear stress and the velocity gradient change signs, i.e. flow reversal. This phenomenon has been reported by Perrier et al. (1995), Davies and Villaret (1999) and Malarkey and Davies (2004). We followed the methodology proposed by Briganti et al. (2004), where the flow is represented through a decomposition of the velocity into a potential and a rotational part. A possible alternative to solve the eddy viscosity problem was suggested by Shih et al. (1996), which was based on the relation between the Reynolds stress tensor and the strain rate of the mean flow through the nonlinear Reynolds stress model.

In this paper, the approach presented by Briganti et al. (2004), was tested by using the formulae Eq. (4) and Eq. (5), where the mean velocity and its derivatives were specifically treated. The irrotational flow was removed from the measured velocity by removing the oscillating part of the flow from the mean velocity and modifying its derivatives fields by the depth-dependent and time independent constants. The velocity corresponding to a rotational part was obtained by subtracting the velocity just outside the bottom boundary layer from the local velocity, and the mean velocity gradient components were modified by functions $A(x_2)$, $B(x_2)$, $C(x_2)$, $D(x_2)$, which depend on the distance from the bottom. Apparently, this specific treatment of the mean velocity and its derivatives is a possible source of some errors, which is not important in respect of qualitative results. In our approach, the used functions follow some conditions, i.e. $A(x_2) \ll B(x_2)$ and $C(x_2) = D(x_2)$. The latter indicates that the specific correction functions correspond to the irrotational flow of the velocity field. In other words, according to the approach by Briganti et al. (2004), the rotational velocity can be expressed as

$$\overrightarrow{\langle U \rangle}_p = \overrightarrow{\langle U \rangle}_b + a x_2 \hat{a} + b x_2^2 \hat{b}, \quad (16)$$

where coefficients $a = f_a(A, B, C, D)$, $b = f_b(A, B, C, D)$ and unit vectors are \hat{a} and \hat{b} .

In the surf zone, the surface wave undergoes changes due to the velocity shear near bottom and free surface non-linear deformation, the turbulence is generated from two sources: bottom boundary layer and surface boundary layer. Also, the present study takes into account that the eddy viscosity is not related to the tube flow oscillation approximation, where it is sufficient to use the relationship between the correlation coefficient of cross flow directional fluctuations and the vertical component of the along channel velocity gradient. Furthermore, a substantial amount of air that is captured within the wave motion due to breaking, results in the non-zero divergence of the mean velocity. This indicates that the air mixing in the water of the plunging breaker corresponds to a weakly compressible fluid.

Considering variations in the turbulent kinetic energy values during the wave period and over the water column, it is apparent from Eq. (5) that the eddy viscosity values are also changing over time and space. Regarding the new experimental findings, it could be suggested that using the coastal engineering models, the empirical and numerical predictions should follow the theoretical eddy viscosity time and space dependent functions in the surf zone. It should be taken into account that the turbulence is generated both in the surface and bottom boundary layers, which merge in the surf zone. Therefore, empirical predictions are unable to forecast the eddy viscosity values during the wave period and over the water column with acceptable accuracy.

6. CONCLUSIONS

To clarify the complex turbulence dynamics of breaking waves in the surf zone, this study revisited a data set derived from a relevant experiment. The empirical and numerical predictions of eddy viscosity were

compared to the experimental findings obtained from the physical beach model presented by Liiv (2007). The theoretically predicted eddy viscosity was derived from the combined functions of Reynolds stresses, modified mean velocity and its gradient components and from turbulent kinetic energy for weakly compressible fluid. The irrotational flow that masked the turbulence velocity field under a breaking wave was removed by means of oscillating velocity at bottom and four coefficients were used to modify the particular mean velocity gradient components. The instantaneous eddy viscosity coefficient is positively valued during the wave period, which gives evidence of the modified velocity field corresponding well to the shear and compression strain that results from the bottom and surface boundary layers. It was found that the eddy viscosity determined experimentally is of high complexity under a breaking wave on the sloping bottom than predictions of the empirical formulae. Also, it is required to improve the meshless numerical modelling to determine the artificial viscosity and the corresponding eddy viscosity more accurately by a number of particles “smeared” in space. It is demonstrated that the theoretically determined eddy viscosity values are in the same order of magnitude as the empirical and numerical predictions, and follow reasonably well the production of turbulence during wave breaking.

It was found that the SPH eddy viscosity corresponds qualitatively well with the theoretical eddy viscosity determined from the combined functions of Reynolds stresses modified mean velocity and its gradient components and turbulent kinetic energy for compressible fluid. As a possible future task, SPH modelling approach should be used more comprehensively in dealing with the counterparts of coastal processes, e.g., stratified flow mixing, air-water interaction and sediments transport in the surf zone due to wave breaking. In the complex coastal environment, where waves and currents interact with bed forms, the stratified flow and wind wave numerical models should be used to predict bottom changes (cf. Laanearu et al., 2011).

ACKNOWLEDGEMENTS

The SPH model used herein was developed by the master-level student Gleb Bogomol during the special course of fluid dynamics at Tallinn University of Technology. This work was partly supported by the Estonian Ministry of Education and Research [grant IUT 19-17]. The publication costs of this article were covered by the Estonian Academy of Sciences.

REFERENCES

- Batchelor, G. K. 1967. *An Introduction to fluid dynamics*. Cambridge University Press, Cambridge, United Kingdom.
- Battjes, J. A. 1988. Surf-zone dynamics. *Annu. Rev. Fluid Mech.*, **20**, 257–291.
- Bertin, J. J., Periaux, J., and Ballmann, J. 1992. *Advances in Hypersonics. Modeling Hypersonic Flows. – Volume 2*. Birkhäuser, Boston, USA.
- Briganti, R., Musumeci, R. E., Bellotti, G., Brocchini, M., and Foti, E. 2004. Boussinesq modeling of breaking waves: description of turbulence. *J. Geophys. Res.*, **109**(C0701).
- Canuto, V. M. and Cheng, Y. 1997. Determination of the Smagorinsky-Lilly constant CS. *Phys. Fluids*, **9**, 1368.
- Capone, T., Panizzo, A., and Monaghan, J. J. 2010. SPH modelling of water waves generated by submarine landslides. *J. Hydraul. Res.*, **48**, 80–84.
- Chang, K.-A. and Liu, P. L.-F. 1999. Experimental investigation of turbulence generated by breaking waves in water of intermediate depth. *Phys. Fluids*, **11**, 3339–3400.
- Dalrymple, R. A. and Rogers, B. D. 2006. Numerical modelling of water waves with the SPH method. *Coastal Eng.*, **53**, 141–147.
- Davies, A. G. and Villaret, C. 1999. Eulerian drift induced by progressive waves above rippled and very rough beds. *J. Geophys. Res.*, **104**(C1), 1465–1488.
- De Padova, D., Dalrymple, R. A., Mossa, M., and Petrillo, A. F. 2009. SPH simulations of regular and irregular waves and their comparison with experimental data. *arXiv:0911.1872v1*
- Fredsoe, J. and Deigaard, R. 1992. *Mechanics of coastal sediment transport. Advanced Series on Ocean Engineering – Volume 3*. World Scientific Publishing, Singapore.
- Gomez-Gesteira, M., Rogers, B. D., Dalrymple, R. A., and Crespo, A. J. C. 2010. State-of-the-art of classical SPH for free-surface flows. *J. Hydraul. Res.*, **48**, 6–27.
- Ihmsen, M., Akinci, N., Becker, M., and Teschner, M. 2011. A parallel SPH implementation on multi-core CPUs. *Comput. Graphics Forum*, **30**(1), 99–112.
- Laanearu, J., Koppel, T., Soomere, T., and Davies, P. A. 2007. Joint influence of river stream, water level and wind waves on the height of sand bar in a river mouth. *Nord. Hydrol.*, **38**(3), 287–302.

- Laanearu, J., Vassiljev, A., and Davies, P. A. 2011. Hydraulic modelling of stratified bi-directional flow in a river mouth. In *Proceedings of the Institution of Civil Engineers: Engineering and Computational Mechanics*, **164**(4), 207–216.
- Lauder, B. E. and Sharma, B. I. 1974. Application of the energy-dissipation model of turbulence to the calculation of flow near a spinning disc. *Lett. Heat Mass Transfer*, **1**(2), 131–138.
- Lee, E. S., Violeau, D., Issa, R., and Ploix, S. 2010. Application of weakly compressible and truly incompressible SPH to 3-D water collapse in waterworks. *J. Hydraul. Res.*, **48**, 50–60.
- Liiv, T. 2007. An experimental investigation of the oscillatory boundary layer around the breaking point. *Proc. Est. Acad. Sci.*, **13**(3), 215–233.
- Liiv, T. and Lagema, P. 2008. The variation of the velocity and turbulent kinetic energy field in the wave in the vicinity of the breaking point. *Est. J. Eng.*, **14**(1), 42–64.
- Lundgren, H. and Sorensen, T. 1958. A pulsating water tunnel. In *Proceedings 6th Coastal Engineering Conference, ASCE*, 356–358.
- Madsen, O. S. and Grant, W. D. 1976. Quantitative description of sediment transport by waves. *Coastal Eng. Proc.*, **1**(15), 1093–1112.
- Malarkey, J. and Davies, A. G. 2004. An eddy viscosity formulation for oscillatory flow over vortex ripples. *J. Geophys. Res.*, **109**, C12016.
- Monaghan, J. J. 1992. Smoothed particle hydrodynamics. *Annu. Rev. Astron. Astrophys.*, **30**, 543–574.
- Monaghan, J. J. 1994. Simulating free surface flows with SPH. *J. Comput. Phys.*, **110**, 399–406.
- Monaghan, J. J. 2000. SPH without a Tensile Instability. *J. Comput. Phys.*, **159**, 290–311.
- Morris, J. P. 2000. Simulating surface tension with smoothed particle hydrodynamics. *Int. J. Numer. Methods Fluids*, **33**(3), 333–353.
- Oldekop, N. and Liiv, T. 2013. Measurement of the variation of shear velocity on bed during a wave cycle. *J. Earth Sci. Eng.*, **3**(5), 322–330.
- Oldekop, N., Liiv, T., and Lagema, P. 2015. The variation of turbulent eddy viscosity during a wave cycle. *E-Proceedings of the 36th IAHR World Congress, June 28–July 3, 2015, Hague, Netherlands*, 1–5.
- Peregrine, D. H. 1983. Breaking waves on beaches. *Annu. Rev. Fluid Mech.*, **15**, 149–178.
- Perrier, G., Villaret, C., Davies, A. G., and Hansen, E. A. 1995. Numerical modelling of the oscillatory boundary layer over ripples. *MAST G8-M Coastal Morphodynamics Project, Final Overall Meeting, Delft Hydraul., Gdansk, Poland*, 4.26–4.29.
- Rodi, W. 1980. *Turbulence models and their application in hydraulics – A state of the art review*. International Association for Hydraulic Research, Delft.
- Rogers, B. D., Dalrymple, R. A., and Stansby, P. K. 2010. Simulation of caisson breakwater movement using SPH. *J. Hydraul. Res.*, **48**, 135–141.
- Rosswog, S. 2015. SPH methods in the modelling of compact objects. *Living Rev. Comput. Astrophys.*, **1**(1).
- Shao, S. 2006. Simulation of breaking wave by SPH method coupled with $k-\epsilon$ model. *J. Hydraul. Res.*, **44**(3), 338–349.
- Shih, T.-H., Zhu, J., and Lumley, J. L. 1996. Calculation of wall-bounded complex flows and free shear flows. *Int. J. Numer. Methods Fluids*, **23**, 1133–1144.
- Svendsen, I. A. and Putrevu, V. 1996. Surf-zone hydrodynamics. *Adv. Coastal Ocean Eng.*, **2**, 1–78.
- Ting, F. C. K. and Kirby, J. T. 1994. Observation of undertow and turbulence in a laboratory surf zone. *Coastal Eng.*, **24**, 51–80.
- Ting, F. C. K. and Kirby, J. T. 1995. Dynamics of surf-zone turbulence in a strong plunging breaker. *Coastal Eng.*, **24**, 177–204.
- Ting, F. C. K. and Kirby, J. T. 1996. Dynamics of surf-zone turbulence in a spilling breaker. *Coastal Eng.*, **27**, 131–160.
- Violeau, D. and Rogers, B. D. 2016. Smoothed particle hydrodynamics (SPH) for free-surface flows: past, present and future. *J. Hydraul. Res.*, **54**(1), 1–26.

Turbulentse viskoossuse katseline uurimine lainerenni kaldpinnal murdlaine all ja võrdlused empiiriliste ning numbriliste arvutustulemustega

Nelly Oldekop, Toomas Liiv ja Janek Laanearu

On selgitatud turbulentsi parameetrite määramist sukelduva murdlaine all. Kiirusväli on mõõdetud lainerenni kaldpinnalisel põhjal Doppleri laseranemomeetriga. Kasutades Reynoldsi pinge anisotroopsust kokkusurumatu vedeliku jaoks, on leitud, et ansamblikeskmestatud mõõdetud kiirusega määratud turbulentse viskoossuse on seotud singulaarsustega, mis ei esine laialdaselt kasutatavate empiiriliste valemite arvutustulemustes. Seetõttu määratakse hetkeline turbulentse viskoossustegur Reynoldsi pingete, matemaatilisel täiendatud keskmise kiiruse ja selle gradientkomponentide ning turbulentse kineetilise energia järgi. Modifitseeritud keskmine kiirus ja selle tuletised parandavad oluliselt turbulentse viskoossusteguri arväärtusi laineperioodi jooksul, millest võib järeldada, et matemaatilisel muudetud kiirusväli vastab hästi pöörisele keerisvälja tingimustele. Mõõtmistega saadud turbulentse viskoossusteguri arväärtusi on võrreldud ka olemasolevate empiiriliste valemite arvutustulemustega, et näidata erinevate meetoditega saadud turbulentsete viskoossustegurite väärtusi laineperioodi jooksul. Närgalt kokkusurutava vedeliku hüdrodroomaanka numbrilist mudelit SPH on kasutatud kunstliku viskoossuse määramiseks laineperioodi jooksul. SPH turbulentse viskoossusteguri arväärtusi on samuti võrreldud mõõtmistel saadud turbulentse viskoossusteguri arvutustulemustega.

Publication IV

Oldekop, N., Laanearu, J. & Liiv, T. (2019). The streamline curvature dependent eddy viscosity for a plunging breaker. *Submitted to Journal of Hydraulic Research*

The streamline curvature dependent eddy viscosity for a plunging breaker

NELLY OLDEKOP (IAHR member), PhD Student, *Department of Civil Engineering and Architecture, School of Engineering, Tallinn University of Technology, Tallinn, Estonia*

Email: nelly@corson.ee (corresponding author)

JANEK LAANEARU (IAHR member), Associated Professor, *Department of Civil Engineering and Architecture, School of Engineering, Tallinn University of Technology, Tallinn, Estonia*

Email: janek.laanearu@taltech.ee

TOOMAS LIIV, Chartered Civil Engineer of Waterfront Structures, *Corson LLC, Tallinn, Estonia*

Email: toomas@corson.ee

ABSTRACT

In addition to the simple shear flow and the fluid compressibility (see Oldekop et al. 2019), in this study, the longitudinal accelerations are considered when relating the Reynolds stresses to the strain rates. The eddy viscosity was calculated based on the experimental results for a plunging breaker wave. The Reynolds stresses, modified mean velocity, its gradient components and turbulent kinetic energy were determined from the velocity measurements. It was found that the eddy viscosity coefficient under a plunging breaker wave on a sloping bottom varies during the wave period and over the water depth. It is shown that the eddy viscosity generated in the surface roller hitting the surface affects mostly middle depths, while the surface roller passing affects mostly the bottom region and the wave crest passing affects both the surface and the bottom region. It is demonstrated that the largest maximum of eddy viscosity does not appear in compliance with the largest maximum of turbulent kinetic energy. Therefore, the bulk compression and extension rates induced by the streamline curvature are also used to determine the eddy viscosity.

Keywords: Eddy viscosity; Experimental study; Open channel flow; Turbulent flow; Wave breaking

1 Introduction

The bottom and surface boundary layers of breaking waves in the surf zone are treated in very different ways in the coastal engineering models. The turbulence is generated both in the surface and bottom boundary layers, which merge in the surf zone. It was found by Oldekop et al. (2015) that the ensemble averaged measured

velocity predicts eddy viscosity with peaks and negative values, which are absent in the broadly accepted empirical predictions. Such peaks associated with negative values are apparently related to the velocity components representing the wave-type motion where flow gradient components do not represent the shear straining and manifest themselves when the shear stress and the velocity gradient change signs, i.e., flow reversal.

Turbulence progresses because of instability of a vortical flow; turbulence injection can only be simplified once the mechanisms for vorticity production in a wave are known. This can be done through handling turbulent stresses by means of the Boussinesq eddy viscosity assumption. However, removing the premise of an irrotational flow and regarding the production of vorticity due to the roller as the fundamental ingredient for a physical description of the energy dissipation will lead to a weakly nonlinear Bousinesq-type model. As such, the breaking terms are derived directly through the decomposition of the velocity into a potential and a rotational part (Briganti et al., 2004).

To simplify the complex turbulence dynamics, this study revisited a data set derived from a relevant experiment by Liiv (2007). It was found by Oldekop et al. (2019) that the eddy viscosity determined experimentally is of high complexity under a breaking wave on the sloping bottom. In addition, the theoretically determined eddy viscosity values are in the same order of magnitude as the empirical and numerical predictions and follow reasonably well the production of turbulence during wave breaking.

This paper presents the results obtained by using the methodology proposed in the study of Oldekop et al. (2019) and considers the streamline curvature changed strain rates suggested by Luracelli et. al. (2018). In the present study, the orthogonal curvilinear coordinate system that follows the velocity field is used. The proposed novel solutions show the eddy viscosity variation both during the wave period and over the water depth. However, a qualitative improvement of the eddy viscosity was achieved by the water depth dependent functions which modify the mean velocity gradient components in the cross-coordinate system.

2 Methodology

2.1 Eddy viscosity

Reynolds stresses can be used to determine the eddy viscosity at any point of the turbulent flow field. At each

point and time, the Reynolds stress anisotropy $a_{ij} \equiv \langle u_i u_j \rangle - \frac{2}{3} \left(k_T + \nu_T \frac{\partial \langle u_k \rangle}{\partial x_k} \right) \delta_{ij}$, which corresponds to

turbulent shear stresses, is determined by the mean velocity gradient $\overline{\nabla\langle U \rangle}$ components and eddy viscosity ν_T .

According to the Boussinesq eddy viscosity assumption, the corresponding Reynolds stresses are

$$\begin{aligned} -\langle u_i u_j \rangle &= -\frac{2}{3} k_T \delta_{ij} + \nu_T \left(\frac{\partial \langle U_i \rangle}{\partial x_j} + \frac{\partial \langle U_j \rangle}{\partial x_i} - \frac{2}{3} \frac{\partial \langle U_k \rangle}{\partial x_k} \delta_{ij} \right) = \\ &= -\frac{2}{3} \left(k_T + \nu_T \frac{\partial \langle U_k \rangle}{\partial x_k} \right) \delta_{ij} + \nu_T \left(\frac{\partial \langle U_i \rangle}{\partial x_j} + \frac{\partial \langle U_j \rangle}{\partial x_i} \right). \end{aligned} \quad (1)$$

Reynolds stress is proportional to the mean rate of the compression and shear strain, where the eddy viscosity ν_T represents the positive scalar coefficient. However, only the anisotropic component a_{ij} is effective in transporting the momentum, while the isotropic component $\frac{2}{3} \left(k_T + \nu_T \frac{\partial \langle U_k \rangle}{\partial x_k} \right)$ can be absorbed in a modified mean pressure.

Reynolds stress anisotropy, Eq. (1), can be applied to derive a formula for the eddy viscosity coefficient that results from the Reynolds stress tensor non-diagonal elements:

$$\nu_T = \frac{-\langle u_1 u_2 \rangle}{\frac{\partial \langle U_1 \rangle}{\partial x_2} + \frac{\partial \langle U_2 \rangle}{\partial x_1}} \quad (2)$$

where the equation represents shear deformation and can be used in the case of a compressible as well as an incompressible fluid.

At the same time, when deriving from the Reynolds stress tensor, the first and the second diagonal elements result:

$$\nu_T = \frac{\frac{2}{3} k_T - \langle u_i u_i \rangle}{\frac{2}{3} \frac{\partial \langle U_i \rangle}{\partial x_i} - \frac{2}{3} \left(\frac{\partial \langle U_1 \rangle}{\partial x_1} + \frac{\partial \langle U_2 \rangle}{\partial x_2} \right)}, \quad (3)$$

where the equation that represents extension and bulk compression deformation can be used only in the case of a compressible fluid, or in the case of an incompressible fluid if the bulk compression rate is zero, i.e. $\nabla \cdot \langle \vec{U} \rangle = 0$.

2.2 Rotational velocity

In the Boussinesq-type models for surface waves, the flow is represented through the decomposition of the velocity into a potential and a rotational part. The velocity corresponding to a rotational part can be obtained by subtracting the velocity just outside the bottom boundary layer from the local velocity, and the mean velocity gradient components are modified by functions $A(x_2)$, $B(x_2)$, $C(x_2)$, $D(x_2)$, which depend on the distance from the bottom. The latter indicates that the specific correction functions correspond to the irrotational flow of

the velocity field. In other words, according to the approach by Briganti et al. (2004), the rotational velocity can be expressed in this case as

$$\overline{\langle U \rangle}_p = \overline{\langle U \rangle}_b + a x_2 \hat{a} + b x_2^2 \hat{b}, \quad (4)$$

where coefficients $a = f_a(A, B, C, D)$ and $b = f_b(A, B, C, D)$, x_2 vertical coordinate and unit vectors are \hat{a} and \hat{b} . In the cross-coordinate system, x_1 is along the channel horizontal coordinate. It should be mentioned here that in the present model rather high order velocity profiles are considered, i.e. $\sum_{i=0}^n a_i x_2^i \hat{a}_i$, where $n > 2$.

The approach by Briganti et al. (2004) is based on the Boussinesq assumptions of weakly non-linear long waves, and it indicates that the notion is less accurate as the waves approach breaking. However, comparisons with measured data by Veeramony & Svendsen (2000) show that the results agree well with the experimental data and can be applied to an outer region of surf zone.

3 Results

3.1 Physical model

Our experimental study of breaking waves with the propagation of regular waves over a uniformly sloping bottom was carried out in the wave flume with a bottom slope of a constant 1 to 17 positioned at the one end and a flap-type wave generator situated at the other end. Wave flume itself was 0.6 m in width, 0.6 m in depth and 22 m in length, with the origin of the coordinate system taken at the still water height 0.3 m, where the inclined bottom of the flume begins.

Velocity profiles were measured with a two component Argon-ion Laser Doppler Anemometer (LDA) with an output power of 1.3 W. During experimental runs, horizontal and vertical components, the corresponding signal drop-outs, water level variation and the signal from the synchronizing mechanism were stored. To determine an ensemble averaged unsteady mean velocity and velocity fluctuation, data was collected from 151 waves. The main characteristics of the regular wave in the experimental runs were for deep water: wave height 0.072 m, wave length 6.0 m, wave celerity 1.72 m s⁻² and wave period 2.03 s. Breaking waves were plunging type. As the LDA system allows measurements at one point, the measurements were repeated over 29 profiles along the slope, where profiles 1 to 19 were inside of the outer area of surf zone. The parameters observed in the experimental runs that were used for calculations in the present case are presented in Table 1.

Table 1. Location of measuring points and corresponding wave parameters

Profile No.	Distance from the reference point (m)	Still water depth d (m)	Water depth with wave set-up h (m)	Wave celerity C (m s ⁻²)
16	2.80	0.118	0.116	1.069
17	2.81	0.118	0.115	1.064
18	2.82	0.117	0.114	1.059

The physical model of the wave flume and preliminary data processing of the experimental tests of breaking waves on the sloping bottom developed at Tallinn University of Technology are described in detail by Liiv (2007).

3.2 Treatment of experimental results

Solutions for the direct ensemble averaged measured velocity confirm that eddy viscosity formulae result in peaks and negative values (see Oldekop et al., 2015). This is apparently due to the velocity corresponding to a potential part where its gradient components do not represent the shear straining and compression. Thus, an irrotational flow may be removed from the measured velocity by a specific treatment of the mean velocity and its derivatives. The velocity corresponding to a rotational part may be gained by subtracting the velocity just outside the bottom boundary layer from the local velocity: $\overline{\langle U \rangle}_t = \overline{\langle U \rangle} - \overline{\langle U \rangle}_b$. Furthermore, the mean velocity gradient components should be modified by the functions that depend on the distance above the bottom: $\left(\frac{\partial \langle U_1 \rangle}{\partial x_1}\right)_t = \frac{\partial \langle U_1 \rangle}{\partial x_1} - A(x_2)$, $\left(\frac{\partial \langle U_2 \rangle}{\partial x_2}\right)_t = \frac{\partial \langle U_2 \rangle}{\partial x_2} - B(x_2)$, $\left(\frac{\partial \langle U_1 \rangle}{\partial x_2}\right)_t = \frac{\partial \langle U_1 \rangle}{\partial x_2} - C(x_2)$, $\left(\frac{\partial \langle U_2 \rangle}{\partial x_1}\right)_t = \frac{\partial \langle U_2 \rangle}{\partial x_1} - D(x_2)$. In our approach, the used functions follow some conditions (see Table 2), i.e., $A(x_2) \ll B(x_2)$ and $C(x_2) = D(x_2)$.

Table 2. Change of functions $A(x_2)$, $B(x_2)$, $C(x_2)$, $D(x_2)$ over depth

Function (s ⁻¹)	Height above sloping bottom (m)				
	0.067	0.052	0.040	0.028	0.006
$A(x_2)$	0	1	1	4	4
$B(x_2)$	13	14	15	15	33
$C(x_2) = D(x_2)$	-45	-45	-44	-45	-135

3.3 Experimental findings

The turbulent kinetic energy and eddy viscosity were calculated at five heights of the same profile: a) 0.067 m; b) 0.052 m; c) 0.040 m; d) 0.028 m, and e) 0.006 m on the sloping bottom. Turbulent kinetic energy (see Fig. 1) demonstrates two maximums: at instants when the surface roller is passing the measuring point, i.e., dimensionless wave period interval 0.65 – 0.75, and after the wave crest is passing the measuring point, i.e., dimensionless wave period interval 0.80 – 0.85. After breaking of a wave, there is a minimum in the turbulent kinetic energy value occurring during a dimensionless wave period interval 0.00 – 0.10, which then converges to more or less constant value during a dimensionless wave period interval 0.10 – 0.60. It can be seen that the turbulent kinetic energy varies almost linearly with the increasing height from the bed (also seen in Fig. 3).

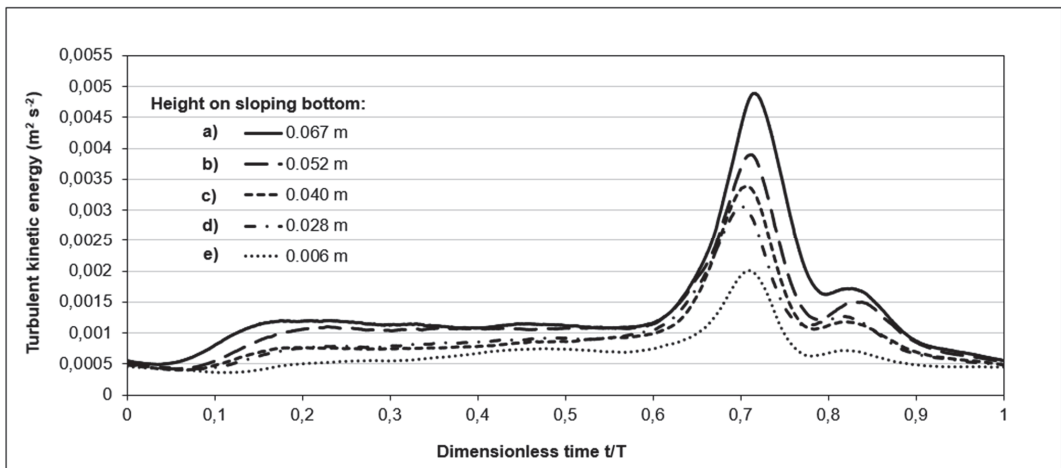


Fig. 1. Determined turbulent kinetic energy at five heights of the same profile, above sloping bottom: a) 0.067 m; b) 0.052 m; c) 0.040 m; d) 0.028 m and e) 0.006 m.

The eddy viscosity (see Fig. 2) demonstrates three maximums on three higher measurement points, i.e., 0.040 m, 0.052 m and 0.067 m: at instants when the surface roller hits the water surface, i.e., dimensionless wave period interval 0.50 – 0.60, when the surface roller is passing the measuring point, i.e., dimensionless wave period interval 0.65 – 0.75, and after the wave crest is passing the measuring point, i.e., dimensionless wave period interval 0.80 – 0.85. Two later eddy-viscosity maximums correspond in time with the turbulent kinetic energy maximums.

After breaking of a wave, the eddy viscosity value is more or less constant during a dimensionless wave period interval 0.90 – 0.50. However, on the second lowest measurement point, i.e., 0.028 m, there are only two

last maximums compared to previous higher measurement heights, and for the lowest measurement point, i.e., 0.006 m, it is close to one maximum at the instants of the wave crest, i.e., dimensionless wave period instant 0.75. In other words, the turbulence develops in the layers close to the bottom when the roller generated turbulence develops downwards and the eddy viscosity maximum appears when the surface roller has passed and then disappears in the layer closest to the bottom, i.e., at height 0.006 m.

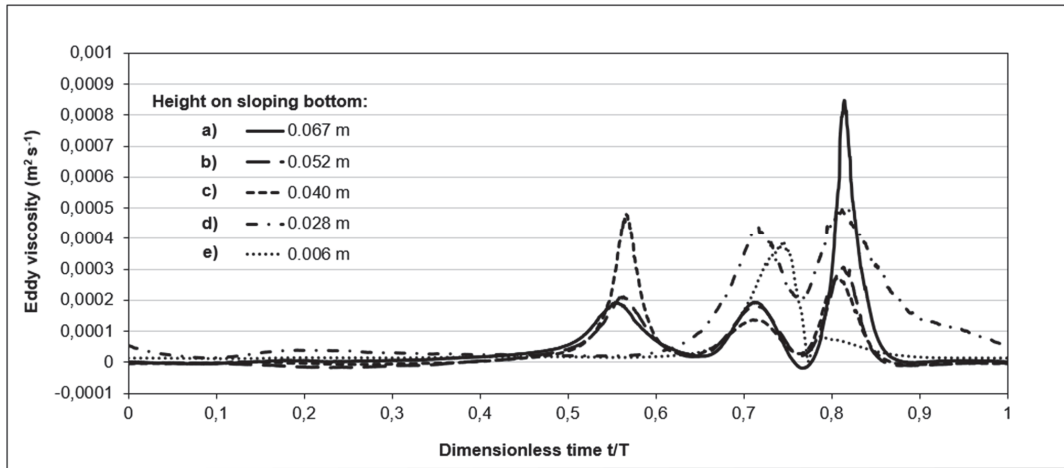


Fig. 2. Averaged eddy viscosity values based on theoretical equations with the surface direction index i and the flow direction index j at different heights above sloping bottom: a) 0.067 m; b) 0.052 m; c) 0.040 m; d) 0.028 m and e) 0.006 m.

Furthermore, the eddy viscosity based on the non-diagonal elements from the Reynolds stress tensor with shear deformation is responsive of the first maximum, from Eq. (2), while eddy viscosity based on the first and second diagonal elements from the Reynolds stress tensor with extension and bulk compression rates is responsive of the last two maximums, from Eq. (3).

Additionally, eddy viscosity values demonstrate obvious maximums in Fig. 2, i.e., the highest values at wave period dimensionless instants 0.556432, 0.711681 and 0.814687, the corresponding eddy viscosity profiles of which are shown in Fig. 3. The eddy viscosity value maximum, i.e., $\sim 0.00085 \text{ m}^2 \text{ s}^{-1}$, occurs on the highest measurement point, i.e., at height 0.067 m, appearing directly after the wave crest passing the measuring point (shown by continuous curve on Fig. 3). Second and third peak-magnitudes of the eddy viscosity, i.e., $\sim 0.00048 \text{ m}^2 \text{ s}^{-1}$ and $\sim 0.00042 \text{ m}^2 \text{ s}^{-1}$ respectively, are both on the second lowest measurement point, i.e., 0.028 m, when the wave crest is passing the measuring point (shown by continuous curve on Fig. 3) and when the

surface roller is passing (shown by longer dashed curve on Fig. 3). Fourth peak-magnitude of the eddy viscosity, i.e., $\sim 0.00035 \text{ m}^2 \text{ s}^{-1}$, is on the middle measurement point, i.e., 0.040 m, at the instants when the surface roller hits the water surface (shown by shorter dashed curve on Fig. 3). In the other words, the eddy viscosity generated in the surface roller hitting the surface affects mostly middle depths, while surface roller passing affects mostly the bottom region and wave crest passing affects both the surface and the bottom region. For comparison, Fig. 3 shows a selected dimensionless wave period instant 0.245441 to demonstrate eddy viscosity values outside of the maximum values, where the eddy viscosity values are more or less constant over the water depth.

Also, Fig. 3 shows the turbulent kinetic energy on the same time instances. It was found that the largest maximum of eddy viscosity does not appear in compliance with the largest maximum of turbulent kinetic energy, and vice versa. Furthermore, the monotonically decreasing characteristic of turbulent kinetic energy over the water depth does not relate to the varying nature of eddy viscosity.

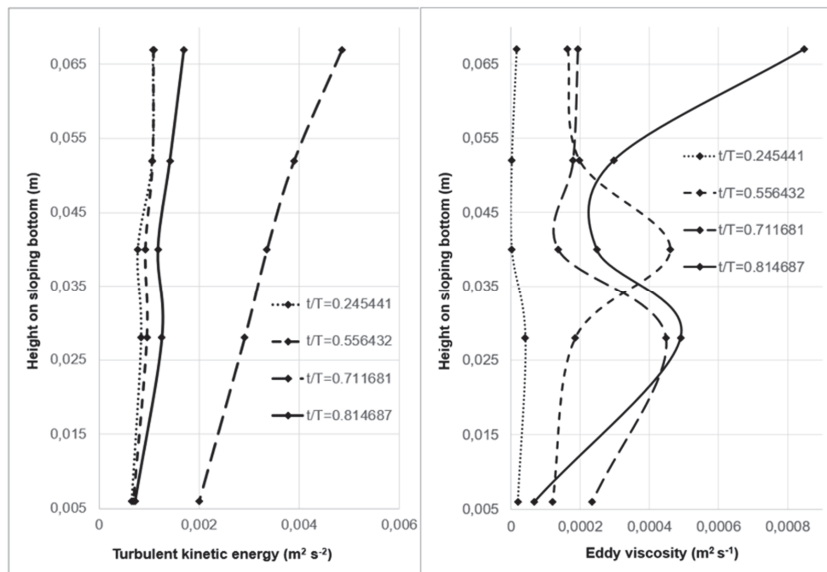


Fig. 3. Turbulent kinetic energy and averaged eddy viscosity values over the water depth at the maximums shown in Figs. 1-2 in the dimensionless wave period: a) 0.245441; b) 0.556432; c) 0.711681 and d) 0.814687.

3.4 Extra strain rates

According to Lucarelli et al. (2018), the extra strain rates that characterize a curved flow are needed to consider the mixing layer in the breaking wave. For this purpose, the orthogonal curvilinear coordinates are used to determine the bulk compression and extension rates induced by the streamline curvature. The resulting eddy

viscosity, based on the first diagonal elements from the Reynolds stress tensor with extension and bulk compression rates, has peaks in it. The same peaks were present in Lucarelli et al. (2018) as well. However, the second diagonal elements from the Reynolds stress tensor give positively valued eddy viscosity. Furthermore, there is only one maximum at instants when the surface roller hits the water surface, i.e., dimensionless wave period interval 0.50 – 0.60. This maximum aligns well with the first maximum of the eddy viscosity from the cross-coordinate system (see Fig. 2) based on the non-diagonal elements from the Reynolds stress tensor with shear deformation, from Eq. (2).

4 Conclusions and discussion

In the present study, the eddy viscosity was derived from the combined functions (see Eqs. 2-3) of Reynolds stresses, modified mean velocity, its gradient components and from turbulent kinetic energy for a weakly compressible fluid. The proposed analysis showed that the irrotational flow that masked the turbulence velocity field under a breaking wave can be removed by means of the oscillating velocity at the bottom proposed by Briganti et al. (2004). Four coefficients were used to modify the gradient components of the particular mean velocity. The deformation of the fluid element was strongly related to the pressure and viscous-stress work in the surface and bottom boundary layers, which merged in the surf zone. The modified velocity field ensured that the turbulence production was positive throughout the wave period.

Considering variations in the turbulent kinetic energy values with two maximums during the wave period and almost linear variation over the water depth, it was apparent that the eddy viscosity values are also changing during the wave period and over the water depth. It should be noted that the eddy viscosity does not decay monotonically from the surface to the bed like turbulent kinetic energy; and the largest maximum of eddy viscosity does not appear in compliance with the largest maximum of turbulent kinetic energy. It was demonstrated that taking use of the velocity measurements, the Boussinesq eddy viscosity assumption can be presented with the eddy viscosity, being the positive scalar coefficient.

Considering the orthogonal curvilinear coordinate system suggested by Luracelli (2018) instead of the cross-coordinate system leads to the eddy viscosity with an n-number of peaks from the first diagonal elements from the Reynolds stress tensor. However, the second diagonal elements give positively valued eddy viscosity that aligns to the eddy viscosity from the non-diagonal elements of the cross-coordinate system from the

Reynolds stress tensor. Turbulent kinetic energy values remain unchanged due to the change in the coordinate system.

Acknowledgements

This work was partly supported by the Estonian Ministry of Education and Research [grant IUT 19-17].

Notation

\hat{a}, \hat{b} = unit vectors (-)

a_{ij} = anisotropic component ($\text{m}^2 \text{s}^{-2}$)

C_0 = deep water wave celerity (m s^{-2})

$\frac{\partial \langle U \rangle}{\partial x}$ = velocity gradient (s^{-1})

$\left(\frac{\partial \langle U \rangle}{\partial x}\right)_t$ = modified velocity gradient (s^{-1})

H_0 = deep water wave height (m)

$i, j = 1, 2$ denote x_1, x_2 directions respectively

k_T = turbulent kinetic energy ($\text{m}^2 \text{s}^{-2}$)

L_o = deep water wave length (m)

T = wave period (s)

U = instantaneous local velocity (m s^{-1})

$\langle U \rangle$ = ensemble-averaged velocity (m s^{-1})

$\langle U \rangle_b$ = ensemble-averaged velocity on bottom boundary (m s^{-1})

$\langle U \rangle_p$ = ensemble-averaged potential velocity (m s^{-1})

$\langle U \rangle_t$ = modified ensemble-averaged velocity (m s^{-1})

u = velocity fluctuation (m s^{-1})

x_1 = along the flow horizontal coordinate (-)

x_2 = vertical coordinate (-)

δ_{ij} = Kronecker delta (-)

ν_T = eddy viscosity ($\text{m}^2 \text{s}^{-1}$)

References

- Briganti, R., Musumeci, R.E., Bellotti, G., Brocchini, M. & Foti, E. (2004). Boussinesq modeling of breaking waves: Description of turbulence. *J. Geophys. Res.*, 109(C0701). doi:10.1029/2003JC002065
- Liiv, T. (2007). An experimental investigation of the oscillatory boundary layer around the breaking point. *Proceedings of the Estonian Academy of Sciences*, 13(3), 215-233.
- Luracelli, A., Lugni, C., Falchi, M., Felli, M., & Brocchini, M. (2018). Extra Strain Rates in an unsteady spilling breaking wave. *Scientific Reports*, 8(13926), 1-8. doi:10.1038/s41598-018-32307-3
- Oldekop, N., Liiv, T. & Laanearu, J. (2019). Experimental study of eddy viscosity for breaking waves on sloping bottom and comparisons with empirical and numerical predictions. *Journal of Earth Science and Engineering*, 68(3), 299-312. doi:10.3176/proc.2019.3.07
- Oldekop, N. & Liiv, T. (2015). The variation of turbulent eddy viscosity during a wave cycle. E-Proceedings of the 36th IAHR World Congress, The Hague, Netherlands, 28 June – 3 July 2015, 1–5.
- Veeramony, J. & Svendsen, I.A. (2000). The flow in surf-zone waves. *Coastal Engineering*, 39, 93-122. doi: 10.1016/S0378-3839(99)00058-7

Curriculum vitae

Personal data

Name: Nelly Oldekop
Date of birth: 30.07.1984
Place of birth: Estonia
Citizenship: Estonian

Contact data

E-mail: nelly.oldekop@taltech.ee

Education

2011–2019 Tallinn University of Technology, Doctoral study, Civil and Environmental Engineering – PhD
2003–2008 Tallinn University of Technology, Engineering study, Civil and Building Engineering – MSC
1991–2003 Märjamaa Gymnasium, High school

Language competence

Estonian Native language
English Fluent
Russian Beginner

Professional employment

2007– ... Corson LLC, Civil engineer
2006–2007 ETP Grupp AS, Senior Designer
2006–2007 Tallinn University of Technology, Applicant

Certifications

2019–2026 Chartered Civil Engineer in Buildings and Structures, EstQF level 8. Competences: Design and construction of waterfront structures
2018–2023 Diploma Civil Engineer in Buildings and Structures, EstQF level 7. Competences: Building design and construction
2014–2019 Diploma Civil Engineer in Buildings and Structures, EstQF level 7. Competences: Design and construction of waterfront structures
2016– ... Member of International Association for Hydro-Environment Engineering and Research (IAHR)
2014– ... Certified International Engineering Educator by International Society for Engineering Pedagogy

Field of research

4. Natural Sciences and Engineering; 4.15. Construction and Municipal Engineering; CERCS SPECIALITY: T220 Civil engineering, hydraulic engineering, offshore technology, soil mechanics

Supervised dissertations

Kaur Tull, Master's Degree, 2015, (sup) Nelly Oldekop, Analytical calculations for increasing the bearing capacity of the reinforced concrete ribbed slabs of berth no. 11 in the port of Muuga, Tallinn University of Technology Faculty of Civil Engineering, Department of Mechanics

Publications

- Oldekop, N.;** Liiv, T.; Laanearu, J. (2019). Experimental study of eddy viscosity for breaking waves on sloping bottom and comparisons with empirical and numerical predictions. Proceedings of the Estonian Academy of Sciences, 68 (3), 299–312.10.3176/proc.2019.3.07.
- Oldekop, N.;** Liiv, T. (2015). The variation of turbulent eddy viscosity during a wave cycle. Proceedings of the 36TH IAHR world congress: deltas of the future and what happens upstream: 36th IAHR World Congress, The Hague, Netherlands, 28 June – 3 July, 2015. International Association for Hydro-Environment Engineering and Research - IAHR, 1–5.
- Oldekop, N.;** Liiv, T. (2013). Measurement of the Variation of Shear Velocity on Bed during a Wave Cycle. Journal of Earth Science and Engineering, 3, 322–330.
- Oldekop, N.;** Liiv, T. (2012). Measurement of the Variation Bed Shear Stress during a Wave Cycle. ICSE-6: Paris, August 27–31, 2012: 6th International Conference on Scour and Erosion: Proceedings: 6th International Conference on Scour and Erosion, Paris, August 27–31, 2012. Societe Hydrotechnique de France, 152–157.

Elulookirjeldus

Isikuandmed

Nimi: Nelly Oldekop
Sünniaeg: 30.07.1984
Sünnikoht: Eesti
Kodakondsus: eestlane

Kontaktandmed

E-post: nelly.oldekop@taltech.ee

Hariduskäik

2011–2019 Tallinna Tehnikaülikool, Doktoriõpe, Ehitus- ja keskkonnatehnika – PhD
2003–2008 Tallinna Tehnikaülikool, Integreeritud õpe, Tööstus- ja tsiviilehitus – MSC
1991–2003 Märjamaa Gümnaasium, Keskkharidus

Keelteoskus

Eesti keel Emakeel
Inglise keel Kõrgtase
Vene keel Algtase

Teenistuskäik

2007– ... Corson OÜ, Projekteerija-konstruktor
2006–2007 ETP Grupp AS, Vanemtehnik
2006–2007 Tallinna Tehnikaülikool, Asjaajaja

Tunnustused

2019–2026 Volitatud ehitusinsener, EKR tase 8. Spetsialiseerumine: Sadamaehitus. Kompetents: Sadamarajatiste projekteerimine
2018–2023 Diplomeeritud ehitusinsener, EKR tase 7. Spetsialiseerumine: Hoonete ehitus. Kompetents: Projekteerimine
2014–2019 Diplomeeritud ehitusinsener, EKR tase 7. Spetsialiseerumine: Sadamaehitus. Kompetents: Projekteerimine
2016– ... Rahvusvaheline Hüdraulika Inseneriteaduste ja Uuringute Assotsiatsiooni liige (IAHR)
2014– ... Sertifitseeritud Rahvusvaheline insenerpedagoog

Teadustöö põhisuund

4. Loodusteadused ja tehnika; 4.15. Ehitus- ja kommunaaltehnika; CERCS ERIALA: T220 Tsiiviilehitus, Hüdrotehnoloogia, avameretehnoloogia, pinnasemehhaanika

Juhendatud väitekirjad

Kaur Tull, magistrakraad, 2015, (juh) Nelly Oldekop, Muuga sadama kai nr. 11 analüütilised arvutused raudbetoonribipaneelide kandevõime suurendamiseks, Tallinna Tehnikaülikool, Ehitusteaduskond, Mehaanikainstituut.

Publikatsioonid

Oldekop, N.; Liiv, T.; Laanearu, J. (2019). Experimental study of eddy viscosity for breaking waves on sloping bottom and comparisons with empirical and numerical predictions. Proceedings of the Estonian Academy of Sciences, 68 (3), 299–312.10.3176/proc.2019.3.07.

- Oldekop, N.;** Liiv, T. (2015). The variation of turbulent eddy viscosity during a wave cycle. Proceedings of the 36TH IAHR world congress: deltas of the future and what happens upstream: 36th IAHR World Congress, The Hague, Netherlands, 28 June – 3 July, 2015. International Association for Hydro-Environment Engineering and Research - IAHR, 1–5.
- Oldekop, N.;** Liiv, T. (2013). Measurement of the Variation of Shear Velocity on Bed during a Wave Cycle. *Journal of Earth Science and Engineering*, 3, 322–330.
- Oldekop, N.;** Liiv, T. (2012). Measurement of the Variation Bed Shear Stress during a Wave Cycle. ICSE-6: Paris, August 27–31, 2012: 6th International Conference on Scour and Erosion: Proceedings: 6th International Conference on Scour and Erosion, Paris, August 27–31, 2012. Societe Hydrotechnique de France, 152–157.